Swept Source Optical Coherence Microscopy for Pathological Assessment of Cancerous Tissues

by

Osman Oguz Ahsen

B.S., Electrical and Electronics Engineering
Bilkent University, 2010

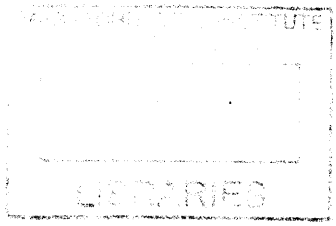

Submitted to the

DEPARTMENT OF ELECTRICAL ENGINEERING AND COMPUTER SCIENCE

in partial fulfillment of the requirements for the degree of

MASTER OF SCIENCE

at the

MASSACHUSETTS INSTITUTE OF TECHNOLOGY

February 2013

Signature of Author _____
Department of Electrical Engineering and Computer Science
December 28, 2012

Certified by _____
James G. Fujimoto
Elihu Thomson Professor of Electrical Engineering
Thesis Supervisor

Accepted by _____
Leslie A. Kolodziejski
Professor of Electrical Engineering
Chair, Department Committee on Graduate Students

Swept Source Optical Coherence Microscopy for Pathological Assessment of Cancerous Tissues

by

Osman Oguz Ahsen

Submitted to the Department of Electrical Engineering and Computer Science
on December 28, 2012 in Partial Fulfillment of the
Requirements for the Degree of Master of Science in
Electrical Engineering and Computer Science

Abstract

Optical coherence microscopy (OCM) combines optical coherence tomography (OCT) with confocal microscopy and enables depth resolved visualization of biological specimens with cellular resolution. OCM offers a suitable alternative to confocal imaging by providing enhanced contrast due to the additional coherence gate to the inherent confocal gate, increasing the field of view and imaging depth, and eliminating the need of external contrast agents. In the past, development of OCT systems have been focused on time domain and spectral/Fourier domain methods which offer high axial resolution and imaging speeds. However, recent advances in the OCT technology have pushed the development into the direction of swept source OCT technologies, and development of the OCM technology is likely to follow this path.

This thesis describes construction, characterization and preliminary imaging results of a swept source OCM (SS-OCM) system utilizing a novel light source, Vertical Cavity Surface-Emission Laser (VCSEL). This swept source laser can reach sweep rates exceeding 1 MHz and provide wide tuning ranges, which will enable both imaging speeds approaching to time domain OCM (TD-OCM) systems, and axial resolution approaching to spectral/Fourier domain OCM (SD-OCM) systems. Several other advantages of SS-OCM compared to TD-OCM and SD-OCM that make this technology a promising alternative to the latter imaging methods are presented. Furthermore, practical concepts in the system development and signal processing, such as compensation for the scan curvatures, methods for calibration of the spectrums, selection of suitable color maps for display, and other related topics are also discussed in the text.

In addition to technical description of the OCM system development, an in depth analysis of several clinical applications that will be likely to benefit from this imaging modality is also presented. Real time intraoperative feedback is required in order to reduce the morbidity and the rate of additional operations for the surgical management of several forms of cancer, where

a benchtop OCM system residing in the pathology laboratory can be immensely beneficial. Furthermore, with the novel scanning mechanisms that have been developed in the recent years it is possible to translate this imaging modality to an *in vivo* setting where an OCM probe can be inserted through the working channel of an endoscope and generate cellular resolution images in real time without the need of external contrast agents. Endoscopic management and clinical challenges for a spectrum of lower gastrointestinal (GI) diseases is discussed where an *in vivo* OCM imaging probe can play an important role in the diagnosis and evaluation of the extend of the particular disease. A review of alternative imaging modalities, such as chromoendoscopy, narrow band imaging (NBI) and confocal laser endomicroscopy (CLE) is also included which outlines the relative strengths and limitations of these imaging modalities for the clinical management of lower GI diseases.

Thesis Supervisor: James G. Fujimoto
Title: Elihu Thomson Professor of Electrical Engineering

Acknowledgements

I am grateful to my thesis advisor Prof. Fujimoto for giving me the opportunity to work in this highly esteemed research group and providing the facilities and guidance that enabled me to complete this thesis. Not only his remarkable scientific and administrative oversight, also his genuine sense of responsibility and commitment to generate the technology to offset the investment of society into scientific research is truly noteworthy and deserves a great deal of appreciation.

I would like to thank many of the graduate students and postdoctoral associates that were immensely helpful to me in the transition to graduate studies. To name just a few, Kenny Tao was instrumental in teaching me the fundamental concepts of optics and share his vast scientific knowledge. Similarly, Chao Zhou, Ireneusz Grulkowski and Jonathan Liu were always reachable and did not hesitate to share their experiences and wisdom. I am very glad to be working closely with the cancer research team in our group including Tsung-Han Tsai, Hsiang-Chieh Lee and Kaicheng Liang. Ben Potsaid was very helpful especially in setting up and operating the VCSEL sources, as well as bridging our collaboration with Thorlabs. I am very grateful to the comments and insights of Aaron Aguirre on this project, who despite having already graduated from our group continues to share is broad expertise on these topics.

Last but not least I would like to thank to my family and friends who keep supporting me morally and arrange the activities that provide me the necessary relaxation to maintain the intense level of academic studies.

Graduate life is certainly not easy and requires a certain amount of sacrifice; however, I believe that it is a very effective platform in pushing one's limits on scientific knowledge and enlightenment. Therefore, I am very happy to be a part of this journey and I am very excited for the upcoming years.

Table of Contents

1. Introduction and Scope of the Thesis

There are several cancer imaging applications that will benefit from an imaging modality that provides non-destructive evaluation of pathological state of the tissue in real time. The following discussion will provide insight on some of the pressing challenges for the management of breast, lung, head and neck, and thyroid cancers, where real time intraoperative feedback is required in order to reduce the morbidity and the rate additional operations for the surgical management of the particular disease.

For the clinical management of non-metastatic breast cancer, breast conserving therapy (BCT) is the standard of care for the surgical intervention due to its superiority over radical mastectomy in terms of providing acceptable cosmetic outcome, reduced morbidity associated with lymphedema, and improved quality of life after operation, as well as ensuring equivalence in the survival and low rate of local recurrence [1-4]. Although in order to provide best cosmetic outcome it is important to resect only the tissue involved in the cancer, this approach often leads to residual tumor tissue at the boundaries of the excised specimen or the lumpectomy cavity, especially for the case of clinically occult (nonpalpable) lesions [5, 6]. Consequently, up to 40% of all patients undergoing BCT require repeat surgical resection as a result of positive or close margins [7-11]. Alternative real time imaging strategies such as frozen section analysis (FSA) suffers from sampling errors, low sensitivity (~70%) and increased procedure time (>15 minutes), and are often destructive for small specimens [12-15].

For the surgical management of lung cancer, which accounts for 28% of all cancer related deaths, early detection of smaller sized tumors is increased over the past years owing to the advancements on radiological imaging techniques [16-18]. Although the safe way for the management of a confirmed lung malignancy is a pulmonary lobectomy, which involves the surgical removal of the lobe involved with the cancer, improvements in the detection of lower grade tumors has pushed the applications of lung sparing surgeries such as wedge resection and sleeve resection [19-21]. With the studies showing equivalence of survival rates to standard lobectomy, lung sparing procedures have the potential to provide the removal of the tumor without compromising the lung function [22]. For these surgeries it is important to ensure a tumor free margin in order to minimize recurrence. Although gross evaluation and image guidance is routinely being used for discriminating the overall boundaries of the tumor, studies have shown that about 31% of the central tumors and 19% of the peripheral tumors have a microscopic proximal extension, making it hard to detect with these methods [23, 24]. Consequently up to 17% of resection cases shows a positive bronchial margin at the resection boundary [25]. The application of FSA for intraoperative margin assessment during the lung

resection surgery suffers from low sensitivity as it is shown to have about 42% false negative rate in detecting the presence of tumor cells at the resection margin [26].

Another challenge for the management of lung cancer is to establish a correct diagnosis on suspicious lung nodules. As an example, studies have found a thoracic metastasis in up to 18% of breast cancer patients, hence for the patients with a history of breast cancer it is critical to distinguish between breast cancer metastasis and primary lung lesion, as the surgical management for these two scenarios are vastly different [27, 28]. Even with bronchoscopic guidance, transbronchial biopsy suffers from sampling problems and low yield [29, 30]. FSA has been used to provide an intraoperative diagnosis for the suspicious lung nodules, however, it has shown to have a 7.5% error rate for detecting malignancy [31]. Furthermore, another study showed deferral to permanent histology with a rate of 15.5% in making a differential diagnosis between primary lung lesion and metastatic breast carcinoma, showing the limitation of FSA in differentiating between primary lung lesion and metastatic breast cancer [32]. Moreover, the use of FSA is not recommended for the nodules smaller than 5 mm, as the FSA preparation renders it impossible to obtain a permanent histological diagnosis afterwards [33].

Head and neck cancers include the cancers of oral cavity, pharynx and larynx, and account for about 3.2% of all cancer incidences [34]. Especially for the early stage cancers it is critical to limit extend of the resection in order to provide the best quality of life after surgery. A repeat surgery is often not desired, especially in case of immediate reconstruction operations or due to anatomical limitations [35]. Consequently establishing a negative margin with the initial surgery becomes an important concern [36]. As an example, studies for oral cancers demonstrated reduced 5 year survival rates as low as 50% for a positive margin, whereas the survival can be as high as 91% for a negative margin and 85% for a close margin [37, 38]. Although FSA is shown to have high correlation with the permanent histology results of the same tissue (89% and 99% sensitivity and specificity, respectively), in the same study it failed to detect positive final margin in as high as 40% of patients [39]. In another large scale study on 4976 specimens, it is shown to have a 15% sampling error rate for head and neck tumor resections [40].

With a 56,460 estimated new cases in 2012, thyroid cancer accounts for 3.4% of all cancer incidences and is the most common malignancy of the endocrine system [34]. Although the incidence of this cancer is relatively low and the survival rates for the diagnosed patients are high (5 year survival rates >95%), the main challenge for the management of this disease is to differentiate malignant lesions from benign lesions, as ultrasonography detects thyroid nodules with a very high prevalence of up to 42% of the general population [41-43]. Fine needle aspiration (FNA) cytology is the standard method for pre-operative assessment of the malignancy of the thyroid nodules. Although the accuracy of this technique is close to 95%

when a diagnosis has been made, about 20% to 33% of the FNA results as indeterminate for the malignancy of the nodule [44-46]. Frozen section analysis (FSA) is proposed to be used to determine the malignancy of the nodules during the initial thyroidectomy procedure, however, it suffers from low sensitivity (~30%), hence has not gained clinical acceptance [47, 48]. Therefore, an accurate intraoperative assessment technique will be immensely useful in guiding the extent of the thyroidectomy and preventing unnecessary total thyroidectomy procedures.

Apart from the applications mentioned in the following paragraphs that will benefit from an imaging modality which provides real time intraoperative feedback, several other clinical scenarios require real time, *in situ* assessment of the tissues in order to guide targeted biopsies, to detect or diagnose malignant lesions, and to assess treatment response and efficacy. Especially for a range of diseases related to human gastrointestinal (GI) tract, current strategies for the detection and diagnosis of malignant lesions suffer from low yield, non specifity and prolonged procedure times. Chapter 2 presents an in depth discussion on some of the pressing challenges in the management of some of the highly prevalent GI diseases.

Optical coherence tomography (OCT) enables real-time, *in vivo,* micron-scale and three-dimensional (3D) imaging of biological tissues without the need to sacrifice and process specimens. OCT has been used for a wide range of clinical applications in human, including ophthalmology [49-52], endoscopy [53-59], and cardiovascular imaging [60-64]. Optical coherence microscopy (OCM) combines OCT with confocal microscopy and enables depth resolved visualization of biological specimens with cellular resolution [65, 66]. OCM offers a suitable alternative to confocal imaging by providing enhanced contrast due to the additional coherence gate to the inherent confocal gate, increasing the field of view and imaging depth, and eliminating the need of external contrast agents. Due to its unique advantages over alternative real-time imaging modalities, a benchtop OCM system residing in the pathology suite will be extremely beneficial for the clinical management of the cancer types described previously. Furthermore, with the novel scanning mechanisms that have been developed in the recent years it is possible to translate this imaging modality to an *in vivo* setting where a probe can be inserted through the working channel of an endoscope or bronchoscope, and generate cellular resolution images in real time without the need of external contrast agents.

This thesis describes the construction, characterization and preliminary imaging results of a swept source OCM (SS-OCM) system utilizing a novel light source, Vertical Cavity Surface-Emission Laser (VCSEL). This swept source laser can reach sweep rates exceeding 1 MHz and provide wide tuning range, which will enable both imaging speeds approaching to time domain OCM (TD-OCM) systems, and axial resolution approaching to spectral/Fourier domain OCM (SD-OCM) systems. Two prototype VCSEL light sources, operating at 1060 nm and 1310 nm, have been employed in this study that are developed with the collaboration of Thorlabs, Inc.

(Newton, NJ) and Pravium Research, Inc. (Santa Barbara, CA). The 1060 nm and 1310 nm VCSEL systems use the same sample arm optics whereas the fibers and couplers used in the interferometer setup are tailored for the respective wavelengths. 1060 nm VCSEL is a prototype turnkey operated light source which exploits optical clocking to acquire spectrums linear in wavenumber. For the 1310 nm VCSEL, acquisition is performed also with optical clocking, as well as by internally clocking the acquisition card and subsequent calibration of the spectrums using Mach Zehnder interferometer (MZI) traces.

This thesis is developed in the following order:

Chapter 2 starts by describing endoscopic management and clinical challenges for a spectrum of lower GI diseases where an *in vivo* OCM imaging probe can play a significant role in the diagnosis and evaluation of the extend of the particular disease. Then, a review of alternative imaging modalities, such as chromoendoscopy, narrow band imaging (NBI) and confocal laser endomicroscopy (CLE) is presented, which outlines the relative strengths and limitations of these imaging modalities in the context of management of lower GI diseases.

Chapter 3 gives an overview for the history of development of the OCM technology, with a particular emphasis on their clinical applications. Discussion and comparison about the TD-OCM, SD-OCM and SS-OCM imaging modalities is also included outlining the advantages and disadvantages of each imaging method.

Chapter 4 begins with schematics of the overall system design, and then describes the methods employed for the acquisition and calibration of the spectrums. In this context, a detailed discussion on how the spectrums are calibrated for the internally clocked system, as well as how optical clocking is achieved is also included. The discussion is followed by describing some practical concepts in the system development and signal processing, such as compensation for the scan curvatures, generating larger field of view mosaic images and selection of suitable color maps for display. Finally, the performance of the system is assessed by presenting measurements for the characterization of the imaging setup.

Chapter 5 presents example images obtained from *ex vivo* rabbit and human specimens, using the 1060 nm and 1310 nm OCM systems. Rabbit samples include colon and kidney, whereas samples from human include normal colon and invasive breast cancer specimens. Demonstration of large field of view mosaic images is also included.

Chapter 6 summarizes the concepts and discussion presented throughout the thesis and gives directions for the future development of the system.

References

[1] B. Fisher, C. Redmond, R. Poisson, R. Margolese, N. Wolmark, L. Wickerham, E. Fisher, M. Deutsch, R. Caplan, Y. Pilch, and et al., "Eight-year results of a randomized clinical trial comparing total mastectomy and lumpectomy with or without irradiation in the treatment of breast cancer," *N Engl J Med,* vol. 320, pp. 822-8, Mar 30 1989.

[2] R. Arriagada, M. G. Le, F. Rochard, and G. Contesso, "Conservative treatment versus mastectomy in early breast cancer: patterns of failure with 15 years of follow-up data. Institut Gustave-Roussy Breast Cancer Group," *J Clin Oncol,* vol. 14, pp. 1558-64, May 1996.

[3] J. A. van Dongen, A. C. Voogd, I. S. Fentiman, C. Legrand, R. J. Sylvester, D. Tong, E. van der Schueren, P. A. Helle, K. van Zijl, and H. Bartelink, "Long-term results of a randomized trial comparing breast-conserving therapy with mastectomy: European Organization for Research and Treatment of Cancer 10801 trial," *J Natl Cancer Inst,* vol. 92, pp. 1143-50, Jul 19 2000.

[4] B. Fisher, S. Anderson, J. Bryant, R. G. Margolese, M. Deutsch, E. R. Fisher, J. H. Jeong, and N. Wolmark, "Twenty-year follow-up of a randomized trial comparing total mastectomy, lumpectomy, and lumpectomy plus irradiation for the treatment of invasive breast cancer," *N Engl J Med,* vol. 347, pp. 1233-41, Oct 17 2002.

[5] B. Cleffken, J. Postelmans, S. Olde Damink, M. Nap, I. Schreutelkamp, and H. van der Bijl, "Breast-conserving therapy for palpable and nonpalpable breast cancer: can surgical residents do the job irrespective of experience?," *World Journal of Surgery,* vol. 31, pp. 1731-6, Sep 2007.

[6] K. Moorthy, V. Asopa, E. Wiggins, and M. Callam, "Is the reexcision rate higher if breast conservation surgery is performed by surgical trainees?," *American Journal of Surgery,* vol. 188, pp. 45-8, Jul 2004.

[7] F. J. Fleming, A. D. Hill, E. W. Mc Dermott, A. O'Doherty, N. J. O'Higgins, and C. M. Quinn, "Intraoperative margin assessment and re-excision rate in breast conserving surgery," *Eur J Surg Oncol,* vol. 30, pp. 233-7, Apr 2004.

[8] G. P. Swanson, K. Rynearson, and R. Symmonds, "Significance of margins of excision on breast cancer recurrence," *Am J Clin Oncol,* vol. 25, pp. 438-41, Oct 2002.

[9] E. L. Wiley, L. K. Diaz, S. Badve, and M. Morrow, "Effect of time interval on residual disease in breast cancer," *Am J Surg Pathol,* vol. 27, pp. 194-8, Feb 2003.

[10] M. S. Sabel, K. Rogers, K. Griffith, R. Jagsi, C. G. Kleer, K. A. Diehl, T. M. Breslin, V. M. Cimmino, A. E. Chang, and L. A. Newman, "Residual disease after re-excision lumpectomy for close margins," *Journal of Surgical Oncology,* vol. 99, pp. 99-103, Feb 1 2009.

[11] A. Kobbermann, A. Unzeitig, X. J. Xie, J. Yan, D. Euhus, Y. Peng, V. Sarode, A. Moldrem, A. Marilyn Leitch, V. Andrews, C. Stallings, and R. Rao, "Impact of routine cavity shave margins on breast cancer re-excision rates," *Annals of Surgical Oncology,* vol. 18, pp. 1349-55, May 2011.

[12] M. R. Weiser, L. L. Montgomery, B. Susnik, L. K. Tan, P. I. Borgen, and H. S. Cody, "Is routine intraoperative frozen-section examination of sentinel lymph nodes in breast cancer worthwhile?," *Ann Surg Oncol,* vol. 7, pp. 651-655, Oct 2000.

[13] J. Cendan, D. Coco, and E. Copelandiii, "Accuracy of Intraoperative Frozen-Section Analysis of Breast Cancer Lumpectomy-Bed Margins," *Journal of the American College of Surgeons,* vol. 201, pp. 194-198, 2005.

[14] S. L. Blair, K. Thompson, J. Rococco, V. Malcarne, P. D. Beitsch, and D. W. Ollila, "Attaining Negative Margins in Breast-Conservation Operations: Is There a Consensus among Breast Surgeons?," *Journal of the American College of Surgeons,* vol. 209, pp. 608-613, Nov 2009.

[15] D. M. Layfield, A. Agrawal, H. Roche, and R. I. Cutress, "Intraoperative assessment of sentinel lymph nodes in breast cancer," *British Journal of Surgery,* vol. 98, pp. 4-17, 2010.

[16] R. J. Menezes, H. C. Roberts, N. S. Paul, M. McGregor, T. B. Chung, D. Patsios, G. Weisbrod, S. Herman, A. Pereira, A. McGregor, Z. Dong, I. Sitartchouk, S. Boerner, M. S. Tsao, S. Keshavjee, and F. A. Shepherd, "Lung cancer screening using low-dose computed tomography in at-risk individuals: the Toronto experience," *Lung Cancer,* vol. 67, pp. 177-83, Feb 2010.

[17] J. C. Sieren, Y. Ohno, H. Koyama, K. Sugimura, and G. McLennan, "Recent technological and application developments in computed tomography and magnetic resonance imaging for improved pulmonary nodule detection and lung cancer staging," *J Magn Reson Imaging,* vol. 32, pp. 1353-69, Dec 2010.

[18] N. Y. Wu, H. C. Cheng, J. S. Ko, Y. C. Cheng, P. W. Lin, W. C. Lin, C. Y. Chang, and D. M. Liou, "Magnetic resonance imaging for lung cancer detection: experience in a population of more than 10,000 healthy individuals," *BMC Cancer,* vol. 11, p. 242, 2011.

[19] H. C. Suen, B. F. Meyers, T. Guthrie, M. S. Pohl, S. Sundaresan, C. L. Roper, J. D. Cooper, and G. A. Patterson, "Favorable results after sleeve lobectomy or bronchoplasty for bronchial malignancies," *Ann Thorac Surg,* vol. 67, pp. 1557-62, Jun 1999.

[20] C. Kotoulas, G. Lazopoulos, C. Foroulis, M. Konstantinou, P. Tomos, and A. Lioulias, "Wedge resection of the bronchus: an alternative bronchoplastic technique for preservation of lung tissue," *Eur J Cardiothorac Surg,* vol. 20, pp. 679-83, Oct 2001.

[21] Y. Ohta, T. Yachi, M. Oda, H. Sato, J. Shimizu, Y. Watanabe, and G. Watanabe, "Bronchial sleeve resection with complete preservation of the lung for carcinoma," *Respiration,* vol. 68, pp. 528-32, 2001.

[22] P. Thomas, C. Doddoli, S. Yena, X. Thirion, F. Sebag, P. Fuentes, and R. Giudicelli, "VATS is an adequate oncological operation for stage I non-small cell lung cancer," *Eur J Cardiothorac Surg,* vol. 21, pp. 1094-9, Jun 2002.

[23] M. Kara, S. Dizbay Sak, D. Orhan, and S. Kavukcu, "Proximal bronchial extension with special reference to tumor localization in non-small cell lung cancer," *Eur J Cardiothorac Surg,* vol. 20, pp. 350-5, Aug 2001.

[24] S. J. Maygarden, F. C. Detterbeck, and W. K. Funkhouser, "Bronchial margins in lung cancer resection specimens: utility of frozen section and gross evaluation," *Mod Pathol,* vol. 17, pp. 1080-6, Sep 2004.

[25] K. Kayser, E. Anyanwu, H. G. Bauer, and I. Vogt-Moykopf, "Tumor presence at resection boundaries and lymph-node metastasis in bronchial carcinoma patients," *Thorac Cardiovasc Surg,* vol. 41, pp. 308-11, Oct 1993.

[26] L. R. Kaiser, P. Fleshner, S. Keller, and N. Martini, "Significance of extramucosal residual tumor at the bronchial resection margin," *Ann Thorac Surg,* vol. 47, pp. 265-9, Feb 1989.

[27] G. Friedel, U. Pastorino, R. J. Ginsberg, P. Goldstraw, M. Johnston, H. Pass, J. B. Putnam, and H. Toomes, "Results of lung metastasectomy from breast cancer: prognostic criteria on the basis of 467 cases of the International Registry of Lung Metastases," *Eur J Cardiothorac Surg,* vol. 22, pp. 335-44, Sep 2002.

[28] H. Kreisman, N. Wolkove, H. S. Finkelstein, C. Cohen, R. Margolese, and H. Frank, "Breast cancer and thoracic metastases: review of 119 patients," *Thorax,* vol. 38, pp. 175-9, Mar 1983.

[29] G. Schreiber and D. C. McCrory, "Performance characteristics of different modalities for diagnosis of suspected lung cancer: summary of published evidence," *Chest,* vol. 123, pp. 115S-128S, Jan 2003.

[30] E. El-Bayoumi and G. A. Silvestri, "Bronchoscopy for the diagnosis and staging of lung cancer," *Semin Respir Crit Care Med,* vol. 29, pp. 261-70, Jun 2008.

[31] R. Gupta, A. Dastane, R. J. McKenna, Jr., and A. M. Marchevsky, "What can we learn from the errors in the frozen section diagnosis of pulmonary carcinoid tumors? An evidence-based approach," *Hum Pathol,* vol. 40, pp. 1-9, Jan 2009.

[32] J. Herbst, R. Jenders, R. McKenna, and A. Marchevsky, "Evidence-based criteria to help distinguish metastatic breast cancer from primary lung adenocarcinoma on thoracic frozen section," *Am J Clin Pathol,* vol. 131, pp. 122-8, Jan 2009.

[33] A. M. Marchevsky, C. Changsri, I. Gupta, C. Fuller, W. Houck, and R. J. McKenna, Jr., "Frozen section diagnoses of small pulmonary nodules: accuracy and clinical implications," *Ann Thorac Surg,* vol. 78, pp. 1755-9, Nov 2004.

[34] R. Siegel, D. Naishadham, and A. Jemal, "Cancer statistics, 2012," *CA Cancer J Clin,* vol. 62, pp. 10-29, Jan-Feb 2012.

[35] C. Black, J. Marotti, E. Zarovnaya, and J. Paydarfar, "Critical evaluation of frozen section margins in head and neck cancer resections," *Cancer,* vol. 107, pp. 2792-800, Dec 15 2006.

[36] A. Binahmed, R. W. Nason, and A. A. Abdoh, "The clinical significance of the positive surgical margin in oral cancer," *Oral Oncol,* vol. 43, pp. 780-4, Sep 2007.

[37] T. C. Chen, C. P. Wang, J. Y. Ko, T. L. Yang, and P. J. Lou, "The impact of pathologic close margin on the survival of patients with early stage oral squamous cell carcinoma," *Oral Oncol,* vol. 48, pp. 623-8, Jul 2012.

[38] T. R. Loree and E. W. Strong, "Significance of positive margins in oral cavity squamous carcinoma," *American Journal of Surgery,* vol. 160, pp. 410-4, Oct 1990.

[39] L. J. DiNardo, J. Lin, L. S. Karageorge, and C. N. Powers, "Accuracy, utility, and cost of frozen section margins in head and neck cancer surgery," *Laryngoscope,* vol. 110, pp. 1773-6, Oct 2000.

[40] S. M. Olson, M. Hussaini, and J. S. Lewis, Jr., "Frozen section analysis of margins for head and neck tumor resections: reduction of sampling errors with a third histologic level," *Mod Pathol,* vol. 24, pp. 665-70, May 2011.

[41] A. Brander, P. Viikinkoski, J. Nickels, and L. Kivisaari, "Thyroid gland: US screening in a random adult population," *Radiology,* vol. 181, pp. 683-7, Dec 1991.

[42] J. N. Bruneton, C. Balu-Maestro, P. Y. Marcy, P. Melia, and M. Y. Mourou, "Very high frequency (13 MHz) ultrasonographic examination of the normal neck: detection of normal lymph nodes and thyroid nodules," *J Ultrasound Med,* vol. 13, pp. 87-90, Feb 1994.

[43] J. Woestyn, M. Afschrift, K. Schelstraete, and A. Vermeulen, "Demonstration of nodules in the normal thyroid by echography," *Br J Radiol,* vol. 58, pp. 1179-82, Dec 1985.

[44] D. S. Tyler, D. J. Winchester, N. P. Caraway, R. C. Hickey, and D. B. Evans, "Indeterminate fine-needle aspiration biopsy of the thyroid: identification of subgroups at high risk for invasive carcinoma," *Surgery,* vol. 116, pp. 1054-60, Dec 1994.

[45] H. Gharib, "Fine-needle aspiration biopsy of thyroid nodules: advantages, limitations, and effect," *Mayo Clin Proc,* vol. 69, pp. 44-9, Jan 1994.

[46] E. A. Mittendorf, A. Khiyami, and C. R. McHenry, "When fine-needle aspiration biopsy cannot exclude papillary thyroid cancer: a therapeutic dilemma," *Arch Surg,* vol. 141, pp. 961-6; discussion 966, Oct 2006.

[47] G. F. Huber, P. Dziegielewski, T. W. Matthews, S. J. Warshawski, L. M. Kmet, P. Faris, M. Khalil, and J. C. Dort, "Intraoperative frozen-section analysis for thyroid nodules: a step toward clarity or confusion?," *Arch Otolaryngol Head Neck Surg,* vol. 133, pp. 874-81, Sep 2007.

[48] R. Asari, B. E. Niederle, C. Scheuba, P. Riss, O. Koperek, K. Kaserer, and B. Niederle, "Indeterminate thyroid nodules: a challenge for the surgical strategy," *Surgery,* vol. 148, pp. 516-25, Sep 2010.

[49] D. Huang, E. A. Swanson, C. P. Lin, J. S. Schuman, W. G. Stinson, W. Chang, M. R. Hee, T. Flotte, K. Gregory, C. A. Puliafito, and J. G. Fujimoto, "Optical Coherence Tomography," *Science,* vol. 254, pp. 1178-1181, Nov 22 1991.

[50] W. Drexler, U. Morgner, R. K. Ghanta, F. X. Kärtner, J. S. Schuman, and J. G. Fujimoto, "Ultrahigh-resolution ophthalmic optical coherence tomography," *Nature Medicine,* vol. 7, pp. 502-507, Apr 2001.

[51] L. M. Sakata, J. DeLeon-Ortega, V. Sakata, and C. A. Girkin, "Optical coherence tomography of the retina and optic nerve - a review," *Clinical and Experimental Ophthalmology,* vol. 37, pp. 90-99, Jan-Feb 2009.

[52] W. Geitzenauer, C. K. Hitzenberger, and U. M. Schmidt-Erfurth, "Retinal optical coherence tomography: past, present and future perspectives," *British Journal of Ophthalmology,* vol. 95, pp. 171-177, Feb 2011.

[53] G. J. Tearney, M. E. Brezinski, B. E. Bouma, S. A. Boppart, C. Pitris, J. F. Southern, and J. G. Fujimoto, "In vivo endoscopic optical biopsy with optical coherence tomography," *Science,* vol. 276, pp. 2037-9, Jun 27 1997.

[54] B. E. Bouma, G. J. Tearney, C. C. Compton, and N. S. Nishioka, "High-resolution imaging of the human esophagus and stomach in vivo using optical coherence tomography," *Gastrointest Endosc,* vol. 51, pp. 467-74, Apr 2000.

[55] X. D. Li, S. A. Boppart, J. Van Dam, H. Mashimo, M. Mutinga, W. Drexler, M. Klein, C. Pitris, M. L. Krinsky, M. E. Brezinski, and J. G. Fujimoto, "Optical coherence tomography: advanced technology for the endoscopic imaging of Barrett's esophagus," *Endoscopy,* vol. 32, pp. 921-30, Dec 2000.

[56] M. V. Sivak, K. Kobayashi, J. A. Izatt, A. M. Rollins, R. Ung-runyawee, A. Chak, R. C. K. Wong, G. A. Isenberg, and J. Willis, "High-resolution endoscopic imaging of the GI tract using optical coherence tomography," *Gastrointestinal Endoscopy,* vol. 51, pp. 474-479, Apr 2000.

[57] W. Hatta, K. Uno, T. Koike, S. Yokosawa, K. Iijima, A. Imatani, and T. Shimosegawa, "Optical coherence tomography for the staging of tumor infiltration in superficial esophageal squamous cell carcinoma," *Gastrointestinal Endoscopy,* vol. 71, pp. 899-906, May 2010.

[58] M. J. Suter, P. A. Jillella, B. J. Vakoc, E. F. Halpern, M. Mino-Kenudson, G. Y. Lauwers, B. E. Bouma, N. S. Nishioka, and G. J. Tearney, "Image-guided biopsy in the esophagus through comprehensive optical frequency domain imaging and laser marking: a study in living swine," *Gastrointestinal Endoscopy,* vol. 71, pp. 346-353, Feb 2010.

[59] C. Zhou, T. H. Tsai, H. C. Lee, T. Kirtane, M. Figueiredo, Y. K. Tao, O. O. Ahsen, D. C. Adler, J. M. Schmitt, Q. Huang, J. G. Fujimoto, and H. Mashimo, "Characterization of buried glands before and after radiofrequency ablation by using 3-dimensional optical coherence tomography (with videos)," *Gastrointest Endosc,* vol. 76, pp. 32-40, Jul 2012.

[60] G. J. Tearney, M. E. Brezinski, J. F. Southern, B. E. Bouma, S. A. Boppart, and J. G. Fujimoto, "Optical biopsy in human gastrointestinal tissue using optical coherence tomography," *Am J Gastroenterol,* vol. 92, pp. 1800-4, Oct 1997.

[61] I. K. Jang, B. E. Bouma, D. H. Kang, S. J. Park, S. W. Park, K. B. Seung, K. B. Choi, M. Shishkov, K. Schlendorf, E. Pomerantsev, S. L. Houser, H. T. Aretz, and G. J. Tearney, "Visualization of coronary atherosclerotic plaques in patients using optical coherence tomography: Comparison with intravascular ultrasound," *Journal of the American College of Cardiology,* vol. 39, pp. 604-609, Feb 20 2002.

[62] P. Barlis, G. van Soest, P. W. Serruys, and E. Regar, "Intracoronary optical coherence tomography and the evaluation of stents," *Expert Review of Medical Devices,* vol. 6, pp. 157-167, Mar 2009.

[63] H. G. Bezerra, M. A. Costa, G. Guagliumi, A. M. Rollins, and D. I. Simon, "Intracoronary optical coherence tomography: a comprehensive review clinical and research applications," *JACC Cardiovasc Interv,* vol. 2, pp. 1035-46, Nov 2009.

[64] J. L. Gutierrez-Chico, E. Alegria-Barrero, R. Teijeiro-Mestre, P. H. Chan, H. Tsujioka, R. de Silva, N. Viceconte, A. Lindsay, T. Patterson, N. Foin, T. Akasaka, and C. di Mario, "Optical coherence

tomography: from research to practice," *European Heart Journal-Cardiovascular Imaging,* vol. 13, pp. 370-384, May 2012.

[65] J. A. Izatt, M. R. Hee, G. M. Owen, E. A. Swanson, and J. G. Fujimoto, "Optical coherence microscopy in scattering media," *Opt Lett,* vol. 19, pp. 590-2, Apr 15 1994.

[66] J. A. Izatt, M. D. Kulkarni, H. W. Wang, K. Kobayashi, and M. V. Sivak, "Optical coherence tomography and microscopy in gastrointestinal tissues," *Ieee Journal of Selected Topics in Quantum Electronics,* vol. 2, pp. 1017-1028, Dec 1996.

2. Lower GI pathologies and Endoscopic Imaging Methods

2.1. Background on Lower GI Diseases

Based on our groups longstanding collaboration with Drs. Hiroshi Mashimo, MD, PhD and Qin Huang, MD, PhD, at Department of Gastroenterology at the VA Boston Healthcare System, as well as Dr. James Connolly, MD, at Department of Pathology at the Beth Israel Deaconess Medical Center (BIDMC), and the scope of some of the major National Institute of Health (NIH) grants that financially supports us, our group puts a strong emphasis on OCT and OCM applications for diseases related to human GI tract. In the past, the focus of the research of our group was to identify and survey a set of premalignant conditions mainly related to upper GI tract. Earlier studies have confirmed the utility of OCT by showing correlation between OCT images and histological appearance of related upper GI architectures, such as squamous epithelium, Barrett's esophagus (BE), low and high grade dysplasia (LGD, HGD), and adenocarcinoma [1-5]. In a study with 55 patients, a blinded read of OCT and corresponding histology images has shown a sensitivity of 83% and specifity of 75% for detecting HGD and intramucosal carcinoma [6]. Although in this study HGD and advanced carcinoma was grouped together, the main clinical challenge is to distinguish Barrett's epithelium with dysplasia from BE without dysplasia, as adenocarcinoma and intramucosal carcinoma is readily identifiable by endoscopy. In a prospective, double blinded study with 33 patients, the utility of OCT for detecting dysplastic BE is found to be relatively low with a sensitivity of 68% and specifity of 82% [7]. Another study investigated methods for computer aided classification techniques for identifying dysplasia and found a sensitivity of 82% and specifity of 74% for a relatively low patient population of 13 patients [8].

Note that earlier endoscopic OCT studies have utilized imaging catheters wit relatively low resolution (~10 - 15 um), which might have impacted the low diagnostic accuracy observed in those studies. Subsequently, with the advent of broadband, high speed swept source lasers and improved imaging catheters, high resolution (9 um transverse and 7 um axial) imaging has been demonstrated *in vivo* [9]. Furthermore, pilot studies utilizing Doppler OCT methods have shown characteristic flow patterns related to normal esophagus, Barrett's esophagus and adenocarcinoma [10]. Moreover, using a balloon based imaging catheter, comprehensive surveillance of long segments of esophagus (> 5 cm) has been performed [11, 12]. More recently, using the unique advantage of OCT imaging which provides depth resolved images, our group have demonstrated the high prevalence of "buried" BE glands for the patients undergoing radiofrequency ablation (RFA), which are invisible during standard white light endoscopy (WLE) and has been argued to have malignant potential [13]. In another study, we found a correlation between the quantity of these buried glands and the efficacy of the RFA treatment [14]. Furthermore, the same study also showed a correlation between the thickness

of the Barrett's epithelium and the success of the subsequent treatment response. With the substantial increase in the axial and transverse resolutions, as well as the imaging speed of the new generation OCT systems, it can be expected that more studies will be conducted on upper GI diseases to further tackle the long standing clinical challenges such as detecting dysplasia in BE patients and improving the efficacy of treatment strategies.

Recently, the interest of our group in lower GI pathologies has been grown due to long standing and emerging clinical challenges related to some of the highly prevalent colorectal diseases. It is our belief that OCT and OCM imaging have several distinguishing features, such as high resolution, depth resolved imaging capability, deep tissue penetration and non-reliance on external contrast agents, which can make these imaging modalities promising technologies in tackling some of the issues faced in the management of a major subset of lower GI diseases. In the following sections, three of these diseases will be analyzed by highlighting the clinical challenge and indicating limitations of WLE for these particular applications. Note that, in the following the terms endoscopy and colonoscopy will be used interchangeably where both refer to conventional endoscopic procedure performed with WLE.

i. Detection of Non-polypoid (flat) Lesions

With 103,170 estimated new cases in 2012, colorectal carcinoma (CRC) is the third most common cancer, as well as the third most common cause of cancer related deaths for both sexes in the U.S. [15, 16]. Approximately two-thirds of all CRC cases progresses through a relatively well defined pathway, which involves the transformation from normal epithelium to low-grade dysplastic adenoma, and then to protruding adenoma with high grade dysplasia or villous component, which finally progresses to invasive cancer, accompanied by a series of genetic mutations, including mutations in APC, KRAS and p-53 genes [17, 18]. For the case of a well defined protruding lesion, a polypectomy procedure is performed to remove the adenomatous lesions. The latest update on the National Polyp Study, an ongoing randomized trial (starting from 1990) to evaluate effective surveillance of patients discovered to have colorectal adenomas, demonstrated a reduction of 53% in CRC related mortality with colonoscopic polypectomy (population wide mortality was 0.46% vs. 0.97% for with and without polypectomy, respectively) [19]. Similar to the result of this study, several other studies in U.S. and other nations proved the effectiveness of colonoscopy as a screening tool, with a reduced CRC incidence rate of 29-77% [20-23].

Non-polypoid colorectal neoplasms (NP-CRNs) depicted in Fig. 1, on other hand, show only slight morphological difference from the surrounding epithelium, making it harder to detect using conventional endoscopic imaging modalities [24, 25]. Although several definition exist on what constitutes this category of polyps, a polyp whose height is no more than its diameter or, more quantitatively, polyps with less than 3 mm vertical elevation are usually

considered as flat lesions [26, 27]. Tied to the challenges for the detection of the non-polypoid lesions, the population wide prevalence of these category of polyps is not well known, yet a range of numbers between 7% to 45% exist for the prevalence of these lesions, with a clear increasing trend as more advanced imaging methods are employed aiding the detection of these lesions [28-32]. Moreover, these lesions is shown to exist throughout the lower GI tract, 58% of which residing in the left colon and 42% residing in the right or transverse colon [32].

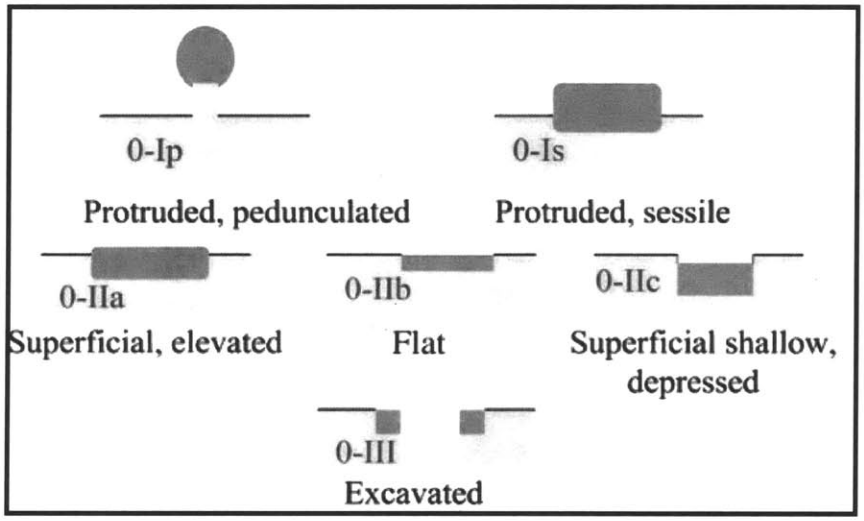

Figure 1: Schematic representation of major variants of colonic lesions. 0-Ip and 0-Is represents polypoid lesions, readily identifiable by WLE. 0-IIa, 0-IIb and 0-IIc, on the other hand, are non-polypoid lesions and they are harder to detect using standard endoscopic imaging modalities. Figure is modified from [33].

In a cross sectional study with 1,819 patients undergoing elective colonoscopy, the malignant potential of NP-CRNs have been found to be much higher than polypoid lesions, with an odds ratio of 9.78 (95% CI, 3.93 – 24.4) for the likelihood of containing carcinoma [34]. In the same study, non-polypoid lesions accounted for 54% of superficial carcinomas. Moreover, about 8.6% of the non-polypoid lesions was categorized as depressed lesion, with a risk of malignancy as high as 33% [34]. Several other studies confirmed the higher malignancy of the depressed lesions, by showing that 75% of all early CRCs have a depressed component, and 29.5% of all depressed lesions are malignant irrespective of size, with the overall risk of carcinoma increasing above 80% when the size of the lesion is larger than 15 mm [35, 36].

Despite its extremely high potential of malignancy and its high prevalence among population, the miss rates of the non-polypoid lesions during WLE are very high, even when the endoscopy procedure is conducted by expert endoscopists. In a retrospective study with 76 colonoscopy pairs it has been found that 17% of patients had one or more neoplastic polyps missed in the initial imaging session [37]. Other retrospective studies confirmed the high miss rate of WLE, especially for the flat appearing lesions [38, 39]. Furthermore, several prospective

studies that featured back to back colonoscopy by two different endoscopists demonstrated that about 16-27% of small polyps (<5 mm) falling into this category are missed by WLE [40, 41]. Hence it is clear that there is a need for an imaging modality that will increase the yield of surveillance endoscopy for the detection of the non-polypoid lesions.

ii. Differentiation Between Forms of IBD

Chron's disease (CD) and Ulcerative colitis (UC) constitutes two major forms of chronic inflammatory bowel disease (IBD), with an estimated number of 1.5 million total cases in the U.S. [42, 43]. The chronic nature of this disease manifest itself as a significant economical burden, producing a total of $6.3 billion annual cost for IBD-associated treatment in U.S. [44].

For an established IBD case, the differential diagnosis between CD and UC is crucial, as the clinical management and prognosis for these two forms of IBD are vastly different. For instance, antibiotics are shown to be more effective in CD patients compared to UC patients [45]. Moreover, for UC patients, surgical intervention to remove the inflammatory lesion followed by an ileal puch-anal anstomosis (IPAA) procedure is considered as an effective treatment, whereas CD is generally considered incurable, and the management strategies focus on maintaining symptomatic control, improving quality of life and minimizing short and long term toxicity as well as complications [46, 47]. As an example, the IPAA procedure performed on CD patients result in pouch complications in as high as 40% of patients [48].

There are several morphological and structural features that aid in the differentiation between these two forms of IBD. In general, UC involves the rectum and might affect part or the entire colon in a continuous pattern, with inflammation mainly limited to the mucosa layer. On the other hand, any site of the lower GI tract can be affected with CD, but it is most common to the ileum and colon with a skip or patchy involvement [49]. Different form UC, CD is characterized with a transmural inflammation and often associated with intestinal granulomas, strictures, and fistrulas [42, 43].

Despite many clinical, anatomic and histologic distinctions, there is still no gold standard of diagnosis between these two forms of IBD [50]. Consequently, several prospective and retrospective studies have shown that in 5-15% of cases a definite distinction between UC and CD can not be made, and the disease is classified as indeterminate colitis (IC) [51, 52]. Even when an endoscopic resection is performed, the pathological diagnosis is correct only in 87% of cases [53]. Several serologic, proteomic and genetic analyses were also tested for the differentiation between the two forms of IBD, however, their sensitivity remain too low for them to be adapted into the standard of care [54-56]. Therefore, it is clear that an imaging modality that will enable accurate differential diagnosis between UC and CD will make a significant impact on the clinical management of IBD.

iii. Detecting Dysplasia in IBD Patients

The prognosis for CRC patients with a history of longstanding IBD is shown to be worse by population based studies, with a mortality rate ratio of 1.24 for UC patients and with a hazard ratio of 1.82 for CD patients, compared to CRC patients without IBD [57, 58]. Furthermore, several studies established the increased risk of developing CRC for IBD patients. A large meta-analysis based on 194 studies showed the risk of cancer for UC patients as 2% after 10 years, and as high as 18% after 30 years of long standing disease [59]. A similar risk factor has been reported in another prospective follow up study with 600 patients (2.5% at 20 and 10.8% at 40 years) [60]. Similar population based studies and meta-analyses conducted with CD patients confirmed an increased risk of developing CRC equal to UC patients [61, 62]. There are also some recent studies, however, which suggest a decrease in the absolute risk of developing CRC in IBD patients, which might be attributed to more comprehensive surveillance programs or the effect of anti-inflammatory medications [63-65]. Several risk factors such as duration of the disease, degree of inflammation, concurrent diagnosis of primary sclerosing cholangitis (PSC), family history, gender, and age of onset of the IBD has been associated with an increased risk of developing CRC for IBD patients [60, 66-69].

Due to high risk of developing CRC, current American Gastroenterology Association (AGA) guidelines recommends screening colonoscopy for IBD patients with 1-3 year intervals, at a maximum of 8 years after onset of the disease, which consists of obtaining 4 quadrant random biopsy specimens every 10 cm throughout the entire colon [70]. However, this approach is prone to sampling errors as several studies showed that in 50-80% of cases with colitis-associated neoplasms, the lesions are not visible upon WLE [71]. One study with 590 patients who underwent proctocolectomy showed that preoperative colonoscopy led to the correct identification of the lesion only in 39.7% of cases, and the positive predictive value of finding preoperative dysplasia of any grade was 50% [72]. A meta analysis conducted on 10 prospective studies with a total of 1,225 patients showed that 37% of patients with indefinite results for malignancy during colonoscopy progressed to high grade dysplasia or cancer [71]. Therefore, to date, no randomized prospective studies have shown that surveillance colonoscopy indeed reduces the risk of CRC development in IBD patients [73].

The purpose of surveillance in IBD patients is to detect dysplastic progression of the mucosa, as this is thought to be the best marker for CRC risk in IBD patients [74]. Lesions suspicious for dysplasia are categorized into dysplasia associated lesion or mass (DALM) or adenoma like mass (ALM). The differential diagnosis of the suspected lesion between these two categories is critical for the clinical management of the disease. For ALM, polypectomy is considered to be a successful tool for the removal of malignancy based on the results of several studies [75-77]. Even in the case of high grade dysplasia, endoscopic resection is shown to have

no significant excess risk for the development of CRC for the IBD patients with ALM [78]. On the other hand, DALM is shown to correlate with synchronous or metachronous carcinoma, and involvement of invasive carcinoma is shown in up to half of cases. Hence, colectomy is the standard of care for the IBD patients with a diagnosed DALM [70]. Note that in both cases removal of the entire dysplastic lesion is essential. Especially for the case of endoscopic resection, residual flat dysplastic lesion around the boundaries of the primary lesion is shown to develop into CRC in almost 40% of cases [79].

Despite the importance of differentiating between DALM and ALM, pathological differences between these two lesions are rather subtle such that making a correct diagnosis during the endoscopy procedure is a major concern [80]. Unfortunately, WLE performs poorly for this purpose, as prospective studies have shown an accuracy of 68% and 75% for the correct diagnosis of ALM and DALM, respectively, even when the diagnosis is made by an expert pathologist [81, 82]. For academic gastroenterologists, who are argued to have less endoscopic work load and experience, the accuracy decreases to as low as 58% and 56% for the correct diagnosis between ALD and DALM, respectively [81]. Hence there is a marked need for an imaging technology that will aid in differentiation of DALM from ALM, and increase the yield in detecting dysplasia in IBD patients.

2.2. Advanced Imaging Techniques for Management of Lower GI Diseases

In the previous section a set of diseases related to lower GI tract has been described, where the utility of conventional WLE is limited in the diagnosis and management of the related condition. In the past decades, several imaging modalities have been developed and applied to the realm of endoscopic imaging, in an attempt to increase the yield of the lower GI surveillance strategies. In this section, a review of some of the most promising endoscopic imaging modalities will be given with a special emphasis of their advantages, limitations, results of controlled comparison studies, and the adaptation of the related technologies into the GI community.

Identification of Fine Surface Structures (Pit Patterns) of the Colonic Mucosa

One of the characteristics of the colon is the presence of well defined crypt like structures (pit patterns) that lines the superficial layer of the colonic mucosa [83]. Although too small to be discernible with conventional WLE, the advent of the advanced imaging modalities such as magnification endoscopy, narrow band imaging (NBI) and chromoendoscopy made it possible to observe these structures during the endoscopic session. Hence, several classification schemes have been developed in conjunction with the exploration of the various types of crypt patterns and the underlying pathological condition [84]. Among these, the classification scheme developed by Kudo et al. has gained widespread acceptance within the GI community, hence

"Kudo's pit pattern" became the common nomenclature for describing the category of the colonic crypt structures [85, 86].

Figure 2 depicts the Kudo classification of colonic pit patterns that is widely used in the GI community. In this figure, Type - I refers to roundish crypt structure where each crypt has about 0.07 $\pm$ 0.02 mm diameter [84]. This type of pit pattern is the characteristic of normal colonic mucosa. Type – II, on the other hand, consists of larger pits with a diameter of 0.09 $\pm$ 0.02 mm, where the crypts have stellar of papillary appearance. This type of pit pattern is associated with the presence of a hyperplastic polyp with an accuracy of as high as 95.5% [87]. The elongated roundish pits in Type – IIIL have a diameter of 0.22 $\pm$ 0.09. On the other hand, Type – IIIS consists of smaller (diameter of 0.03 $\pm$ 0.01 mm) elongated roundish pits. Adenomas with a Type – IIIL pit pattern account for the majority of colorectal neoplasms, whereas Type – IIIS is usually associated with the presence of a depressed lesion [88]. Type – IV features the largest crypts with a diameter of 0.93 $\pm$ 0.32 mm that are typically in branched form. Finally, Type – V pit pattern consists of disarrayed crypt structures that do not show any structural characteristics. The malignancy potential of Type – IV and Type – V pit pattern is shown to be very high, where Type – IV typically belongs to a protruded tumor and Type – V is often associated with submucosal or advanced carcinoma [88-91].

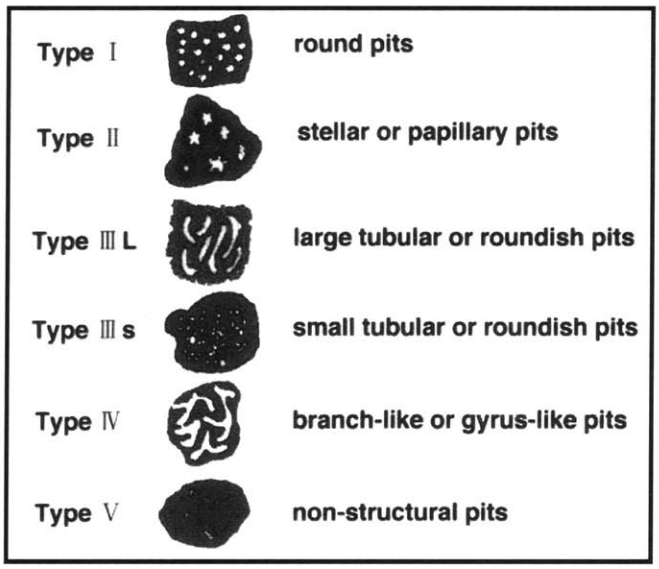

Figure 2: Classification of colonic pit patterns developed by Kudo et al. Figure is modified from [89].

Due to this intimate relationship between the morphology of the colonic pit patterns and the histopathological state of the tissue, the main objective of some the imaging modalities that will be discussed next will be to provide necessary contrast and magnification to enhance the visualization of the pit patterns during the endoscopy procedure.

i. Narrow Band Imaging (NBI)

In narrowband imaging, the tissue is illuminated by two discrete signal bands, one centered at 450 nm (440-460 nm), and the other band centered at 550 nm (540 – 560 nm) [92]. It is well known that hemoglobin has high absorption at these spectral bands. Hence, light will be attenuated from the vessels and capillaries, which will result in enhanced identification of the mucosal surface patterns. Figure 3 demonstrates the utility of NBI in terms of enhancing the contrast of the colonic architecture. Especially the magnified views shown in Fig. 3 (C) and (F) shows clear delineation of irregular pit patterns and the vascular network. Note that, in terms of instrumentation, only two narrowband optical filters are required, hence this method can be readily integrated into existing endoscopes. Hence, newer models of the endoscopes and colonoscopes from major endoscope manufactures indeed feature this imaging modality.

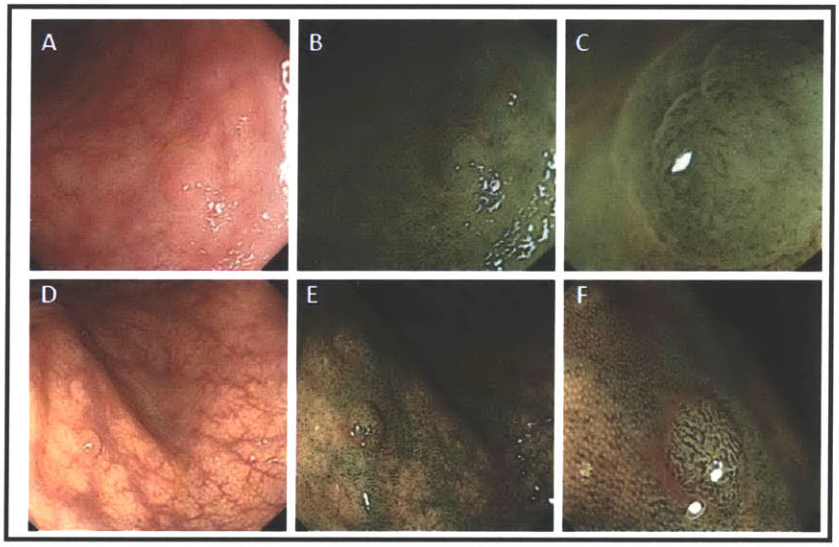

Figure 3: Enhanced visualization of colonic architecture and vessels due to NBI. (A) to (C) show a 3 mm sessile hyperplastic polyp whereas (D) to (F) show a 4 mm sessile adenoma. (A,D) are taken with WLE, (B,E) are taken with NBI and (C,F) are taken with NBI with magnification. Figure is modified from [93].

Due to its increased contrast for the surface morphology, initially there was a high optimism for the utility of NBI for the detection of polypoid and non-polypoid adenomas [94]. However, subsequent large scale randomized control studies have shown no significant increase in the adenoma detection rates with NBI. A study conducted by a single endoscopist on 434 patients resulted in an adenoma detection rate of 65% with NBI as compared to 67% with WLE [95]. Moreover, no significant improvement in the flat lesion detection rate is noted in the same study. In another prospective randomized control study, conducted by 7 endoscopists with no prior NBI experience, the detection rate of adenomas for NBI and WLE was as low as 23% and 17%, respectively [96]. Another recent multicenter study involving 1,256

patients, conducted by 6 experienced endoscopists with some prior NBI experience, has shown the detection rate as 33% with NBI and 37% with WLE [97]. Note that in these studies adenoma detection rates are defined as the number of patients that have been detected to have adenomas divided by the total number of the patients in the study.

There are also some tandem studies that showed a slight increase in the adenoma detection rates with NBI. In one study with 62 patients, single experienced endoscopists performed WLE followed by NBI. The results showed that the adenoma detection rates are 27% for NBI whereas it is 15% for WLE [98]. In a larger scale study 276 patients have been randomized to either WLE or NBI examination [99]. Afterwards, all patients have been underwent a second procedure with WLE as the reference standard. The adenoma detection rates are shown only marginally higher for NBI (50% with NBI vs. 44% for WLE). Note that despite the results showing some improvement for the adenoma detection rate with NBI for the tandem studies, these studies have been criticized as blinding of the endoscopists is not possible due to the nature of the study [94]. Overall, a pooled analysis on different studies concluded that NBI is only marginally better than WLE for adenoma detection [100].

Although it seems that NBI might have less utility in the detection of lesions, it might have a better potential in characterization and differentiation of colonic lesions. In one prospective comparative study with 133 patients, the diagnostic accuracy of NBI is shown to be significantly higher than WLE (p = 0.04 and p = 0.004 for two different readers) and it was comparable to that of chromoendoscopy [101]. In this study sensitivity and specifity of NBI was 87%/88% and 95%/71%, respectively, for reader 1/reader 2, as opposed to being 62%/65% and 85%/74%, respectively, for WLE. Yet in another prospective comparative study with 78 patients, the sensitivity and specifity of NBI for differential diagnosis of neoplastic (adenoma, adenocarcinoma) and non-neoplastic (hyperplastic) polyps was 95.7% and 87.5%, respectively, with an overall diagnostic accuracy of 92.7% [102]. The sensitivity and specificity of WLE for the same diagnosis was significantly lower in the same study (82.9% sensitivity, 80% specifity). Several other smaller scale studies have further confirmed the utility of NBI for the differential diagnosis of the colorectal lesions [98, 103, 104]. Note that, in some of these studies the appearance of the vessel structures has been taken into consideration in addition to pit patterns. Due to the high hemoglobin absorption at the illumination wavelengths, as previously mentioned, NBI also enhances the visualization of the vessel and capillaries by this negative contrast mechanism. Hence, it should be emphasized that this advantage of NBI can provide additional diagnostic information.

The utility of NBI for detection of dysplasia in IBD patients is not studied in detail. One of the few studies on this subject has shown that NBI detects neoplastic lesions at a rate comparable to WLE (24% and 23% for NBI and WLE, respectively) [105]. However, this study

utilized an early generation NBI system. It is argued that the newer generation NBI systems, combined with magnification endoscopy, can enhance the detection of dysplasia for IBD patients [106].

ii. Chromoendoscopy

Chromoendoscopy involves the topical application of specific dyes to enhance the visualization, characterization and diagnosis of mucosal surface structures [107]. As it is the case with NBI, it does not require any sophisticated equipment and can be readily performed using standard endoscopes. The application of the dye requires a spraying catheter, introduced through the working channel of the endoscope. For diagnosis purposes the dyes can be sprayed solely onto the suspected lesions, whereas for detection of lesions they can be sprayed homogeneously throughout the colon, a procedure termed as pancolonic chromoendoscopy [108].

There are three commonly used Chromoendoscopy dyes in the GI tract that can be broadly categorized into either absorptive (vital) or contrast stains [109]. Absorptive dyes include Lugol's iodine and methylene blue. Lugol's iodine has an affinity for glycogen in nonkeratinized squamous epithelium. Normal squamous epithelium stains with black or brown colors, whereas an abnormal stain pattern indicates a condition related to the disruption of the epithelial structure. Hence it is commonly used for diseases related to upper GI tract, namely esophagus, whose characteristic lining consists of squamous epithelium. Consequently, several studies have established its efficacy on the detection of esophageal malignancies, with a sensitivity reaching to 96% for the detection of high grade dysplasia or cancer for squamous cell carcinoma of the esophagus [110, 111]. On the other hand, methylene blue is taken up by actively absorbing tissues such as small intestinal and colonic epithelium and does not stain non absorptive epithelia such as esophageal mucosa. Hence, the presence of this stain in the esophagus highlights malignancy, whereas lack of stain in the colon can be related to the presence of a metaplastic, neoplastic or inflammatory change [112-114]. Methylene blue has been used in a variety of GI applications, which includes improving the diagnosis of early gastric cancer, highlighting mucosal changes in celiac disease, detection of intestinal metaplasia in Barrett's esophagus, detection of colonic neoplasia, and differentiating between neoplastic and non-neoplastic lesions in IBD patients [114-118]. Figure 4 demonstrates the utility of chromoendoscopy in detecting the regions in the esophagus that have abnormal epithelial lining.

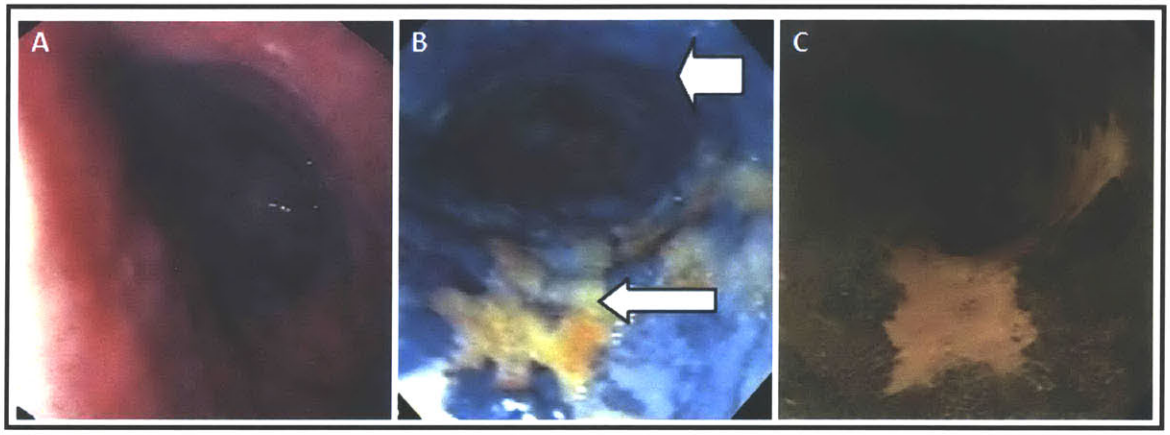

Figure 4: Enhanced visualization of mucosal architecture with chromoendoscopy. (A) is a WLE image of a BE patient with high grade dysplasia whereas (B) is the chromoendoscopy image of the same region after the methylene blue stain whereas (C) shows a region with squamous cell carcinoma of the esophagus after Lugol's iodine. Figure is modified from [119].

Indigocarmine, as opposed to the absorbing stains mentioned previously, pools into the mucosal cervices and pits, highlighting the fine features of the surface topography [109]. As shown in Fig. 5, pit patterns are clearly delineated with chromoendoscopy using the indigocarmine stain. Because of its superiority in defining irregularities in the mucosal architecture, it has been widely used for the detection and diagnosis of colorectal lesions. Note that, unless otherwise noted, all the chromoendoscopy studies described next were conducted with Indigocarmine as the staining agent.

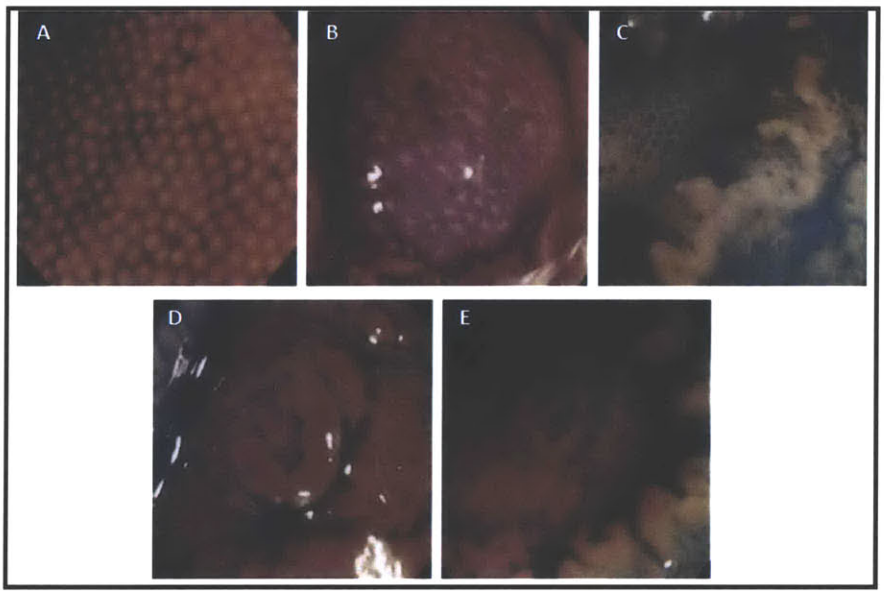

Figure 5: Visualization of pit patterns with Chromoendoscopy stained with indigocarmine. (A) to (E) show Type – I, Type – II, Type – IIIs, Type – IIIL and Type – V Kudo pit pattern, respectively. Figure is modified from [89].

As was the case with NBI, studies have shown a high diagnostic accuracy of chromoendoscopy for the differentiation between colonic lesions. In one large scale retrospective study consisting of images from 923 polyps, the sensitivity and specifity of chromoendoscopy for the differential diagnosis between neoplastic and non-neoplastic lesions is found to be 92% and 73.3%, respectively, with an overall diagnostic accuracy of 88.4% [120]. In another retrospective landmark study involving 3,438 lesions from 4,445 patients have shown that the diagnostic accuracy of chromoendoscopy is 75% for non-neoplastic lesions, 94% for adenomatous polyps, and 85% for invasive carcinoma [121]. In another large scale prospective study with 954 polyps, the sensitivity and specifity of chromoendoscopy for comparing histologically confirmed neoplastic lesions to non-neoplastic lesions was found to be 90.8% and 72.7%, respectively [122]. Several other studies have confirmed the diagnostic accuracy of chromoendoscopy for the classification of colorectal lesions [123-126]. A pooled meta analysis including 27 of the large scale studies on this subject has indicated the sensitivity and specifity of chromoendoscopy for differentiating between malignant and non-malignant lesions as 94% (95% CI, 92% - 95%) and 82% (95% CI, 72% - 88%), respectively [127].

The utility of chromoendoscopy for the detection of non-polypoid lesions is more promising than NBI discussed in the previous section. In one of the largest randomized multi center control trials on this subject, which included 1,008 patients randomized to chromoendoscopy (N = 496) and WLE control (N = 512) groups, it has been shown that pancolonic chromoendoscopy has increased the overall detection rate for protruded adenomas (0.95 vs. 0.66 per patient), flat adenomas (0.56 vs. 0.28 per patient) as well as serrated lesions (1.19 vs. 0.49 per patient, $p<0.001$) [128]. Another randomized control study involving 660 patients have also found increased detection rates for flat adenoma (0.6 vs. 0.4 per patient, $p = 0.01$), for adenoma smaller than 5 mm (0.8 vs. 0.7 per patient, $p = 0.03$), and for non-neoplastic lesions (1.8 vs. 1 per patient , $p<0.0001$) with chromoendoscopy compared to WLE [129]. Note that, the yield of detection of advanced neoplasia with chromoendoscopy was found similar to WLE in the same study. Several other prospective control studies have been confirmed the efficacy of chromoendoscopy in detecting lesions not discernible under conventional WLE [130-132].

Chromoendoscopy is also shown to be a promising modality for the detection and classification of dysplasia in IBD patients. In a single arm study involving 117 surveillance colonoscopies, chromoendoscopy is shown to have a sensitivity of 85.7% and specifity of 88.5% for the differential diagnosis between low grade dysplasia (LGD) and high grade dysplasia (HGD)/carcinoma (CA) for IBD lesions [133]. In another, prospective tandem study which involved back to back colonoscopies, where standard WLE is followed by chromoendoscopy, 114 additional abnormalities from 55 patients have been identified by chromoendoscopy, all of which were considered to be adenomas [134]. This study further revealed a statistically

increased dysplasia detection rate and increased yield for targeted biopsies due to the application of chromoendoscopy. In one of the landmark studies on this subject, which consisted of a randomized controlled trial involving 262 IBD patients, significantly more intraepithelial neoplasia were detected in the chromoendoscopy group compared to the conventional WLE group (32 vs. 10, $p = 0.003$) [114]. Furthermore, using the Kudo pit pattern classification, the sensitivity and specifity for differentiation between neoplastic and non-neoplastic lesions is reported as 93% in the same study. Several other studies further validated the utility of chromoendoscopy for the endoscopic management of IBD patients [135, 136].

The advantages of chromoendoscopy discussed in this section are offset by an increase in procedure time, higher cost and a labor intensive procedure. Apart from the time required for spraying of the stain, especially for the case of pancolonic chromoendoscopy, an extremely high quality bowel preparation is also required for the procedure to be successful. In a study described earlier, as high as 158 patients among the total study population of 1,008 patients had been excluded from the study solely based on inadequate bowel preparation [128]. It has been also argued that the gain in the adenoma detection rates can be due to improvements in the standard endoscopy technology, such as the introduction of high definition endoscopy and magnification endoscopy [137]. Furthermore, the false negative rate of this technique, being as 5.7% in the pooled meta-analysis for the assessment of colorectal neoplasms, has been criticized as unacceptably high [127]. All in all, due to these apparent limitations, chromoendoscopy has not been integrated yet into the routine clinical practice [94].

iii. Confocal Laser Endomicroscopy

Confocal microscopy utilizes a small pinhole aperture imaged onto the sample, which enables the rejection of the light scattered from out of the focus of the objective [138-140]. Compared to conventional microscopy, the use of point illumination on the sample and spatial filtering on the detector has the advantages of providing sharper images by increasing the effective axial resolution of the system (termed as confocal gate), as well as improving the contrast by increasing the signal to noise ratio (SNR) by rejecting scattered light from out of focal plane [141]. For the last several decades this imaging technology has been found applications in many areas of biological sciences and biomedicine, in form of a benchtop microscopic imaging system as well as an *in vivo* cellular resolution imaging platform [142-146].

Confocal laser endomicroscopy (CLE) is the integration of confocal imaging into the endoscopic setting. Currently there are two FDA approved CLE imaging platforms available to use in the U.S. The first system, iCLE (Pentax Endomicroscopy, Japan) is an integrated system that features both standard endoscopic imaging as well as the confocal imaging [147]. The second system is a probe based confocal imaging system, pCLE (Cellvizio Endomicroscopy, MKT,

France), where the imaging catheter is advanced through the working channel of a standard endoscope [148]. Several key features of these two systems are compared in Table 1.

	iCLE	pCLE	
		Low Res	High Res
Imaging Depth (um)	0-250	70-130	55-65
Field of View (um)	475 x 475	600	240
Lateral Res. (um)	0.7	3.5	1
Axial Res. (um)	7	15	5
Frame Rate (fps)	0.8	12	12
Number of pixels	1 megapixel	30,000 pixels	30,000 pixels

Table 1: Comparison of two commercially available confocal imaging systems.

As can be seen from Table 1, pCLE system has two probe options. The lower resolution probe provides larger field of view at a cost of lower resolution. The higher resolution probe, on the other hand, compares with the iCLE system in terms of resolution. One major difference between the pCLE and high resolution iCLE is that the focus of the former system can be adjusted from 0 um to 250 um, whereas the probe of the pCLE has a fixed focus around 60 um below the tissue contact. Moreover, the field of view of the iCLE is twice larger than pCLE, as well as it has significantly higher pixel density. On the other hand, pCLE has an increased frame rate compared to iCLE. Arguably the most significant advantage of pCLE is its compatibility with any endoscope with a working channel of at least 2.8 mm. In order to use iCLE, however, a complete endoscopic imaging platform needs to be purchased, which is a limiting factor for established endoscopy suites. Furthermore, the current iCLE product features a standard resolution WLE, whereas pCLE can be used with high resolution endoscopes as well. Due to these reasons, a majority of CLE studies especially in the U.S. employs a pCLE system for imaging.

For both of the CLE systems, extrinsic contrast is achieved by the intravenous administration of fluorescein. The leakage of fluorescein from the vessels provides the contrast in the images, where the capillaries and extracellular matrix appears bright and the cells and nuclei appears as dark structures. The topical agent Acriflavine has also been used, which provides nuclear contrast by staining the nuclei, however, it is not approved to *in vivo* use in the U.S. due to its mutagenic potential [149, 150]. Therefore, unless noted otherwise all the studies discussed next are used fluorescein as the contrast agent.

Miami classifications outline a consensus among endoscopists and confocal imaging experts for a classification system to distinguish normal and pathological states for a variety of GI diseases, including Barrett's Esophagus, biliary disease, colorectal disease, as well as gastric and duodenal diseases [151]. For colonic diseases, this classification scheme uses a combination

of structural changes in the crypt architecture, such as the formation of irregular and villiform structures, as well as changes in the size and organization of the vessels and capillaries to diagnose and classify neoplastic progression. As an example, normal colonic structure is defined as having round crypt structures, dark goblet cells and narrow vessels surrounding crypts in the CLE images, whereas disorganized/loss of villiform structures, presence of dark, irregularly thickened epithelium and dilated vessels are hallmark characteristics of adenocarcinoma.

As opposed to NBI and chromoendoscopy, the limited field of view of CLE renders this imaging modality impractical for the detection of colonic lesions during surveillance. However, it can still provide benefit to improve diagnostic accuracy and provide the acquisition of targeted biopsies when it is used in conjunction with a "red flag" imaging modality such as chromoendoscopy [152]. In a prospective, blinded study with 69 patients on 390 different imaging locations, iCLE has predicted neoplastic changes (intraepithelial neoplasia and colorectal cancer) in the lower GI tract with as high as 97.4% sensitivity and 99.4% specifity [153]. Another study compared the diagnostic accuracy of chromoendoscopy and CLE to detect malignancy in a total of 119 polyps from 75 patients [154]. Although there were no statistically significant differences in the specifity of the two imaging modalities, the sensitivity of CLE was 91%, whereas the sensitivity of WLE was found to be 77%. Another study compared CLE and chromoendoscopy for detecting residual neoplasia at the endoscopic mucosal resection (EMR) scars, and similar to the aforementioned study, CLE yielded better sensitivity and specifity compared to chromoendoscopy (97% sensitivity, 77% specificity vs. 72% sensitivity, 77% specificity for CLE vs. chromoendoscopy, respectively) [155]. Similar studies comparing CLE and NBI also showed improved diagnostic accuracy for CLE [156]. These studies demonstrate that the high resolution imaging capability of confocal imaging provides a high diagnostic accuracy once a suspected region can be identified with the aid of WLE, chromoendoscopy or NBI.

The use of chromoendoscopy and CLE in combination is proven to be effective in increasing the yield of neoplasia in IBD patients as well. In one prospective study where 73 patients randomized to the conventional colonoscopy group and 80 patients randomized to the CLE group, a 4.75 fold increase in the detection rate of intraepithelial neoplasia has been observed [157]. In the same study, CLE predicted the presence of neoplastic changes with 95% sensitivity and 98% specifity. In another study which investigated the utility of CLE in differentiating between DALM and ALM showed an accuracy of as high as 97%, with the kappa coefficient for the agreement between histology and CLE being 0.91 [158]. Several other feasibility studies have been further demonstrated the utility of CLE in detecting the neoplastic changes and differentiating between benign and malignant lesions in IBD patients [159, 160].

In summary, studies utilizing CLE have been shown the benefit of this imaging technology which offers *in vivo* assessment of pathological state of tissues with cellular resolution.

However, since the field of view of CLE is limited, as well as it often requires contact with the tissue, it is found to be unfeasible to use this modality by itself for the detection of colorectal malignancies. Hence an accompanying imaging modality such as NBI or chromoendoscopy is necessary to be used in conjunction with CLE in order to increase the overall yield of detection and reducing the sampling errors due to random biopsies. Another limitation of CLE is the lack of nuclear contrast due to the use of fluorescein, which makes it challenging to detect and classify early neoplastic changes, such as differentiating between low grade dysplasia and high grade dysplasia. Moreover, the acquisition of single depth in pCLE, and limited total imaging depth of iCLE makes this modality suitable to image only the superficial structures, which occludes extraction of some critical diagnostic information such as detecting mucosal invasion or staging neoplasia. Finally, it should be noted that even for prospective studies, readings of confocal images were often done in a retrospective setting, by selecting exclusively high quality images among the images generated throughout the imaging session. However, the diagnostic accuracy of CLE for the studies that involved real time diagnosis of malignancy showed significantly less sensitivity and specifity compared to aforementioned studies, which was related to the poor quality of confocal images for the overall imaging session [161]. Therefore, although CLE is a promising imaging modality for lower GI applications, there are several challenges that need to be addressed in order for this technology to gain clinical acceptance.

iv. Optical Coherence Tomography

The utility of OCT for the *in vivo* detection and diagnosis of lower GI diseases has not been investigated thoroughly so far, although several feasibility studies have been conducted. Earlier studies have demonstrated the superiority of OCT compared to endoscopic ultrasound (EUS) in terms of spatial resolution [162]. Another study demonstrated a strong correlation of OCT images and histology, in terms of classifying the mucosal and submucosal layers of the lower GI tract, although this study was conducted with *ex vivo* specimens [163]. In one study OCT has been used to identify regions of active inflammation in UC patients based on alterations in the layered architecture of the colon [164]. Involving 27 patients, this study achieved a sensitivity of 100%, whereas the specifity was as low as 69%. Similarly, in another, *ex vivo* study using OCT as the imaging modality, a sensitivity of 86% and specifity of 91% has been achieved in differentiation between UC and CD for IBD patients [165]. The same study has been also conducted *in vivo* with the involvement of 40 CD and 30 UC patients, where a sensitivity and specifity of 90% and 83%, respectively, has been demonstrated [166]. Note that in both of these studies the main diagnostic feature for the OCT images was the presence or absence of the appearance of the layered architecture for the cross sectional colon images, as any apparent disruption on this structure is assumed to indicate transmural inflammation, which is considered as a hallmark of CD.

Note that most of these earlier studies on OCT for lower GI applications have been focused on inferring information from cross sectional images. However, as it has been seen throughout this section, *en face* visualization is critical in order to identify pit patterns, vascular changes, flat or depressed lesions, and other diagnostic features relevant to lower GI diseases. However, tied to the technological challenges in the development of OCT probes that can acquire a volumetric data from which an image can be reconstructed in an *en face* fashion, as well as limitations in achieving fast imaging speeds have been so far obstructed the use of OCT for many of the lower GI applications that require the identification of the aforementioned features.

On the other hand, in the recent years there have been many advances in both OCT technology and instrumentation. Recently, a study by our research group has demonstrated *in vivo* endoscopic OCT images from lower GI tract that clearly showed features of regular crypt architecture (Type – I pit pattern) [167]. This study employed a Fourier domain mode locked (FDML) laser with a tuning range of 180 nm, achieving an axial resolution of 6 um in tissues over a 180 mm^2 field with an imaging range of 1.6 mm. Furthermore, this study featured an OCT probe which performed spiral scanning of the imaging beam, actuated proximal to the endoscopists. However, due to the long length of the probe and anatomical constraints of the human colon, such as the presence of sharp bends, makes it challenging to transfer the rotation to the distal end uniformly. Hence, artifacts associated with this non-uniformity in the rotation and other mechanical factors, such as frictions during the pullback, limits the reproducibility of the spiral scan, degrading the quality of the *en face* images [168].

In the recent years several distally actuated probes have been developed to overcome the challenge of non-uniform rotation for proximally actuated OCT probes. Examples include micromotor, miroelectromechanical (MEMS) and piezoelectrical transducer (PZT) scanning technologies [169-173]. Especially, a forward scanning PZT probe has the potential to generate images resembling to confocal images with better contrast and signal to noise ratio (SNR), without the need of external contrast agents [174]. Hence, with the integration of these novel scanning technologies to the endoscopic OCT systems, it is expected that more studies will be conducted in assessing the utility of OCT for lower GI applications. It is the author's belief that in many of the clinical applications mentioned in this section, OCT can be used in conjunction with a red flag technique, such as NBI or chromoendoscopy, in order to increase the yield of detecting neoplastic changes and decreasing the errors due to random sampling, similar to the clinical role of CLE. Moreover, OCT should outperform CLE due to its unique advantages such as performing depth resolved imaging for upto 1-2 mm below the tissue surface, which will aid in grading of neoplastic changes and enable the detection of submucosal invasion, enhanced contrast due to the additional coherence gate to the inherent confocal gate, increasing the field of view, ability to work non-contact to the tissue and eliminating the need of external contrast

agents. Furthermore, incorporating Doppler OCT methods, it will be possible to extract information related to the blood flow and enhance the visualization of the vessels and capillaries, similar to the clinical utility of NBI that was previously discussed [175, 176].

References

[1] G. J. Tearney, M. E. Brezinski, B. E. Bouma, S. A. Boppart, C. Pitris, J. F. Southern, and J. G. Fujimoto, "In vivo endoscopic optical biopsy with optical coherence tomography," *Science,* vol. 276, pp. 2037-9, Jun 27 1997.

[2] B. E. Bouma, G. J. Tearney, C. C. Compton, and N. S. Nishioka, "High-resolution imaging of the human esophagus and stomach in vivo using optical coherence tomography," *Gastrointestinal endoscopy,* vol. 51, pp. 467-474, 2000.

[3] X. D. Li, S. A. Boppart, J. Van Dam, H. Mashimo, M. Mutinga, W. Drexler, M. Klein, C. Pitris, M. L. Krinsky, M. E. Brezinski, and J. G. Fujimoto, "Optical coherence tomography: Advanced technology for the endoscopic imaging of Barrett's esophagus," *Endoscopy,* vol. 32, pp. 921-930, Dec 2000.

[4] M. V. Sivak, K. Kobayashi, J. A. Izatt, A. M. Rollins, R. Ung-Runyawee, A. Chak, R. C. K. Wong, G. A. Isenberg, and J. Willis, "High-resolution endoscopic imaging of the GI tract using optical coherence tomography," *Gastrointestinal endoscopy,* vol. 51, pp. 474-479, 2000.

[5] J. M. Poneros, S. Brand, B. E. Bouma, G. J. Tearney, C. C. Compton, and N. S. Nishioka, "Diagnosis of specialized intestinal metaplasia by optical coherence tomography," *Gastroenterology,* vol. 120, pp. 7-12, 2001.

[6] J. A. Evans, B. E. Bouma, J. Bressner, M. Shishkov, G. Y. Lauwers, M. Mino-Kenudson, N. S. Nishioka, and G. J. Tearney, "Identifying intestinal metaplasia at the squamocolumnar junction by using optical coherence tomography," *Gastrointestinal endoscopy,* vol. 65, pp. 50-56, 2007.

[7] G. Isenberg, M. Sivak Jr, A. Chak, R. Wong, J. E. Willis, B. Wolf, D. Y. Rowland, A. Das, and A. Rollins, "Accuracy of endoscopic optical coherence tomography in the detection of dysplasia in Barrett's esophagus: a prospective, double-blinded study," *Gastrointestinal endoscopy,* vol. 62, p. 825, 2005.

[8] X. Qi, M. V. Sivak, G. Isenberg, J. E. Willis, and A. M. Rollins, "Computer-aided diagnosis of dysplasia in Barrett's esophagus using endoscopic optical coherence tomography," *Journal of Biomedical Optics,* vol. 11, p. 044010, Jul-Aug 2006.

[9] D. C. Adler, Y. Chen, R. Huber, J. Schmitt, J. Connolly, and J. G. Fujimoto, "Three-dimensional endomicroscopy using optical coherence tomography," *Nature Photonics,* vol. 1, pp. 709-716, 2007.

[10] V. X. D. Yang, S. Tang, M. L. Gordon, B. Qi, G. Gardiner, M. Cirocco, P. Kortan, G. B. Haber, G. Kandel, and I. A. Vitkin, "Endoscopic Doppler optical coherence tomography in the human GI tract: initial experience," *Gastrointestinal endoscopy,* vol. 61, pp. 879-890, 2005.

[11] B. J. Vakoc, M. Shishko, S. H. Yun, W. Y. Oh, M. J. Suter, A. E. Desjardins, J. A. Evans, N. S. Nishioka, G. J. Tearney, and B. E. Bouma, "Comprehensive esophageal microscopy by using optical frequency–domain imaging (with video)," *Gastrointestinal endoscopy,* vol. 65, pp. 898-905, 2007.

[12] M. J. Suter, B. J. Vakoc, P. S. Yachimski, M. Shishkov, G. Y. Lauwers, M. Mino-Kenudson, B. E. Bouma, N. S. Nishioka, and G. J. Tearney, "Comprehensive microscopy of the esophagus in human patients with optical frequency domain imaging," *Gastrointest Endosc,* vol. 68, pp. 745-53, Oct 2008.

[13] C. Zhou, T. H. Tsai, H. C. Lee, T. Kirtane, M. Figueiredo, Y. K. Tao, O. O. Ahsen, D. C. Adler, J. M. Schmitt, Q. Huang, J. G. Fujimoto, and H. Mashimo, "Characterization of buried glands before and after radiofrequency ablation by using 3-dimensional optical coherence tomography (with videos)," *Gastrointest Endosc,* vol. 76, pp. 32-40, Jul 2012.

[14] T. H. Tsai, C. Zhou, Y. K. Tao, H. C. Lee, O. O. Ahsen, M. Figueiredo, T. Kirtane, D. C. Adler, J. M. Schmitt, Q. Huang, J. G. Fujimoto, and H. Mashimo, "Structural markers observed with

endoscopic 3-dimensional optical coherence tomography correlating with Barrett's esophagus radiofrequency ablation treatment response (with videos)," *Gastrointest Endosc,* Jul 24 2012.

[15] American Cancer Society., "Cancer facts & figures," ed. Atlanta, GA: The Society, p. v.

[16] R. Siegel, D. Naishadham, and A. Jemal, "Cancer statistics, 2012," *CA Cancer J Clin,* vol. 62, pp. 10-29, Jan-Feb 2012.

[17] B. Vogelstein, E. R. Fearon, S. R. Hamilton, S. E. Kern, A. C. Preisinger, M. Leppert, Y. Nakamura, R. White, A. M. Smits, and J. L. Bos, "Genetic alterations during colorectal-tumor development," *N Engl J Med,* vol. 319, pp. 525-32, Sep 1 1988.

[18] R. J. Schlemper, R. H. Riddell, Y. Kato, F. Borchard, H. S. Cooper, S. M. Dawsey, M. F. Dixon, C. M. Fenoglio-Preiser, J. F. Flejou, K. Geboes, T. Hattori, T. Hirota, M. Itabashi, M. Iwafuchi, A. Iwashita, Y. I. Kim, T. Kirchner, M. Klimpfinger, M. Koike, G. Y. Lauwers, K. J. Lewin, G. Oberhuber, F. Offner, A. B. Price, C. A. Rubio, M. Shimizu, T. Shimoda, P. Sipponen, E. Solcia, M. Stolte, H. Watanabe, and H. Yamabe, "The Vienna classification of gastrointestinal epithelial neoplasia," *Gut,* vol. 47, pp. 251-5, Aug 2000.

[19] A. G. Zauber, S. J. Winawer, M. J. O'Brien, I. Lansdorp-Vogelaar, M. van Ballegooijen, B. F. Hankey, W. Shi, J. H. Bond, M. Schapiro, J. F. Panish, E. T. Stewart, and J. D. Waye, "Colonoscopic polypectomy and long-term prevention of colorectal-cancer deaths," *N Engl J Med,* vol. 366, pp. 687-96, Feb 23 2012.

[20] C. J. Kahi, T. F. Imperiale, B. E. Juliar, and D. K. Rex, "Effect of screening colonoscopy on colorectal cancer incidence and mortality," *Clin Gastroenterol Hepatol,* vol. 7, pp. 770-5; quiz 711, Jul 2009.

[21] D. F. Ransohoff, "How Much Does Colonoscopy Reduce Colon Cancer Mortality?," *Annals of Internal Medicine,* vol. 150, pp. 50-52, Jan 6 2009.

[22] H. Singh, Z. Nugent, A. A. Demers, E. V. Kliewer, S. M. Mahmud, and C. N. Bernstein, "The reduction in colorectal cancer mortality after colonoscopy varies by site of the cancer," *Gastroenterology,* vol. 139, pp. 1128-37, Oct 2010.

[23] H. Brenner, J. Chang-Claude, C. M. Seiler, A. Rickert, and M. Hoffmeister, "Protection from colorectal cancer after colonoscopy: a population-based, case-control study," *Ann Intern Med,* vol. 154, pp. 22-30, Jan 4 2011.

[24] S. Kudo, H. Kashida, and T. Tamura, "Early colorectal cancer: flat or depressed type," *Journal of Gastroenterology and Hepatology,* vol. 15 Suppl, pp. D66-70, 2000.

[25] R. Soetikno, S. Friedland, T. Kaltenbach, K. Chayama, and S. Tanaka, "Nonpolypoid (flat and depressed) colorectal neoplasms," *Gastroenterology,* vol. 130, pp. 566-76; quiz 588-9, Feb 2006.

[26] T. Sawada, K. Hojo, and Y. Moriya, "Colonoscopic management of focal and early colorectal carcinoma," *Baillieres Clin Gastroenterol,* vol. 3, pp. 627-45, Jul 1989.

[27] M. E. Zalis, M. A. Barish, J. R. Choi, A. H. Dachman, H. M. Fenlon, J. T. Ferrucci, S. N. Glick, A. Laghi, M. Macari, E. G. McFarland, M. M. Morrin, P. J. Pickhardt, J. Soto, and J. Yee, "CT colonography reporting and data system: a consensus proposal," *Radiology,* vol. 236, pp. 3-9, Jul 2005.

[28] R. A. Wolber and D. A. Owen, "Flat adenomas of the colon," *Hum Pathol,* vol. 22, pp. 70-4, Jan 1991.

[29] E. Jaramillo, M. Watanabe, P. Slezak, and C. Rubio, "Flat neoplastic lesions of the colon and rectum detected by high-resolution video endoscopy and chromoscopy," *Gastrointest Endosc,* vol. 42, pp. 114-22, Aug 1995.

[30] T. Fujii, B. J. Rembacken, M. F. Dixon, S. Yoshida, and A. T. Axon, "Flat adenomas in the United Kingdom: are treatable cancers being missed?," *Endoscopy,* vol. 30, pp. 437-43, Jun 1998.

[31] B. J. Rembacken, T. Fujii, A. Cairns, M. F. Dixon, S. Yoshida, D. M. Chalmers, and A. T. Axon, "Flat and depressed colonic neoplasms: a prospective study of 1000 colonoscopies in the UK," *Lancet,* vol. 355, pp. 1211-4, Apr 8 2000.

[32] Y. Saitoh, I. Waxman, A. B. West, N. K. Popnikolov, Z. Gatalica, J. Watari, T. Obara, Y. Kohgo, and P. J. Pasricha, "Prevalence and distinctive biologic features of flat colorectal adenomas in a North American population," *Gastroenterology,* vol. 120, pp. 1657-65, Jun 2001.

[33] "The Paris endoscopic classification of superficial neoplastic lesions: esophagus, stomach, and colon: November 30 to December 1, 2002," *Gastrointest Endosc,* vol. 58, pp. S3-43, Dec 2003.

[34] R. M. Soetikno, T. Kaltenbach, R. V. Rouse, W. Park, A. Maheshwari, T. Sato, S. Matsui, and S. Friedland, "Prevalence of nonpolypoid (flat and depressed) colorectal neoplasms in asymptomatic and symptomatic adults," *JAMA,* vol. 299, pp. 1027-35, Mar 5 2008.

[35] S. Kudo, H. Kashida, T. Tamura, E. Kogure, Y. Imai, H. Yamano, and A. R. Hart, "Colonoscopic diagnosis and management of nonpolypoid early colorectal cancer," *World Journal of Surgery,* vol. 24, pp. 1081-90, Sep 2000.

[36] D. P. Hurlstone, S. S. Cross, I. Adam, A. J. Shorthouse, S. Brown, D. S. Sanders, and A. J. Lobo, "A prospective clinicopathological and endoscopic evaluation of flat and depressed colorectal lesions in the United Kingdom," *Am J Gastroenterol,* vol. 98, pp. 2543-9, Nov 2003.

[37] S. Bensen, L. A. Mott, B. Dain, R. Rothstein, and J. Baron, "The colonoscopic miss rate and true one-year recurrence of colorectal neoplastic polyps. Polyp Prevention Study Group," *Am J Gastroenterol,* vol. 94, pp. 194-9, Jan 1999.

[38] J. H. Haseman, G. T. Lemmel, E. Y. Rahmani, and D. K. Rex, "Failure of colonoscopy to detect colorectal cancer: evaluation of 47 cases in 20 hospitals," *Gastrointest Endosc,* vol. 45, pp. 451-5, Jun 1997.

[39] D. J. Robertson, E. R. Greenberg, M. Beach, R. S. Sandler, D. Ahnen, R. W. Haile, C. A. Burke, D. C. Snover, R. S. Bresalier, G. McKeown-Eyssen, J. S. Mandel, J. H. Bond, R. U. Van Stolk, R. W. Summers, R. Rothstein, T. R. Church, B. F. Cole, T. Byers, L. Mott, and J. A. Baron, "Colorectal cancer in patients under close colonoscopic surveillance," *Gastroenterology,* vol. 129, pp. 34-41, Jul 2005.

[40] L. J. Hixson, M. B. Fennerty, R. E. Sampliner, D. McGee, and H. Garewal, "Prospective study of the frequency and size distribution of polyps missed by colonoscopy," *J Natl Cancer Inst,* vol. 82, pp. 1769-72, Nov 21 1990.

[41] D. K. Rex, C. S. Cutler, G. T. Lemmel, E. Y. Rahmani, D. W. Clark, D. J. Helper, G. A. Lehman, and D. G. Mark, "Colonoscopic miss rates of adenomas determined by back-to-back colonoscopies," *Gastroenterology,* vol. 112, pp. 24-8, Jan 1997.

[42] C. Abraham and J. H. Cho, "Inflammatory bowel disease," *N Engl J Med,* vol. 361, pp. 2066-78, Nov 19 2009.

[43] D. K. Podolsky, "Inflammatory bowel disease," *N Engl J Med,* vol. 347, pp. 417-29, Aug 8 2002.

[44] M. D. Kappelman, S. L. Rifas-Shiman, C. Q. Porter, D. A. Ollendorf, R. S. Sandler, J. A. Galanko, and J. A. Finkelstein, "Direct health care costs of Crohn's disease and ulcerative colitis in US children and adults," *Gastroenterology,* vol. 135, pp. 1907-13, Dec 2008.

[45] C. Prantera and M. L. Scribano, "Antibiotics and probiotics in inflammatory bowel disease: why, when, and how," *Curr Opin Gastroenterol,* vol. 25, pp. 329-33, Jul 2009.

[46] G. R. Lichtenstein, S. B. Hanauer, and W. J. Sandborn, "Management of Crohn's disease in adults," *Am J Gastroenterol,* vol. 104, pp. 465-83; quiz 464, 484, Feb 2009.

[47] G. R. Lichtenstein, S. K. Yan, M. Bala, and S. Hanauer, "Remission in patients with Crohn's disease is associated with improvement in employment and quality of life and a decrease in hospitalizations and surgeries," *American Journal of Gastroenterology,* vol. 99, pp. 91-96, Jan 2004.

[48] R. Odze, "Diagnostic problems and advances in inflammatory bowel disease," *Mod Pathol,* vol. 16, pp. 347-58, Apr 2003.

[49] S. L. Robbins, V. Kumar, and R. S. Cotran, *Robbins and Cotran pathologic basis of disease*, 8th ed. Philadelphia, PA: Saunders/Elsevier, 2010.

[50] B. E. Sands, "From symptom to diagnosis: Clinical distinctions among various forms of intestinal inflammation," *Gastroenterology,* vol. 126, pp. 1518-1532, May 2004.

[51] G. Meucci, A. Bortoli, F. A. Riccioli, C. M. Girelli, F. Radaelli, R. Rivolta, and M. Tatarella, "Frequency and clinical evolution of indeterminate colitis: a retrospective multi-centre study in northern Italy. GSMII (Gruppo di Studio per le Malattie Infiammatorie Intestinali)," *Eur J Gastroenterol Hepatol,* vol. 11, pp. 909-13, Aug 1999.

[52] A. B. Price, "Overlap in the spectrum of non-specific inflammatory bowel disease--'colitis indeterminate'," *Journal of clinical pathology,* vol. 31, pp. 567-77, Jun 1978.

[53] N. C. Swan, J. G. Geoghegan, D. P. O'Donoghue, J. M. Hyland, and K. Sheahan, "Fulminant colitis in inflammatory bowel disease: detailed pathologic and clinical analysis," *Dis Colon Rectum,* vol. 41, pp. 1511-5, Dec 1998.

[54] A. E. M'Koma, E. H. Seeley, P. E. Wise, M. K. Washington, D. A. Schwartz, A. J. Herline, R. L. Muldoon, and R. M. Caprioli, "Proteomic Analysis of Colonic Submucosa Differentiates Crohn's and Ulcerative Colitis," *Gastroenterology,* vol. 136, pp. A349-A349, May 2009.

[55] P. Von Stein, R. Lofberg, N. V. Kuznetsov, A. W. Gielen, J. O. Persson, R. Sundberg, K. Hellstrom, A. Eriksson, R. Befrits, A. Ost, and O. D. Von Stein, "Multigene analysis can discriminate between ulcerative colitis, Crohn's disease, and irritable bowel syndrome," *Gastroenterology,* vol. 134, pp. 1869-1881, Jun 2008.

[56] G. E. Reese, V. A. Constantinides, C. Simillis, A. W. Darzi, T. R. Orchard, V. W. Fazio, and P. P. Tekkis, "Diagnostic precision of anti-Saccharomyces cerevisiae antibodies and perinuclear antineutrophil cytoplasmic antibodies in inflammatory bowel disease," *Am J Gastroenterol,* vol. 101, pp. 2410-22, Oct 2006.

[57] A. B. Jensen, M. Larsen, M. Gislum, M. V. Skriver, P. Jepsen, B. Norgaard, and H. T. Sorensen, "Survival after colorectal cancer in patients with ulcerative colitis: a nationwide population-based Danish study," *Am J Gastroenterol,* vol. 101, pp. 1283-7, Jun 2006.

[58] M. Larsen, H. Mose, M. Gislum, M. V. Skriver, P. Jepsen, B. Norgard, and H. T. Sorensen, "Survival after colorectal cancer in patients with Crohn's disease: A nationwide population-based Danish follow-up study," *Am J Gastroenterol,* vol. 102, pp. 163-7, Jan 2007.

[59] T. Jess, C. Rungoe, and L. Peyrin-Biroulet, "Risk of colorectal cancer in patients with ulcerative colitis: a meta-analysis of population-based cohort studies," *Clin Gastroenterol Hepatol,* vol. 10, pp. 639-45, Jun 2012.

[60] M. D. Rutter, B. P. Saunders, K. H. Wilkinson, S. Rumbles, G. Schofield, M. A. Kamm, C. B. Williams, A. B. Price, I. C. Talbot, and A. Forbes, "Thirty-year analysis of a colonoscopic surveillance program for neoplasia in ulcerative colitis," *Gastroenterology,* vol. 130, pp. 1030-8, Apr 2006.

[61] C. N. Bernstein, J. F. Blanchard, E. Kliewer, and A. Wajda, "Cancer risk in patients with inflammatory bowel disease: a population-based study," *Cancer,* vol. 91, pp. 854-62, Feb 15 2001.

[62] C. Canavan, K. R. Abrams, and J. Mayberry, "Meta-analysis: colorectal and small bowel cancer risk in patients with Crohn's disease," *Aliment Pharmacol Ther,* vol. 23, pp. 1097-104, Apr 15 2006.

[63] C. A. Rubio, R. Befrits, T. Ljung, E. Jaramillo, and P. Slezak, "Colorectal carcinoma in Ulcerative Colitis is decreasing in Scandinavian countries," *Anticancer Research,* vol. 21, pp. 2921-2924, Jul-Aug 2001.

[64] T. Jess, E. V. Loftus, F. S. Velayos, W. S. Harmsen, A. R. Zinsmeister, T. C. Smyrk, C. D. Schleck, W. J. Tremaine, L. J. Melton, P. Munkholm, and W. J. Sandborn, "Risk of intestinal cancer in inflammatory bowel disease: A population-based study from Olmsted County, Minnesota," *Gastroenterology,* vol. 130, pp. 1039-1046, Apr 2006.

[65] E. V. Loftus, Jr., "Epidemiology and risk factors for colorectal dysplasia and cancer in ulcerative colitis," *Gastroenterol Clin North Am,* vol. 35, pp. 517-31, Sep 2006.

[66] K. W. Nuako, D. A. Ahlquist, D. W. Mahoney, D. J. Schaid, D. M. Siems, and N. M. Lindor, "Familial predisposition for colorectal cancer in chronic ulcerative colitis: a case-control study," *Gastroenterology,* vol. 115, pp. 1079-83, Nov 1998.

[67] J. A. Eaden, K. R. Abrams, and J. F. Mayberry, "The risk of colorectal cancer in ulcerative colitis: a meta-analysis," *Gut,* vol. 48, pp. 526-35, Apr 2001.

[68] R. M. Soetikno, O. S. Lin, P. A. Heidenreich, H. S. Young, and M. O. Blackstone, "Increased risk of colorectal neoplasia in patients with primary sclerosing cholangitis and ulcerative colitis: a meta-analysis," *Gastrointest Endosc,* vol. 56, pp. 48-54, Jul 2002.

[69] S. Soderlund, F. Granath, O. Brostrom, P. Karlen, R. Lofberg, A. Ekbom, and J. Askling, "Inflammatory bowel disease confers a lower risk of colorectal cancer to females than to males," *Gastroenterology,* vol. 138, pp. 1697-703, May 2010.

[70] F. A. Farraye, R. D. Odze, J. Eaden, and S. H. Itzkowitz, "AGA technical review on the diagnosis and management of colorectal neoplasia in inflammatory bowel disease," *Gastroenterology,* vol. 138, pp. 746-74, 774 e1-4; quiz e12-3, Feb 2010.

[71] C. N. Bernstein, F. Shanahan, and W. M. Weinstein, "Are we telling patients the truth about surveillance colonoscopy in ulcerative colitis?," *Lancet,* vol. 343, pp. 71-4, 1994.

[72] S. R. Gorfine, J. J. Bauer, M. T. Harris, and I. Kreel, "Dysplasia complicating chronic ulcerative colitis: is immediate colectomy warranted?," *Dis Colon Rectum,* vol. 43, pp. 1575-81, Nov 2000.

[73] H. Neumann, M. Vieth, C. Langner, M. F. Neurath, and J. Mudter, "Cancer risk in IBD: How to diagnose and how to manage DALM and ALM," *World Journal of Gastroenterology,* vol. 17, pp. 3184-3191, Jul 21 2011.

[74] A. Kakkar and F. A. Farraye, "Diagnosis and Management of Colorectal Neoplasia in Patients with Inflammatory Bowel Disease," *Crohn's Disease and Ulcerative Colitis: From Epidemiology and Immunobiology to a Rational Diagnostic and Therapeutic Approach,* pp. 701-711, 2012.

[75] M. Engelsgjerd, F. A. Farraye, and R. D. Odze, "Polypectomy may be adequate treatment for adenoma-like dysplastic lesions in chronic ulcerative colitis," *Gastroenterology,* vol. 117, pp. 1288-1294, Dec 1999.

[76] R. D. Odze, F. A. Farraye, J. L. Hecht, and J. L. Hornick, "Long-term Follow-up After Polypectomy Treatment for Adenoma-Like Dysplastic Lesions in Ulcerative Colitis," *Clinical Gastroenterology and Hepatology,* vol. 2, pp. 534-541, Jul 2004.

[77] K. Monkemuller, H. Neumann, P. Malfertheiner, and L. C. Fry, "Advanced Colon Polypectomy," *Clinical Gastroenterology and Hepatology,* vol. 7, pp. 641-652, Jun 2009.

[78] W. Blonski, R. Kundu, E. F. Furth, J. Lewis, F. Aberra, and G. R. Lichtenstein, "High-grade dysplastic adenoma-like mass lesions are not an indication for colectomy in patients with ulcerative colitis," *Scandinavian Journal of Gastroenterology,* vol. 43, pp. 817-820, 2008.

[79] W. R. Connell, J. E. Lennard-Jones, C. B. Williams, I. C. Talbot, A. B. Price, and K. H. Wilkinson, "Factors affecting the outcome of endoscopic surveillance for cancer in ulcerative colitis," *Gastroenterology,* vol. 107, pp. 934-44, Oct 1994.

[80] C. Torres, D. Antonioli, and R. D. Odze, "Polypoid dysplasia and adenomas in inflammatory bowel disease: a clinical, pathologic, and follow-up study of 89 polyps from 59 patients," *American Journal of Surgical Pathology,* vol. 22, pp. 275-84, Mar 1998.

[81] F. A. Farraye, J. D. Waye, M. Moscandrew, T. C. Heeren, and R. D. Odze, "Variability in the diagnosis and management of adenoma-like and non-adenoma-like dysplasia-associated lesions or masses in inflammatory bowel disease: an Internet-based study," *Gastrointest Endosc,* vol. 66, pp. 519-29, Sep 2007.

[82] N. Harpaz and A. D. Polydorides, "Colorectal dysplasia in chronic inflammatory bowel disease: pathology, clinical implications, and pathogenesis," *Arch Pathol Lab Med,* vol. 134, pp. 876-95, Jun 2010.

[83] S. S. Poulsen, K. C. Christensen, M. Petri, and S. Jarnum, "Stereomicroscopic examination of stained rectal biopsies," *Scand J Gastroenterol,* vol. 13, pp. 605-8, 1978.

[84] Q. Huang, N. Fukami, H. Kashida, T. Takeuchi, E. Kogure, T. Kurahashi, E. Stahl, Y. Kudo, H. Kimata, and S. E. Kudo, "Interobserver and intra-observer consistency in the endoscopic assessment of colonic pit patterns," *Gastrointest Endosc,* vol. 60, pp. 520-6, Oct 2004.

[85] S. Kudo, "Early colorectal cancer: detection of depressed types of colorectal carcinoma," *Tokyo: Igaku-Shoin,* vol. 166, 1996.

[86] S. E. Kudo, S. Tamura, T. Nakajima, H. O. Yamano, H. Kusaka, and H. Watanabe, "Diagnosis of colorectal tumorous lesions by magnifying endoscopy," *Gastrointestinal Endoscopy,* vol. 44, pp. 8-14, Jul 1996.

[87] S. Kudo, C. A. Rubio, C. R. Teixeira, H. Kashida, and E. Kogure, "Pit pattern in colorectal neoplasia: endoscopic magnifying view," *Endoscopy,* vol. 33, pp. 367-73, Apr 2001.

[88] H. Kashida and S. E. Kudo, "Magnifying colonoscopy, early colorectal cancer, and flat adenomas," *Colonoscopy: Principles and Practice,* pp. 478-486, 2007.

[89] S. Kudo, S. Tamura, T. Nakajima, H. Yamano, H. Kusaka, and H. Watanabe, "Diagnosis of colorectal tumorous lesions by magnifying endoscopy," *Gastrointest Endosc,* vol. 44, pp. 8-14, Jul 1996.

[90] R. Kiesslich, M. Von Bergh, M. Hahn, G. Hermann, and M. Jung, "Chromoendoscopy with indigocarmine improves the detection of adenomatous and nonadenomatous lesions in the colon," *Endoscopy,* vol. 33, p. 1001, 2001.

[91] S. Y. Tung, C. S. Wu, and M. Y. Su, "Magnifying colonoscopy in differentiating neoplastic from nonneoplastic colorectal lesions," *Am J Gastroenterol,* vol. 96, pp. 2628-32, Sep 2001.

[92] R. Singh, S. C. Mei, and S. Sethi, "Advanced endoscopic imaging in Barrett's oesophagus: a review on current practice," *World J Gastroenterol,* vol. 17, pp. 4271-6, Oct 14 2011.

[93] A. Ignjatovic, J. East, T. Guenther, J. Hoare, J. Morris, K. Ragunath, A. Shonde, J. Simmons, N. Suzuki, and S. Thomas-Gibson, "What is the most reliable imaging modality for small colonic polyp characterization? Study of white-light, autofluorescence, and narrow-band imaging," *Endoscopy,* vol. 43, p. 94, 2011.

[94] S. C. Ng and J. Y. Lau, "Narrow-band imaging in the colon: limitations and potentials," *J Gastroenterol Hepatol,* vol. 26, pp. 1589-96, Nov 2011.

[95] D. K. Rex and C. C. Helbig, "High yields of small and flat adenomas with high-definition colonoscopes using either white light or narrow band imaging," *Gastroenterology,* vol. 133, pp. 42-7, Jul 2007.

[96] A. Adler, H. Pohl, I. S. Papanikolaou, H. Abou-Rebyeh, G. Schachschal, W. Veltzke-Schlieker, A. C. Khalifa, E. Setka, M. Koch, B. Wiedenmann, and T. Rosch, "A prospective randomised study on narrow-band imaging versus conventional colonoscopy for adenoma detection: does narrow-band imaging induce a learning effect?," *Gut,* vol. 57, pp. 59-64, Jan 2008.

[97] A. Adler, J. Aschenbeck, T. Yenerim, M. Mayr, A. Aminalai, R. Drossel, A. Schroder, M. Scheel, B. Wiedenmann, and T. Rosch, "Narrow-band versus white-light high definition television endoscopic imaging for screening colonoscopy: a prospective randomized trial," *Gastroenterology,* vol. 136, pp. 410-6 e1; quiz 715, Feb 2009.

[98] J. E. East, N. Suzuki, and B. P. Saunders, "Comparison of magnified pit pattern interpretation with narrow band imaging versus chromoendoscopy for diminutive colonic polyps: a pilot study," *Gastrointest Endosc,* vol. 66, pp. 310-6, Aug 2007.

[99] T. Kaltenbach, S. Friedland, and R. Soetikno, "A randomised tandem colonoscopy trial of narrow band imaging versus white light examination to compare neoplasia miss rates," *Gut,* vol. 57, pp. 1406-12, Oct 2008.

[100] F. J. van den Broek, J. B. Reitsma, W. L. Curvers, P. Fockens, and E. Dekker, "Systematic review of narrow-band imaging for the detection and differentiation of neoplastic and nonneoplastic lesions in the colon (with videos)," *Gastrointest Endosc,* vol. 69, pp. 124-35, Jan 2009.

[101] H. M. Chiu, C. Y. Chang, C. C. Chen, Y. C. Lee, M. S. Wu, J. T. Lin, C. T. Shun, and H. P. Wang, "A prospective comparative study of narrow-band imaging, chromoendoscopy, and conventional colonoscopy in the diagnosis of colorectal neoplasia," *Gut,* vol. 56, pp. 373-9, Mar 2007.

[102] M. Y. Su, C. M. Hsu, Y. P. Ho, P. C. Chen, C. J. Lin, and C. T. Chiu, "Comparative study of conventional colonoscopy, chromoendoscopy, and narrow-band imaging systems in differential diagnosis of neoplastic and nonneoplastic colonic polyps," *Am J Gastroenterol,* vol. 101, pp. 2711-6, Dec 2006.

[103] H. Machida, Y. Sano, Y. Hamamoto, M. Muto, T. Kozu, H. Tajiri, and S. Yoshida, "Narrow-band imaging in the diagnosis of colorectal mucosal lesions: a pilot study," *Endoscopy,* vol. 36, pp. 1094-8, Dec 2004.

[104] M. Hirata, S. Tanaka, S. Oka, I. Kaneko, S. Yoshida, M. Yoshihara, and K. Chayama, "Magnifying endoscopy with narrow band imaging for diagnosis of colorectal tumors," *Gastrointest Endosc,* vol. 65, pp. 988-95, Jun 2007.

[105] E. Dekker, F. J. van den Broek, J. B. Reitsma, J. C. Hardwick, G. J. Offerhaus, S. J. van Deventer, D. W. Hommes, and P. Fockens, "Narrow-band imaging compared with conventional colonoscopy for the detection of dysplasia in patients with longstanding ulcerative colitis," *Endoscopy,* vol. 39, pp. 216-21, Mar 2007.

[106] J. E. East, N. Suzuki, A. von Herbay, and B. P. Saunders, "Narrow band imaging with magnification for dysplasia detection and pit pattern assessment in ulcerative colitis surveillance: a case with multiple dysplasia associated lesions or masses," *Gut,* vol. 55, pp. 1432-5, Oct 2006.

[107] M. B. Fennerty, "Tissue staining," *Gastrointest Endosc Clin N Am,* vol. 4, pp. 297-311, Apr 1994.

[108] J. C. Brooker, B. P. Saunders, S. G. Shah, C. J. Thapar, H. J. Thomas, W. S. Atkin, C. R. Cardwell, and C. B. Williams, "Total colonic dye-spray increases the detection of diminutive adenomas during routine colonoscopy: a randomized controlled trial," *Gastrointest Endosc,* vol. 56, pp. 333-8, Sep 2002.

[109] H. Shehab, "Chromoendoscopy in gastroenterology," *Arab Journal of Gastroenterology,* vol. 11, pp. 3-17, 2010.

[110] V. Meyer, P. Burtin, B. Bour, A. Blanchi, P. Cales, F. Oberti, B. Person, A. Croue, S. Dohn, R. Benoit, B. Fabiani, and J. Boyer, "Endoscopic detection of early esophageal cancer in a high-risk population: does Lugol staining improve videoendoscopy?," *Gastrointestinal endoscopy,* vol. 45, pp. 480-4, 1997.

[111] S. M. Dawsey, D. E. Fleischer, G. Q. Wang, B. Zhou, J. A. Kidwell, N. Lu, K. J. Lewin, M. J. Roth, T. L. Tio, and P. R. Taylor, "Mucosal iodine staining improves endoscopic visualization of squamous dysplasia and squamous cell carcinoma of the esophagus in Linxian, China," *Cancer,* vol. 83, pp. 220-31, Jul 15 1998.

[112] M. I. Canto, S. Setrakian, R. E. Petras, E. Blades, A. Chak, and M. V. Sivak, Jr., "Methylene blue selectively stains intestinal metaplasia in Barrett's esophagus," *Gastrointestinal endoscopy,* vol. 44, pp. 1-7, 1996.

[113] M. I. Canto, S. Setrakian, J. E. Willis, A. Chak, R. E. Petras, and M. V. Sivak, "Methylene blue staining of dysplastic and nondysplastic Barrett's esophagus: an in vivo and ex vivo study," *Endoscopy,* vol. 33, pp. 391-400, 2001.

[114] R. Kiesslich, J. Fritsch, M. Holtmann, H. H. Koehler, M. Stolte, S. Kanzler, B. Nafe, M. Jung, P. R. Galle, and M. F. Neurath, "Methylene blue-aided chromoendoscopy for the detection of intraepithelial neoplasia and colon cancer in ulcerative colitis," *Gastroenterology,* vol. 124, pp. 880-8, 2003.

[115] K. Ida, Y. Hashimoto, S. Takeda, K. Murakami, and K. Kawai, "Endoscopic diagnosis of gastric cancer with dye scattering," *Am J Gastroenterol,* vol. 63, pp. 316-20, Apr 1975.

[116] T. Masaki, J. P. Sheffield, I. C. Talbot, and C. B. Williams, "Non-Polypoid Adenoma of the Large-Intestine," *International Journal of Colorectal Disease,* vol. 9, pp. 180-183, Nov 1994.

[117] S. Niveloni, A. Fiorini, R. Dezi, S. Pedreira, E. Smecuol, H. Vazquez, A. Cabanne, L. A. Boerr, J. Valero, Z. Kogan, E. Maurino, and J. C. Bai, "Usefulness of videoduodenoscopy and vital dye staining as indicators of mucosal atrophy of celiac disease: assessment of interobserver agreement," *Gastrointestinal Endoscopy,* vol. 47, pp. 223-229, Mar 1998.

[118] G. S. Kouklakis, J. Kountouras, S. M. Dokas, E. J. Molyvas, G. P. Vourvoulakis, and G. I. Minopoulos, "Methylene blue chromoendoscopy for the detection of Barrett's esophagus in a Greek cohort," *Endoscopy,* vol. 35, pp. 383-387, May 2003.

[119] L. M. Wong Kee Song, D. G. Adler, B. Chand, J. D. Conway, J. M. Croffie, J. A. Disario, D. S. Mishkin, R. J. Shah, L. Somogyi, W. M. Tierney, and B. T. Petersen, "Chromoendoscopy," *Gastrointest Endosc,* vol. 66, pp. 639-49, Oct 2007.

[120] K. Togashi, F. Konishi, T. Ishizuka, T. Sato, S. Senba, and K. Kanazawa, "Efficacy of magnifying endoscopy in the differential diagnosis of neoplastic and non-neoplastic polyps of the large bowel," *Dis Colon Rectum,* vol. 42, pp. 1602-8, Dec 1999.

[121] S. Kato, T. Fujii, I. Koba, Y. Sano, K. I. Fu, A. Parra-Blanco, H. Tajiri, S. Yoshida, and B. Rembacken, "Assessment of colorectal lesions using magnifying colonoscopy and mucosal dye spraying: can significant lesions be distinguished?," *Endoscopy,* vol. 33, pp. 306-10, 2001.

[122] H. H. Liu, S. E. Kudo, and J. P. Juch, "Pit pattern analysis by magnifying chromoendoscopy for the diagnosis of colorectal polyps," *J Formos Med Assoc,* vol. 102, pp. 178-82, Mar 2003.

[123] G. M. Eisen, C. Y. Kim, D. E. Fleischer, R. A. Kozarek, D. L. Carr-Locke, T. Li, C. J. Gostout, S. J. Heller, E. A. Montgomery, and F. H. Al-Kawas, "High-resolution chromoendoscopy for classifying colonic polyps: a multicenter study," *Gastrointestinal endoscopy,* vol. 55, p. 687, 2002.

[124] D. Hurlstone, S. Cross, I. Adam, A. Shorthouse, S. Brown, D. Sanders, and A. Lobo, "Endoscopic morphological anticipation of submucosal invasion in flat and depressed colorectal lesions: clinical implications and subtype analysis of the kudo type V pit pattern using high-magnification-chromoscopic colonoscopy," *Colorectal Disease,* vol. 6, pp. 369-375, 2004.

[125] M. Bianco, G. Rotondano, R. Marmo, M. Garofano, R. Piscopo, A. de Gregorio, L. Baron, L. Orsini, and L. Cipolletta, "Predictive value of magnification chromoendoscopy for diagnosing invasive neoplasia in nonpolypoid colorectal lesions and stratifying patients for endoscopic resection or surgery," *Endoscopy,* vol. 38, p. 470, 2006.

[126] Y. Liu, L. Huang, X. Wan, J. Cui, N. Xu, and C. Wu, "Fuji Intelligent Chromo Endoscopy and staining technique for the diagnosis of colon tumor," *Chinese Medical Journal (English Edition),* vol. 121, p. 977, 2008.

[127] Y. Kobayashi, Y. Hayashino, J. Jackson, N. Takagaki, S. Hinotsu, and K. Kawakami, "Diagnostic performance of chromoendoscopy and narrow band imaging for colonic neoplasms: a meta-analysis," *Colorectal Disease,* vol. 14, pp. 18-28, 2012.

[128] J. Pohl, A. Schneider, H. Vogell, G. Mayer, G. Kaiser, and C. Ell, "Pancolonic chromoendoscopy with indigo carmine versus standard colonoscopy for detection of neoplastic lesions: a randomised two-centre trial," *Gut,* vol. 60, pp. 485-90, Apr 2011.

[129] C. J. Kahi, J. C. Anderson, I. Waxman, W. R. Kessler, T. F. Imperiale, X. Li, and D. K. Rex, "High-definition chromocolonoscopy vs. high-definition white light colonoscopy for average-risk colorectal cancer screening," *Am J Gastroenterol,* vol. 105, pp. 1301-7, Jun 2010.

[130] T. Lecomte, C. Cellier, T. Meatchi, J. P. Barbier, P. H. Cugnenc, R. Jian, P. Laurent-Puig, and B. Landi, "Chromoendoscopic Colonoscopy for detecting preneoplastic lesions in hereditary nonpolyposis colorectal cancer syndrome," *Clinical Gastroenterology and Hepatology,* vol. 3, pp. 897-902, Sep 2005.

[131] E. M. Stoffel, K. Turgeon, D. H. Stockwell, D. P. Normolle, M. Tuck, N. E. Marcon, J. A. Baron, R. S. Bresalier, N. Arber, M. T. Ruffin, S. Syngal, D. E. Brenner, and Glne-Edrn, "Chromoendoscopy Detects More Adenomas than Colonoscopy Using Intensive Inspection without Dye Spraying," *Cancer Prevention Research,* vol. 1, pp. 507-513, Dec 2008.

[132] R. Huneburg, F. Lammert, C. Rabe, N. Rahner, P. Kahl, R. Buttner, P. Propping, T. Sauerbruch, and C. Lamberti, "Chromocolonoscopy detects more adenomas than white light colonoscopy or narrow band imaging colonoscopy in hereditary nonpolyposis colorectal cancer screening," *Endoscopy,* vol. 41, pp. 316-322, Apr 2009.

[133] T. Matsumoto, S. Nakamura, Y. Jo, T. Yao, and M. Iida, "Chromoscopy might improve diagnostic accuracy in cancer surveillance for ulcerative colitis," *American Journal of Gastroenterology,* vol. 98, pp. 1827-1833, Aug 2003.

[134] M. D. Rutter, B. P. Saunders, G. Schofield, A. Forbes, A. B. Price, and I. C. Talbot, "Pancolonic indigo carmine dye spraying for the detection of dysplasia in ulcerative colitis," *Gut,* vol. 53, pp. 256-60, Feb 2004.

[135] D. P. Hurlstone, M. E. McAlindon, D. S. Sanders, R. Keogh, A. J. Lobo, and S. S. Cross, "Further validation of high-magnification chromoscopic-colonoscopy for the detection of intraepithelial neoplasia and colon cancer in ulcerative colitis," *Gastroenterology,* vol. 126, pp. 376-377, Jan 2004.

[136] M. Sada, M. Igarashi, S. Yoshizawa, K. Kobayashi, T. Katsumata, K. Saigenji, Y. Otani, I. Okayasu, and H. Mitomi, "Dye spraying and magnifying endoscopy for dysplasia and cancer surveillance in ulcerative colitis," *Dis Colon Rectum,* vol. 47, pp. 1816-23, Nov 2004.

[137] J. F. Johanson, "Practicality of high-resolution chromoendoscopy during routine screening colonoscopy," *Gastrointest Endosc,* vol. 63, pp. 829-30, May 2006.

[138] T. Wilson, "Confocal microscopy," *Academic Press: London, etc,* vol. 426, pp. 1-64, 1990.

[139] G. S. Kino and T. R. Corle, *Confocal scanning optical microscopy and related imaging systems*: Academic Press, 1996.

[140] J. Pawley, *Handbook of biological confocal microscopy*: Springer, 2006.

[141] D. R. Sandison and W. W. Webb, "Background rejection and signal-to-noise optimization in confocal and alternative fluorescence microscopes," *Applied Optics,* vol. 33, pp. 603-615, 1994.

[142] D. M. Shotton, "Confocal scanning optical microscopy and its applications for biological specimens," *Journal of Cell Science,* vol. 94, pp. 175-206, 1989.

[143] W. M. Petroll, J. V. Jester, and H. D. Cavanagh, "In vivo confocal imaging: general principles and applications," *Scanning,* vol. 16, p. 131, 1994.

[144] J. Li, J. V. Jester, H. D. Cavanagh, T. D. Black, and W. M. Petroll, "On-line 3-dimensional confocal imaging in vivo," *Investigative Ophthalmology & Visual Science,* vol. 41, pp. 2945-2953, 2000.

[145] A. Diaspro, *Confocal and two-photon microscopy: foundations, applications, and advances* vol. 1: Wiley-Liss New York, 2002.

[146] B. Matsumoto, *Cell biological applications of confocal microscopy*: Academic Press, 2003.

[147] A. L. Polglase, W. J. McLaren, and P. M. Delaney, "Pentax confocal endomicroscope: a novel imaging device for in vivo histology of the upper and lower gastrointestinal tract," *Expert Rev Med Devices,* vol. 3, pp. 549-56, Sep 2006.

[148] K. B. Dunbar and M. I. Canto, "Confocal endomicroscopy," *Techniques in Gastrointestinal Endoscopy,* vol. 12, pp. 90-99, 2010.

[149] R. Kiesslich, M. Goetz, J. Burg, M. Stolte, E. Siegel, M. J. Maeurer, S. Thomas, D. Strand, P. R. Galle, and M. F. Neurath, "Diagnosing Helicobacter pylori in vivo by confocal laser endoscopy," *Gastroenterology,* vol. 128, pp. 2119-23, Jun 2005.

[150] A. L. Polglase, W. J. McLaren, S. A. Skinner, R. Kiesslich, M. F. Neurath, and P. M. Delaney, "A fluorescence confocal endomicroscope for in vivo microscopy of the upper- and the lower-GI tract," *Gastrointest Endosc,* vol. 62, pp. 686-95, Nov 2005.

[151] M. Wallace, G. Y. Lauwers, Y. Chen, E. Dekker, P. Fockens, P. Sharma, and A. Meining, "Miami classification for probe-based confocal laser endomicroscopy," *Endoscopy,* vol. 43, pp. 882-91, Oct 2011.

[152] A. Buda, F. Lamboglia, G. Hatem, R. D'Inca, and G. C. Sturniolo, "Evolving endoscopic technologies for the detection of dysplasia in inflammatory bowel diseases," *Ann Ital Chir,* vol. 82, pp. 29-35, Jan-Feb 2011.

[153] R. Kiesslich, J. Burg, M. Vieth, J. Gnaendiger, M. Enders, P. Delaney, A. Polglase, W. McLaren, D. Janell, S. Thomas, B. Nafe, P. R. Galle, and M. F. Neurath, "Confocal laser endoscopy for diagnosing intraepithelial neoplasias and colorectal cancer in vivo," *Gastroenterology,* vol. 127, pp. 706-13, Sep 2004.

[154] A. M. Buchner, M. W. Shahid, M. G. Heckman, M. Krishna, M. Ghabril, M. Hasan, J. E. Crook, V. Gomez, M. Raimondo, T. Woodward, H. C. Wolfsen, and M. B. Wallace, "Comparison of probe-based confocal laser endomicroscopy with virtual chromoendoscopy for classification of colon polyps," *Gastroenterology,* vol. 138, pp. 834-42, Mar 2010.

[155] M. W. Shahid, A. M. Buchner, E. Coron, T. A. Woodward, M. Raimondo, E. Dekker, P. Fockens, and M. B. Wallace, "Diagnostic accuracy of probe-based confocal laser endomicroscopy in detecting residual colorectal neoplasia after EMR: a prospective study," *Gastrointest Endosc,* vol. 75, pp. 525-33, Mar 2012.

[156] T. Kuiper, F. J. van den Broek, S. van Eeden, P. Fockens, and E. Dekker, "Feasibility and accuracy of confocal endomicroscopy in comparison with narrow-band imaging and chromoendoscopy for the differentiation of colorectal lesions," *Am J Gastroenterol,* vol. 107, pp. 543-50, Apr 2012.

[157] R. Kiesslich, M. Goetz, K. Lammersdorf, C. Schneider, J. Burg, M. Stolte, M. Vieth, B. Nafe, P. R. Galle, and M. F. Neurath, "Chromoscopy-guided endomicroscopy increases the diagnostic yield of intraepithelial neoplasia in ulcerative colitis," *Gastroenterology,* vol. 132, pp. 874-82, Mar 2007.

[158] D. P. Hurlstone, M. Thomson, S. Brown, N. Tiffin, S. S. Cross, and M. D. Hunter, "Confocal endomicroscopy in ulcerative colitis: differentiating dysplasia-associated lesional mass and adenoma-like mass," *Clin Gastroenterol Hepatol,* vol. 5, pp. 1235-41, Oct 2007.

[159] O. Watanabe, T. Ando, O. Maeda, M. Hasegawa, D. Ishikawa, K. Ishiguro, N. Ohmiya, Y. Niwa, and H. Goto, "Confocal endomicroscopy in patients with ulcerative colitis," *Journal of Gastroenterology and Hepatology,* vol. 23, pp. S286-S290, 2008.

[160] G. D. De Palma, S. Staibano, S. Siciliano, F. Maione, M. Siano, D. Esposito, and G. Persico, "In-vivo characterization of DALM in ulcerative colitis with high-resolution probe-based confocal laser endomicroscopy," *World J Gastroenterol,* vol. 17, pp. 677-80, Feb 7 2011.

[161] F. J. C. van den Broek, J. A. van Es, S. van Eeden, P. C. F. Stokkers, C. Y. Ponsioen, J. B. Reitsma, P. Fockens, and E. Dekker, "Pilot study of probe-based confocal laser endomicroscopy during

colonoscopic surveillance of patients with longstanding ulcerative colitis," *Endoscopy,* vol. 43, pp. 116-122, Feb 2011.

[162] A. Das, M. V. Sivak, Jr., A. Chak, R. C. Wong, V. Westphal, A. M. Rollins, J. Willis, G. Isenberg, and J. A. Izatt, "High-resolution endoscopic imaging of the GI tract: a comparative study of optical coherence tomography versus high-frequency catheter probe EUS," *Gastrointest Endosc,* vol. 54, pp. 219-24, Aug 2001.

[163] V. Westphal, A. M. Rollins, J. Willis, M. V. Sivak, and J. A. Izatt, "Correlation of endoscopic optical coherence tomography with histology in the lower-GI tract," *Gastrointest Endosc,* vol. 61, pp. 537-46, Apr 2005.

[164] L. Familiari, G. Strangio, P. Consolo, C. Luigiano, M. Bonica, G. Barresi, V. Barresi, P. Familiari, G. D'Arrigo, A. Alibrandi, A. Zirilli, W. Fries, and M. Scaffidi, "Optical coherence tomography evaluation of ulcerative colitis: the patterns and the comparison with histology," *Am J Gastroenterol,* vol. 101, pp. 2833-40, Dec 2006.

[165] B. Shen, G. Zuccaro, T. L. Gramlich, N. Gladkova, B. A. Lashner, C. P. Delaney, J. T. Connor, F. H. Remzi, M. Kareta, C. L. Bevins, F. Feldchtein, S. A. Strong, M. L. Bambrick, P. Trolli, and V. W. Fazio, "Ex vivo histology-correlated optical coherence tomography in the detection of transmural inflammation in Crohn's disease," *Clin Gastroenterol Hepatol,* vol. 2, pp. 754-60, Sep 2004.

[166] B. Shen, G. Zuccaro, Jr., T. L. Gramlich, N. Gladkova, P. Trolli, M. Kareta, C. P. Delaney, J. T. Connor, B. A. Lashner, C. L. Bevins, F. Feldchtein, F. H. Remzi, M. L. Bambrick, and V. W. Fazio, "In vivo colonoscopic optical coherence tomography for transmural inflammation in inflammatory bowel disease," *Clin Gastroenterol Hepatol,* vol. 2, pp. 1080-7, Dec 2004.

[167] D. C. Adler, C. Zhou, T. H. Tsai, J. Schmitt, Q. Huang, H. Mashimo, and J. G. Fujimoto, "Three-dimensional endomicroscopy of the human colon using optical coherence tomography," *Optics Express,* vol. 17, pp. 784-796, Jan 19 2009.

[168] W. Kang, H. Wang, Z. Wang, M. W. Jenkins, G. A. Isenberg, A. Chak, and A. M. Rollins, "Motion artifacts associated with in vivo endoscopic OCT images of the esophagus," *Optics Express,* vol. 19, pp. 20722-35, Oct 10 2011.

[169] P. R. Herz, Y. Chen, A. D. Aguirre, K. Schneider, P. Hsiung, J. G. Fujimoto, K. Madden, J. Schmitt, J. Goodnow, and C. Petersen, "Micromotor endoscope catheter for in vivo, ultrahigh-resolution optical coherence tomography," *Opt Lett,* vol. 29, pp. 2261-3, Oct 1 2004.

[170] W. Jung, D. T. McCormick, J. Zhang, L. Wang, N. C. Tien, and Z. P. Chen, "Three-dimensional endoscopic optical coherence tomography by use of a two-axis microelectromechanical scanning mirror," *Applied Physics Letters,* vol. 88, Apr 17 2006.

[171] J. J. Sun, S. G. Guo, L. Wu, L. Liu, S. W. Choe, B. S. Sorg, and H. K. Xie, "3D In Vivo optical coherence tomography based on a low-voltage, large-scan-range 2D MEMS mirror," *Optics Express,* vol. 18, pp. 12065-12075, Jun 7 2010.

[172] T. H. Tsai, B. Potsaid, M. F. Kraus, C. Zhou, Y. K. Tao, J. Hornegger, and J. G. Fujimoto, "Piezoelectric-transducer-based miniature catheter for ultrahigh-speed endoscopic optical coherence tomography," *Biomed Opt Express,* vol. 2, pp. 2438-48, Aug 1 2011.

[173] J. Li, M. de Groot, F. Helderman, J. Mo, J. M. Daniels, K. Grunberg, T. G. Sutedja, and J. F. de Boer, "High speed miniature motorized endoscopic probe for optical frequency domain imaging," *Optics Express,* vol. 20, pp. 24132-8, Oct 22 2012.

[174] J. Xi, Y. Chen, Y. Zhang, K. Murari, M. J. Li, and X. Li, "Integrated multimodal endomicroscopy platform for simultaneous en face optical coherence and two-photon fluorescence imaging," *Opt Lett,* vol. 37, pp. 362-4, Feb 1 2012.

[175] B. J. Vakoc, R. M. Lanning, J. A. Tyrrell, T. P. Padera, L. A. Bartlett, T. Stylianopoulos, L. L. Munn, G. J. Tearney, D. Fukumura, R. K. Jain, and B. E. Bouma, "Three-dimensional microscopy of the

tumor microenvironment in vivo using optical frequency domain imaging," *Nat Med,* vol. 15, pp. 1219-23, Oct 2009.

[176] G. Liu, W. Jia, V. Sun, B. Choi, and Z. Chen, "High-resolution imaging of microvasculature in human skin in-vivo with optical coherence tomography," *Optics Express,* vol. 20, pp. 7694-705, Mar 26 2012.

3. Prior Art in Optical Coherence Microscopy

3.1. Overview of OCM Imaging

As mentioned in the previous sections, OCM employs coherence gating in order to reject multiply scattered light. With the use of broadband light sources, an axial resolution of <10 um can be easily achieved, which is on the order of the thickness of histological slides and is argued to be necessary for obtaining cellular resolution images [1]. For confocal imaging, on the other hand, mainly the magnification of the objective determines the axial resolution of the system. The practical implication of having intrinsic high axial resolution for OCM imaging is that the axial and transverse resolutions are effectively decoupled in the system, such that the numerical aperture (NA) of the imaging objective can be reduced without losing axial resolution. Reducing the NA will translate into larger depth of field where the unique advantage of OCM, which enables depth resolved imaging, can be utilized to generate images from multiple depths without the need for physically translating the focus [2, 3].

As an example, Fig. 1 depicts the dependence of confocal range and transverse resolution to the NA of the objective at the 1060 nm and 1310 nm wavelengths. The confocal range is defined as the two sided distance (Rayleigh range) where the beam diameter increases by a factor of $\sqrt{2}$, and transverse resolution is defined as the radius where the beam intensity reduces to $1/e^2$ of its maximum value ($1/e^2$ spot size). The equations used to calculate these two parameters are given in Section 4.1. A beam diameter of 8 mm and water immersion objective is assumed for the calculations. From Fig. 1 (B) it can be observed that even for moderate NAs (< 0.4) a resolution better than 3 um can be achieved. On the other hand, the dependence of confocal range on the NA is more drastic as it scales inversely with the square of the NA. Hence to achieve cellular resolution solely by confocal imaging an NA > 0.8 is required. However, with OCT one can readily achieve cellular resolution with the coherence gate, eliminating the need for high NA objective to provide cellular axial resolution. Furthermore, lower NA imaging also enables to obtain images from deeper regions of the sample, as the multiple scattering effects would be reduced when the focus is translated into the sample [4]. Therefore, for OCM applications the NA of the objective can be selected to provide a desired transverse resolution and field of view, without consideration about losing the axial resolution.

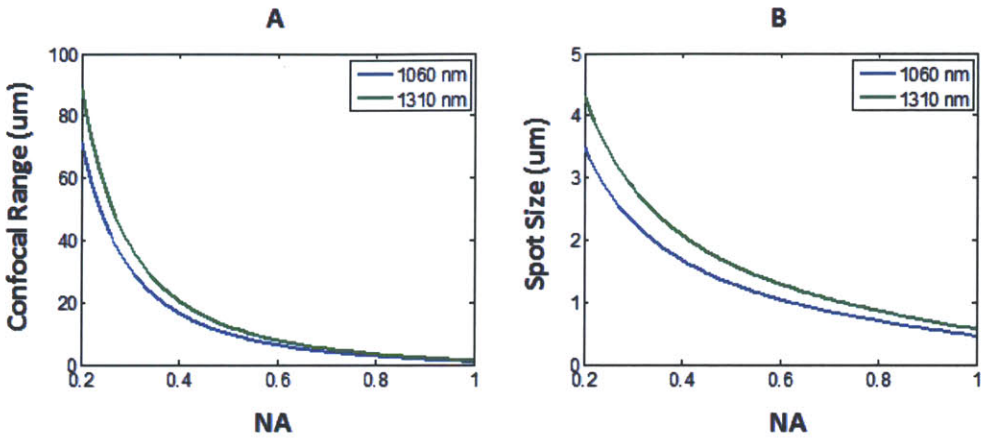

Figure 1: Dependence of confocal range (A) and transverse resolution (B) to the NA of the objective for two different wavelengths.

Next sections give an overview for the history of development of OCM systems, with a particular emphasis on their clinical applications. Similar to the developmental stages of OCT technology, OCM also evolved from time domain techniques to spectral domain and swept source imaging methods. The sections are divided into three categories based on these imaging methods, which will closely follow the development of the OCM technology. Discussion for the differences between these three techniques is also included outlining the advantages and disadvantages of each imaging method. An in depth theory about OCT and OCM will not be presented in this thesis. Readers are directed to some of the excellent book references that discusses the mathematical background of OCT and OCM imaging [5-7]. Moreover, there are also high quality, published doctoral dissertations that provides a solid background on the technical aspects of OCT and OCM imaging [8].

3.2. Time Domain OCM

Time domain OCT methods have the well know sensitivity disadvantage as they acquire images from a single depth, whereas Fourier domain methods acquire images from the entire depth range simultaneously [9]. Moreover, when cross sectional image needs to be generated, then the reference arm path length should be mechanically changed, which restricts the acquisition speed of the A-lines. These factors pose a serious limitation against the use of time domain OCT imaging methods. However, for OCM applications, if the *en face* image is to be generated from a single depth, then neither of these factors actually plays a decisive role. In fact, one can generate *en face* images with a speed limited by the maximum speed of the scanners in the system. For Fourier domain OCM, on the other hand, the axial scan (A-scan) rate is still a limiting factor for the achievable imaging speeds.

As previously mentioned, reference arm length is set to a fixed length for time domain OCM. However, instead of scanning the reference arm length, a phase modulator is employed in the reference arm in order to achieve a heterodyned optical signal. Note that, heterodyned detection is proven to dramatically improve the SNR of optical imaging systems by achieving nearly shot-noise limited detection [10]. Consequently, to generate time domain OCM images the interferometric signal is detected using a balanced detector, which is then band pass filtered and demodulated using either analog mixers or IQ-demodulators, or using digital filters and mixers after the heterodyne signal is sampled by the acquisition card. Note that the heterodyne frequency is typically on the order of 1-10 MHz, which is possible to acquire using standard digitizers or acquisition cards.

First demonstrations of OCM are published within the first years following the invention of the OCT technology [11, 12]. Note that in these studies, the phase delay in the reference arm is achieved using a piezoelectric fiber stretcher, which restricted the heterodyne frequency, consequently the imaging speeds, to a few kHz. This limitation slowed the development of real time OCM systems for several years until the development of grating based phase/delay scanners [13]. The next generation time domain OCM (TD-OCM) system employed this approach to achieve a 1 MHz heterodyne frequency [14]. Using a broadband Ti:Al_2O_3 laser centered around 800 nm, an axial resolution of 3 um is achieved, where the transverse resolution is set to 2 um by underfilling a 40X objective. *In vivo* imaging of *Xenopus laevis* tadpole and human skin from nailfold region has been demonstrated with this system.

Recently an integrated time domain OCT/OCM system have been demonstrated which uses a combination of a low power objective (10X) for OCT imaging and a high power objective (40X) for OCM imaging [15]. As the light source it uses a Nd:Glass laser which is spectrally broadened using a high NA fiber in order to provide an axial resolution of < 4 um. Moreover, an electro-optic waveguide modulator provides a phase modulation of 1 MHz for the reference arm light. Note that, for the OCT imaging mode, the reference arm length is scanned to generate cross sectional images. In this study images of *ex vivo* samples from the human GI tract is presented, which showed close correspondence to the histological appearance of these specimens [15]. Using the same system, several other *ex vivo* imaging studies have been conducted on different pathologies from various human tissues such as thyroid, breast and kidney [16-18].

3.3. Spectral/Fourier Domain OCM

Spectral/Fourier domain OCT (SD-OCT) systems employ a spectrometer in order to record the light spectrum corresponding to each transverse position (A-line) on the sample. Reflections from the sample are coded in the spectrum as a sinusoidal function in wavenumber. Hence, Fourier transformation of the spectrums produces the depth scans. The detector for the SD-

OCT systems is typically a line scan camera that records the spectrum of a single A-line. Hence, maximum line acquisition rate achievable by the camera typically sets the A-scan rate of the imaging system. Furthermore, conventional line scan cameras employ CCD or CMOS detectors, which are sensitive upto NIR wavelengths (< 1000 nm). Therefore, SD-OCT systems typically utilize a light source with a spectral band centered around 800 nm, where the water absorption and sample scattering is relatively small, and the camera still has a reasonable detection efficiency. For OCT applications, the sensitivity advantage of Fourier domain detection, as well as the dramatic increase for the imaging speed due to obtaining entire imaging depth from a single A-scan, caused a rapid shift in the OCT technology as SD-OCT replaced TD-OCT applications.

For OCM applications, the utilization of NIR light around 800 nm also opens the possibility of implementing an integrated OCM and multiphoton microscopy (MPM) system in order to simultaneously achieve molecular contrast. Note that for most of the intrinsic as well as extrinsic contrast agents employed in two photon (TPM) and second harmonic generation (SHG) microscopy systems, the excitation wavelength is typically around 700 – 850 nm range, whereas the emission wavelengths are typically around UV regime (300 – 550 nm), making it possible to use single light source for excitation for MPM as well as for SD-OCM imaging [19]. Consequently, some of the initial SD-OCM studies have employed integrated OCT and MPM imaging.

In one study by Vinegoni et al., a Ti:Sapphire laser centered at 800 nm with a bandwidth of 60 nm has been employed to generate simultaneous SD-OCM and MPM images with 4.7 um coherence gate, 2.2 um confocal gate and 0.9 um transverse OCT resolution over a 600 um x 600 um field of view at a 29 kHz A-scan rate [20]. Using an extremely high power objective (NA = 0.95), OCM and MPM images from fibroblast cell cultures have been demonstrated with very fine cellular and molecular detail. In an extension to this study, spectrums obtained from different regions of single cells are processed using light scattering spectroscopy (LSS) techniques, in order to enhance contrast of the OCM images [21]. Confirmed by the corresponding MPM images, where a nuclei specific stain is employed, this study clearly showed that for imaging of singular cells, regions occupied by cell nuclei produces spectral oscillations consistent with the predictions of Mie theory [22]. However, this effect was less pronounced when the bulk tissue excised from a rat muscle was analyzed with the same LSS analysis method [21]. In another study with combined SD-OCM and MPM system, mean scattering intensity and scattering area from different organelles have been quantitatively measured and it has been found that the scattering from nuclei is actually more than a factor of 2 smaller than the scattering from other organelles such as mitochondria and actin filaments [23]. Nevertheless, these studies demonstrate another advantage of Fourier domain detection over TD-OCM, where spectrums can be processed to enhance the contrast in OCM images.

Another advantage of SD-OCT and SD-OCM systems are the very high phase stability of the imaging setup. Especially when a common path interferometer is employed, where the reflection from the cover slip surface acts as the reference arm signal, an extremely high phase stability of a few milliradian can be achieved. This phase stability of SD-OCM systems can be exploited to achieve phase contrast imaging as well as to provide sub-micron accuracy for measuring displacements in the living cells or tissues. Indeed several SD-OCM studies have used this approach to generate phase contrast and functional images and measuring variations in the optical path lengths as small as 2 nm [24-27]. The ability of measuring phase of the back reflected beam also opens the possibility of numerical algorithms to correct for aberrations or the defocusing effects on the OCM images. An extension of this approach is employed in interferometric synthetic aperture microscopy (ISAM), which provided isotropic transverse resolution by numerically extending the depth of focus upto 1 mm even when a high NA objective is used in the imaging setup [28-30].

There are also several studies that used hardware based approaches to extend the depth of field of the SD-OCM images. Using a specially designed Axicon lens it is shown that it is possible to have a nearly constant transverse resolution of 1.5 um along a focal range about 200 um, which represents an increase in the depth of focus by an order of magnitude [31]. Another approach to extend depth of focus is to apodize the central portion of the collimated beam incident onto the back focal plane of the objective, which results in a bessel-gaussian beam around the focal plane. Using this method a SD-OCM system has been recently demonstrated which achieves about 2 um transverse and 1 um axial resolution along the first 300 – 400 um depth of the tissue [32]. Imaging of *ex vivo* human and swine coronary samples have been demonstrated in this study where cellular features and single cell organisms such as lymphocytes, monocytes and macrophages were identifiable in the resulting cross sectional OCT images. Here it should be noted that both of these methods for depth of field extension sacrifice sensitivity as the main lobe of the resulting gaussian-bessel beam contain only a fraction of the total energy [33]. The loss of sensitivity is typically on the order of 10 – 20 dB, depending on the depth of field extension that will be achieved, which is detrimental especially in an *in vivo* imaging setting as one cannot increase the light exposure to account for the loss of sensitivity. For *ex vivo* OCM imaging, on the other hand, incident light power can be scaled or several volumes from the same region can be averaged to counteract the loss of sensitivity.

Furthermore, the unique advantage of Fourier domain detection which acquires images from the entire depth range also allows for correcting of the curvatures in the scan field caused by the non-telecentricity of the imaging configuration as well as the aberrations of the objective lens. In the literature several SD-OCM studies have been demonstrated correction for this effect using a calibration field (notice that a detailed description on this phenomenon and methods on how to correct for it will be given in Section 4.8) [34, 35]. Consequently, using an

integrated SD-OCM and MPM system, *in vivo* cellular resolution images from human skin have been demonstrated [35, 36].

3.4. Swept Source/Fourier Domain OCM

In swept source/Fourier domain OCT (SS-OCT) systems, at any given instantaneous time only a narrow band of the full spectral bandwidth is incident on the sample. By mechanically changing the cavity length of the light source, this spectral band is swept across the full bandwidth of the spectrum as a function of time. Therefore, the rate which the instantaneous linewidth scans the spectrum sets the imaging speed (A-scan rate) for SS-OCT systems. For SS-OCT systems, a high frequency photodetector followed by a digitizer card is used to acquire spectrums as a function of time. Note that, the availability of photodetectors for the IR range opens up the possibility of utilizing light sources at 1 um as well as 1.3 um, which have less scattering and increased penetration depth compared to using a spectral band around 800 nm [37, 38].

The SS-OCT technology is gaining increasing acceptance in the OCT community as the scan rates achievable with it exceeds the line rate of the cameras employed by the SD-OCT systems. Using a swept source, Fourier-domain mode-locked (FDML) laser, an A-scan rate of upto 5.2 and 1.37 MHz has been demonstrated at 1.3 um and 1 um, respectively [39, 40]. Note that the current state of art line scan cameras can provide A-scan rates at most 300 kHz, which limits the maximum achievable scan rate of the SD-OCT systems.

Application of OCM with a swept source light source (SS-OCM), on the other hand, has not been utilized widely so far. One reason for this is the non existence of high speed swept source lasers until recently, which occluded real time imaging. Moreover, compared to light sources employed in SD-OCT systems, achieving broad tuning range for the swept source light sources operating at 1 um and 1.3 um is more challenging, which limits the axial resolution of the imaging system. Although there is no definitive consensus on this subject, it has been argued that an axial resolution of < 5 um is required for achieving cellular resolution imaging in highly scattering biological samples, which necessitates a tuning range of > 150 nm for longer wavelengths [1]. Upto date a swept source light source which exhibits both high speed and broad tuning range was not existent.

In one of the few SS-OCM studies in the literature, an FDML laser with a tuning range of 110 nm has been employed, which operated at 42 kHz [41]. Using an objective with effective NA of 0.35, a transverse resolution of 1.6 um and axial resolution of 8 um has been achieved in tissue. In this study, *in vivo* cellular images of *Xenopus laevis* tadpole as well as fixed rat kidney and images from *ex vivo* human colonic tissue have been demonstrated. In another study a binary phase spatial filter is employed in order to extend the depth of focus of the SS-OCM system by a factor of 10 [42]. This system used a modified version of a commercial SS-OCT

system as the light source which worked at 16 kHz. Note that as discussed in the previous section, the use of Bessel beams caused a reduction about 20 dB in the sensitivity of the OCM system. In the same study, images from microsphere phantoms have been shown to illustrate the extended depth of focus of the system.

Recently, a new technology for generating wavelength swept light source, named as micro-electro-mechanical systems (MEMS) tunable Vertical-cavity Surface-emitting Laser (VCSEL), has been adapted for OCT imaging [43, 44]. Due to its extremely small cavity length of a few mm, this laser has the unique feature that it exhibits extremely long coherence length, hence the fall off on the sensitivity with respect to increased path length difference, typically seen in SD-OCT and SS-OCT systems, are not observed through the whole imaging range (note that that there might be still some fall off due to decreased detector response at higher frequencies). Recently our group have shown the first demonstration of this technology in ophthalmic imaging achieving a variable sweep rate from 60 kHz upto 1.2 MHz [45]. Note that this laser also has the advantage of being very compact, which is an important factor if the system needs to be employed in a clinical setting, such as pathology laboratory or endoscopy suite. Furthermore, newer generation of VCSEL lasers have expected to achieve a broad tuning range of 160 nm at 1.3 um, which will achieve an axial resolution of < 5 um.

3.5. Comparison of OCM Imaging Methods

In the previous sections a general overview and literature review of several OCM imaging methods has been presented. Some of the key concepts of the respective imaging modalities will be re-iterated here in order to put the discussion into perspective.

TD-OCT has been replaced by the Fourier domain imaging methods in the state of the art applications of OCT, mainly due to the speed and sensitivity disadvantage of this technique. However, for OCM these two main factors do not play a dissuasive role. In fact, the speed of OCM for acquiring *en face* images is still faster than either SS-OCM or SD-OCM, because the heterodyne modulation frequency that can be used by the former modality is higher than the current A-scan rates achievable by the latter techniques.

On the other hand, these advantages of TD-OCM methods are offset by the limitation of not being able acquire images simultaneously from several depths. As it has been discussed in Chapter 2, being able to visualize depth dependent features are significant for grading as well as determining extend of invasion or the neoplastic progression. Moreover, this property also enables to correct for the curvatures in the scan field as will be seen in Section 4.8. Furthermore, obtaining spectral information opens up the possibility of using numerical techniques to correct for dispersion, aberrations or defocusing effects, as well as to enhance the contrast of images or extract quantitative information related to the composition of the

tissue, such as nuclear size and density. Due to these unique advantages of Fourier domain imaging methods, it is the author's content that SS-OCM and SD-OCM will replace TD-OCM imaging, parallel to the evolution of OCT applications.

As for the comparison of SD-OCM and SS-OCM techniques, it can be observed that majority of the current OCM systems are utilizing the former method. This can be argued to be mainly related to the unavailability of high speed, broad band swept source light sources. Furthermore, even if the A-scan rate of SD-OCM system is not as fast as the SS-OCM system, this was not perceived as a limiting factor as the imaging speed for an *ex vivo* application is not considered as critical as it is for *in vivo* imaging applications, where in order to prevent motion artifacts it is certainly crucial to acquire images with high frame rates. However, for the translation of the OCM imaging to endoscopic applications, as well as for the scenario where OCM provides real time feedback for intraoperative guidance, imaging speeds will still be demanding. Furthermore, acquisition of the spectrums only require the use of a photodetector and acquisition card, which is more convenient for a clinical setting as opposed to the requirement of a precisely aligned spectrometer for the SD-OCM systems.

The development of VCSEL technology and its application to OCT imaging opens up new venues where very simultaneously high speeds (> 1 MHz) and broad tuning ranges (> 150 nm) will be achievable with a SS-OCM system. Moreover, the small footprint of the light source is especially useful for building a portable system that can be used in the pathology laboratory or in a GI suite. For these reasons, in the course of the project which this thesis is based on, it has been decided to explore the utility of the VCSEL light source for the OCM application.

References

[1] M. Rajadhyaksha, R. R. Anderson, and R. H. Webb, "Video-rate confocal scanning laser microscope for imaging human tissues in vivo," *Appl Opt,* vol. 38, pp. 2105-15, Apr 1 1999.

[2] M. Kempe and W. Rudolph, "Analysis of heterodyne and confocal microscopy for illumination with broad-bandwidth light," *Journal of Modern Optics,* vol. 43, pp. 2189-2204, Oct 1996.

[3] M. Kempe, W. Rudolph, and E. Welsch, "Comparative study of confocal and heterodyne microscopy for imaging through scattering media," *Journal of the Optical Society of America a-Optics Image Science and Vision,* vol. 13, pp. 46-52, Jan 1996.

[4] A. L. Clark, A. Gillenwater, R. Alizadeh-Naderi, A. K. El-Naggar, and R. Richards-Kortum, "Detection and diagnosis of oral neoplasia with an optical coherence microscope," *Journal of Biomedical Optics,* vol. 9, pp. 1271-1280, Nov-Dec 2004.

[5] B. E. Bouma and G. J. Tearney, *Handbook of optical coherence tomography*. New York: Marcel Dekker, 2002.

[6] M. E. Brezinski, *Optical coherence tomography : principles and applications*. Amsterdam ; Boston: Academic Press, 2006.

[7] W. Drexler and J. G. Fujimoto, *Optical coherence tomography : technology and applications*. Berlin ; New York: Springer, 2008.

[8] A. D. Aguirre, "Advances in Optical Coherence Tomography and Microscopy for endoscopic applications and functional neuroimaging," Ph D, Harvard-MIT Division of Health Sciences and Technology, 2008.

[9] M. Choma, M. Sarunic, C. Yang, and J. Izatt, "Sensitivity advantage of swept source and Fourier domain optical coherence tomography," *Optics Express,* vol. 11, pp. 2183-9, Sep 8 2003.

[10] T. Sawatari, "Optical heterodyne scanning microscope," *Appl Opt,* vol. 12, pp. 2768-72, Nov 1 1973.

[11] J. A. Izatt, M. R. Hee, G. M. Owen, E. A. Swanson, and J. G. Fujimoto, "Optical coherence microscopy in scattering media," *Opt Lett,* vol. 19, pp. 590-2, Apr 15 1994.

[12] J. A. Izatt, M. D. Kulkarni, H. W. Wang, K. Kobayashi, and M. V. Sivak, "Optical coherence tomography and microscopy in gastrointestinal tissues," *Ieee Journal of Selected Topics in Quantum Electronics,* vol. 2, pp. 1017-1028, Dec 1996.

[13] G. J. Tearney, B. E. Bouma, and J. G. Fujimoto, "High-speed phase- and group-delay scanning with a grating-based phase control delay line," *Opt Lett,* vol. 22, pp. 1811-3, Dec 1 1997.

[14] A. D. Aguirre, P. Hsiung, T. H. Ko, I. Hartl, and J. G. Fujimoto, "High-resolution optical coherence microscopy for high-speed, in vivo cellular imaging," *Opt Lett,* vol. 28, pp. 2064-6, Nov 1 2003.

[15] A. D. Aguirre, Y. Chen, B. Bryan, H. Mashimo, Q. Huang, J. L. Connolly, and J. G. Fujimoto, "Cellular resolution ex vivo imaging of gastrointestinal tissues with optical coherence microscopy," *Journal of Biomedical Optics,* vol. 15, p. 016025, Jan-Feb 2010.

[16] C. Zhou, D. W. Cohen, Y. H. Wang, H. C. Lee, A. E. Mondelblatt, T. H. Tsai, A. D. Aguirre, J. G. Fujimoto, and J. L. Connolly, "Integrated Optical Coherence Tomography and Microscopy for Ex Vivo Multiscale Evaluation of Human Breast Tissues," *Cancer Research,* vol. 70, pp. 10071-10079, Dec 15 2010.

[17] C. Zhou, Y. H. Wang, A. D. Aguirre, T. H. Tsai, D. W. Cohen, J. L. Connolly, and J. G. Fujimoto, "Ex vivo imaging of human thyroid pathology using integrated optical coherence tomography and optical coherence microscopy," *Journal of Biomedical Optics,* vol. 15, Jan-Feb 2010.

[18] H. C. Lee, C. Zhou, D. W. Cohen, A. E. Mondelblatt, Y. H. Wang, A. D. Aguirre, D. J. Shen, Y. Sheikine, J. G. Fujimoto, and J. L. Connolly, "Integrated Optical Coherence Tomography and Optical Coherence Microscopy Imaging of Ex Vivo Human Renal Tissues," *Journal of Urology,* vol. 187, pp. 691-699, Feb 2012.

[19] W. R. Zipfel, R. M. Williams, and W. W. Webb, "Nonlinear magic: multiphoton microscopy in the biosciences," *Nat Biotechnol,* vol. 21, pp. 1369-77, Nov 2003.

[20] C. Vinegoni, T. Ralston, W. Tan, W. Luo, D. L. Marks, and S. A. Boppart, "Integrated structural and functional optical imaging combining spectral-domain optical coherence and multiphoton microscopy," *Applied Physics Letters,* vol. 88, Jan 30 2006.

[21] C. Y. Xu, C. Vinegoni, T. S. Ralston, W. Luo, W. Tan, and S. A. Boppart, "Spectroscopic spectral-domain optical coherence microscopy," *Optics Letters,* vol. 31, pp. 1079-1081, Apr 15 2006.

[22] A. Wax, C. H. Yang, and J. A. Izatt, "Fourier-domain low-coherence interferometry for light-scattering spectroscopy," *Optics Letters,* vol. 28, pp. 1230-1232, Jul 15 2003.

[23] S. Tang, C. H. Sun, T. B. Krasieva, Z. P. Chen, and B. J. Tromberg, "Imaging subcellular scattering contrast by using combined optical coherence and multiphoton microscopy," *Optics Letters,* vol. 32, pp. 503-505, Mar 1 2007.

[24] M. A. Choma, A. K. Ellerbee, C. Yang, T. L. Creazzo, and J. A. Izatt, "Spectral-domain phase microscopy," *Opt Lett,* vol. 30, pp. 1162-4, May 15 2005.

[25] C. Joo, T. Akkin, B. Cense, B. H. Park, and J. F. de Boer, "Spectral-domain optical coherence phase microscopy for quantitative phase-contrast imaging," *Opt Lett,* vol. 30, pp. 2131-3, Aug 15 2005.

[26] M. A. Choma, A. K. Ellerbee, S. Yazdanfar, and J. A. Izatt, "Doppler flow imaging of cytoplasmic streaming using spectral domain phase microscopy," *Journal of Biomedical Optics,* vol. 11, p. 024014, Mar-Apr 2006.

[27] C. Joo, K. H. Kim, and J. F. de Boer, "Spectral-domain optical coherence phase and multiphoton microscopy," *Opt Lett,* vol. 32, pp. 623-5, Mar 15 2007.

[28] T. S. Ralston, D. L. Marks, P. S. Carney, and S. A. Boppart, "Interferometric synthetic aperture microscopy," *Nature Physics,* vol. 3, pp. 129-134, Feb 2007.

[29] T. S. Ralston, D. L. Marks, P. S. Carney, and S. A. Boppart, "Real-time interferometric synthetic aperture microscopy," *Optics Express,* vol. 16, pp. 2555-69, Feb 18 2008.

[30] T. S. Ralston, S. G. Adie, D. L. Marks, S. A. Boppart, and P. S. Carney, "Cross-validation of interferometric synthetic aperture microscopy and optical coherence tomography," *Optics Letters,* vol. 35, pp. 1683-1685, May 15 2010.

[31] R. A. Leitgeb, M. Villiger, A. H. Bachmann, L. Steinmann, and T. Lasser, "Extended focus depth for Fourier domain optical coherence microscopy," *Optics Letters,* vol. 31, pp. 2450-2452, Aug 15 2006.

[32] L. Liu, J. A. Gardecki, S. K. Nadkarni, J. D. Toussaint, Y. Yagi, B. E. Bouma, and G. J. Tearney, "Imaging the subcellular structure of human coronary atherosclerosis using micro-optical coherence tomography," *Nat Med,* vol. 17, pp. 1010-4, Aug 2011.

[33] K. S. Lee, "Extended focus range high resolution endoscopic optical coherence tomography," University of Central Florida Orlando, Florida, 2008.

[34] B. W. Graf, S. G. Adie, and S. A. Boppart, "Correction of coherence gate curvature in high numerical aperture optical coherence imaging," *Opt Lett,* vol. 35, pp. 3120-2, Sep 15 2010.

[35] B. W. Graf and S. A. Boppart, "Multimodal In Vivo Skin Imaging with Integrated Optical Coherence and Multiphoton Microscopy," *Ieee Journal of Selected Topics in Quantum Electronics,* vol. 18, pp. 1280-1286, Jul-Aug 2012.

[36] Y. B. Zhao, B. W. Graf, E. J. Chaney, Z. Mahmassani, E. Antoniadou, R. DeVolder, H. Kong, M. D. Boppart, and S. A. Boppart, "Integrated multimodal optical microscopy for structural and functional imaging of engineered and natural skin," *Journal of Biophotonics,* vol. 5, pp. 437-448, May 2012.

[37] D. Kobat, M. E. Durst, N. Nishimura, A. W. Wong, C. B. Schaffer, and C. Xu, "Deep tissue multiphoton microscopy using longer wavelength excitation," *Optics Express,* vol. 17, pp. 13354-13364, Aug 3 2009.

[38] V. J. Srinivasan, H. Radhakrishnan, J. Y. Jiang, S. Barry, and A. E. Cable, "Optical coherence microscopy for deep tissue imaging of the cerebral cortex with intrinsic contrast," *Optics Express,* vol. 20, pp. 2220-2239, Jan 30 2012.

[39] W. Wieser, B. R. Biedermann, T. Klein, C. M. Eigenwillig, and R. Huber, "Multi-Megahertz OCT: High quality 3D imaging at 20 million A-scans and 4.5 GVoxels per second," *Optics Express,* vol. 18, pp. 14685-14704, Jul 5 2010.

[40] T. Klein, W. Wieser, C. M. Eigenwillig, B. R. Biedermann, and R. Huber, "Megahertz OCT for ultrawide-field retinal imaging with a 1050nm Fourier domain mode-locked laser," *Optics Express,* vol. 19, pp. 3044-3062, Feb 14 2011.

[41] S. W. Huang, A. D. Aguirre, R. A. Huber, D. C. Adler, and J. G. Fujimoto, "Swept source optical coherence microscopy using a Fourier domain mode-locked laser," *Optics Express,* vol. 15, pp. 6210-7, May 14 2007.

[42] L. Liu, C. Liu, W. C. Howe, C. J. Sheppard, and N. Chen, "Binary-phase spatial filter for real-time swept-source optical coherence microscopy," *Opt Lett,* vol. 32, pp. 2375-7, Aug 15 2007.

[43] V. Jayaraman, J. Jiang, H. Li, P. Heim, G. Cole, B. Potsaid, J. G. Fujimoto, and A. Cable, "OCT imaging up to 760kHz axial scan rate using single-mode 1310nm MEMS-tunable VCSELs with> 100nm tuning range," in *CLEO: Science and Innovations*, 2011.

[44] V. Jayaraman, J. Jiang, B. Potsaid, G. Cole, J. Fujimoto, and A. Cable, "Design and performance of broadly tunable, narrow line-width, high repetition rate 1310nm VCSELs for swept source optical coherence tomography," in *Proc. of SPIE Vol*, 2012, pp. 82760D-1.

[45] B. Potsaid, V. Jayaraman, J. G. Fujimoto, J. Jiang, P. J. S. Heim, and A. E. Cable, "MEMS tunable VCSEL light source for ultrahigh speed 60kHz-1MHz axial scan rate and long range centimeter class OCT imaging," in *SPIE BiOS*, 2012, pp. 82130M-82130M-8.

4. Swept Source OCM System Development and Characterization

4.1. Sample Arm Design

Figure 1 depicts the sample arm design employed in VCSEL OCM system. This design consists of a collimator lens (f_c = 11 mm), a compound scan lens (f_s = 37.5 mm), a compound tube lens (f_t = 86 mm), an objective lens (f_a), and a pair of galvanometer scanning mirrors in order to raster scan the beam in the two transverse directions. The combination of the focal lengths for the collimator, scan and tube lenses, and objective sets the magnification of the imaging system and the resulting transverse resolution, confocal range and field of view.

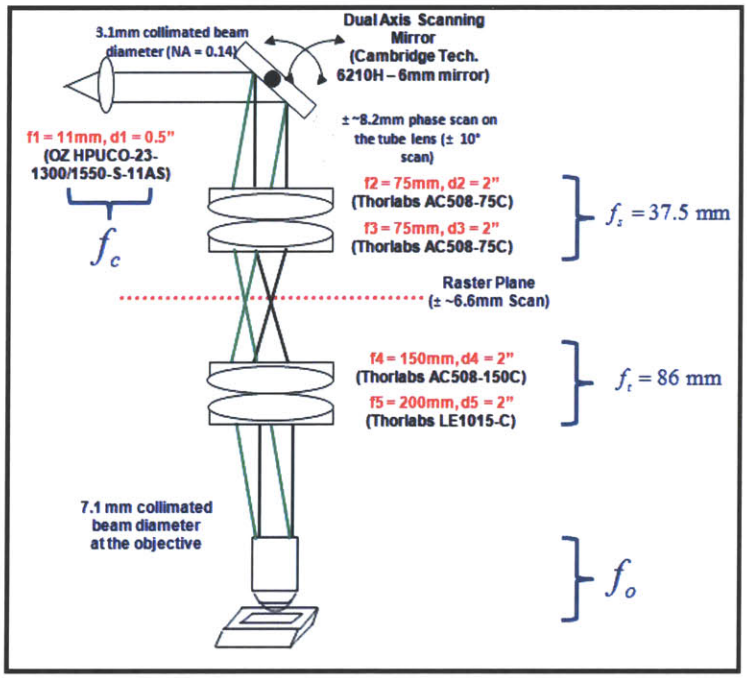

Figure 1: Sample arm design with representative components, beam and scan sizes, for the 1310 nm VCSEL OCM System. For the sample arm of the 1060 nm VCSEL system, the collimator is replaced with a collimator designed and coated for the respective wavelength (Thorlabs TC12APC-1064), which nevertheless has the same focal length. Note that the scan and tube lenses work with good performance for both 1060 nm and 1310 nm wavelengths, hence they are employed in both systems. The scanning mirrors employed in this system are analog galvos with a 6 mm mirror diameter (Model 6210H, Cambridge Tech, Bedford, MA).

The beam sizes and scan ranges are also included in Fig. 1, which are calculated assuming a 1310 nm light source. For calculating the collimated beam size, the formula $d = 2f_c \tan\left(\sin^{-1}\left(NA\right)\right)$ is used where an NA of 0.14 is used for the SFM28 fiber used for the 1310 nm system and for the HI1060 fiber used in the 1060 nm system. The beam angle scans the back focal plane of the objective with a magnification set by the ratio f_t / f_s. The $1/e^2$ spot

size (ω_0) incident on the sample can be calculated using $\lambda f_o / d_o$, where λ is the center wavelength of the light source and d_o is the collimated beam diameter after it has been magnified. The focal length of the objective can be found by dividing the reference tube length of the objective to the magnification of it. For instance, the reference tube length for the Olympus objectives are 180 mm, which means that the effective focal length of the 40X objective would be 4.5 mm. For the Zeiss objectives, on the other hand, the reference tube lengths are 165 mm. The FWHM spot size can be calculated from ω_0 by using the scale factor 1.175. Note that ω_0 can also be calculated by finding the magnification from the fiber tip to the focal plane of the objective, however, in order to find the collimated beam diameter and the scan angles it is more convenient to use the formulas given here. Finally, the confocal parameter, which is defined as the two sided distance where the beam diameter increases by a factor of $\sqrt{2}$, can be calculated using $\frac{2\pi\omega_0^2}{\lambda}$ [1]. The field of view can be calculated by noting that the scan on the raster plane will be ±6.6 mm ($f_s \tan(\phi)$), when the scanning mirrors perform a ±10 degree scan ($\phi = 10^\circ$). This scan is then demagnified by a value given by the ratio of focal lengths of the tube lens and the objective.

Table 1 gives the theoretical calculations for spot size, confocal parameter and field of view for three objectives that is identified to be suitable for this project. These objectives are water immersion which will reduce back reflections from the objective-cover glass surface. Furthermore, compared to regular objectives used for light microscopes that have less than 30% transmission at longer wavelengths, the objectives selected here also have reasonably good throughput at 1.3 um (~50%).

Objective	NA	Focal Length (mm)	Theoretical (1/e^2) Spot Size for the Incident Beam – w0 (um)	Theoretical (FWHM) Spot Size for the Incident Beam (um)	Theoretical Confocal Parameter (2*zr) – um	Field of View for 10 degree galvo scan	Wavelength
Zeiss 10x - W	0.3	16.5	3.04	3.58	44	2500	
Zeiss 20x - W	0.5	8.25	1.52	1.79	11	1250	1310 nm
Olympus 40x -W	0.8	4.5	0.83	0.98	3.3	775	
Zeiss 10x - W	0.3	16.5	2.72	3.2	43.9	2500	
Zeiss 20x - W	0.5	8.25	1.36	1.6	11	1250	1060 nm
Olympus 40x -W	0.8	4.5	0.74	0.87	3.25	775	

Table 1: Theoretical spot sizes, confocal parameters and field of views for three different water immersion objectives for 1060 nm and 1310 nm wavelengths. Part numbers of the objectives are: Olympus 40X - LUMPLFL 40XW/IR2, Zeiss 20X - N-ACHROPLAN 420957, and Zeiss 10X - ACHROPLAN 440039.

The scan and tube lenses essentially image the back focal plane of the objective onto the scanning mirrors. However, as there is a physical distance between the two scanning mirrors, the back focal plane can not be imaged onto the two scanning mirrors simultaneously with this imaging configuration. This imaging setup is termed as non-telecentric, which causes the scan field to be curved at the focus of the objective. Note that, it is possible to design a telecentric microscope using two separate scanning mirrors and putting relay lenses in between, hence to image the back focal plane of the objective precisely to both of the mirrors. However, this approach did not pursed here, as it will make the system more bulky, cause additional light loss and will make the alignment more challenging. All these factors are undesired if the system is to be used in a clinical setting. Furthermore, as it is mentioned previously, it is possible to correct for this scan field curvature in the post processing as will be seen in Section 4.8, which marks a significant advantage of Fourier domain detection methods as opposed to timed domain OCM applications.

The sample holder depicted in Fig. 1 is a modified cassette used in standard histological processing, in which a cover slip has been mounted on its top to provide an imaging window. A tissue embedding sponge is put below the sample which helps to press it to the cover glass in order to provide a flat surface for the imaging. After imaging is performed, sample can be fixed into formalin and transported directly to the histological processing without the need of removing from the cassette. This will ensure corresponding fields to be visualized for the OCM images and for the H&E slides.

4.2. Reference Arm and Interferometer Design

Schematic of the internally clocked 1310 nm VCSEL OCM system is shown in Fig. 2. The light source is a 1310 nm swept source VCSEL laser, which is routed either to the MZI arm or to the imaging arm. In the MZI arm, a fringe signal from the middle of the imaging range is recorded, which is used to calibrate subsequent spectrums as described in Section 4.6. In the imaging arm, light is divided into the sample and reference arms using a fiber coupler. Note that, reference arm has a single pass design which necessitates a fiber spool or an extra fiber coupler to be inserted into its path in order to match the fiber lengths between the sample and reference arms. The glasses put into the reference arm provide dispersion matching due to the extra optical components in the sample arm. Note that, due to single pass design of it, double amount of the glass as there is in the sample arm needs to be inserted to the reference arm, which potentially might necessitate 20 – 30 cm of glass. Instead, the fiber length of the reference arm is made longer than the sample arm in order to account for some of the mismatch in the optical path.

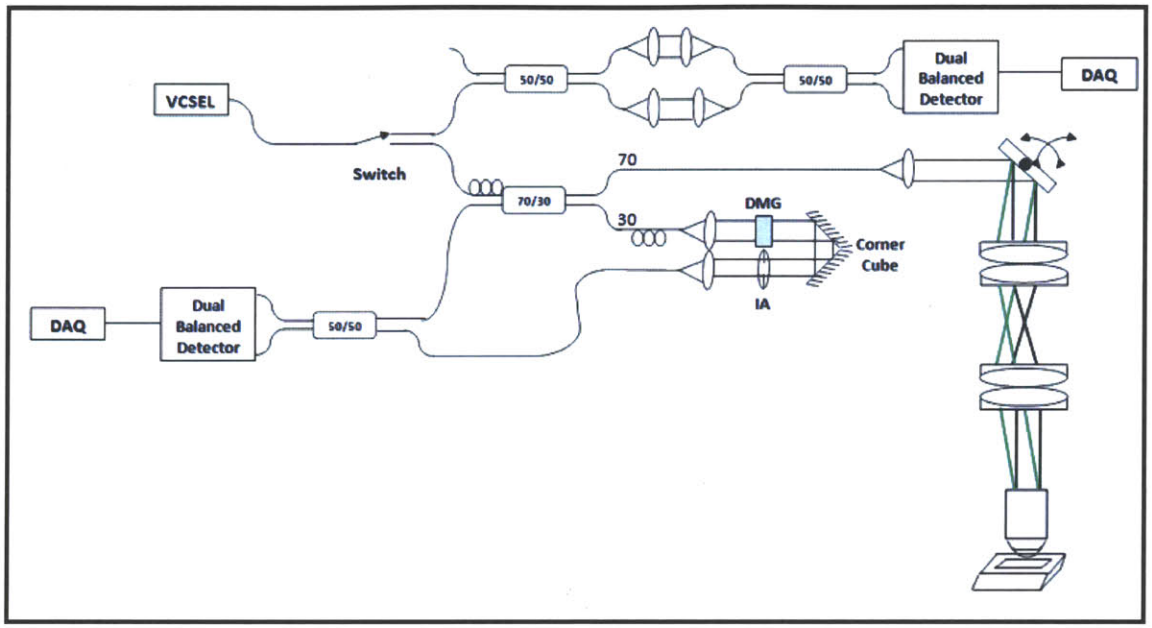

Figure 2: Schematic of the VCSEL OCM System. DAQ: Data acquisition card (Alazar 500 MHz – ATS9350, AlazarTech, Pointe-Claire, QC). DMG: Dispersion matching glass. IA: Iris attenuator. The balanced detector employed in the system is a prototype from Thorlabs which has a bandwidth of 200 MHz.

An iris attenuator is inserted to the reference arm in order to attenuate the excess light. Note that due to high noise rejection of the balanced detector, a reference arm light < 20 uW is usually sufficient, hence the light passing through to the reference arm needs to be attenuated significantly. It has been observed that iris attenuator is a better choice than variable ND filters typically used in the SD-OCT systems, as the small thickness of the ND filter causes extra reflections in the images, especially with the long coherence range of the VCSEL laser.

4.3. Light Sources and Other Hardware Components

The 1060 nm OCM system uses a prototype turnkey VCSEL light source from Thorlabs, which run with optical clocking. This VCSEL module had internal wavelength and power sensors to detect and adjust sweeping behavior of the laser, hence did not require manual adjustment to operate. Therefore, the design only included the imaging arm of the system depicted in Fig. 2. This system worked at an A-scan rate of 100 kHz (sweep rate = 50 kHz). The output power of the light source is ~ 15 mW. The laser produces a sweep with 80 nm tuning range centered around 1060 nm.

The 1310 nm VCSEL source, on the other hand, produces a sweep with a 120 nm tuning range with an output power of ~30 mW. A signal generator is connected to the input of the MEMS circuitry of the light source, which produced a sinusoidal waveform to drive the laser cavity. The amplitude and offset levels of the waveform is carefully adjusted to adjust the

tuning range to its highest value while preventing snapdown of the cavity. For this system a sweep frequency of 280 kHz is used, which is the resonance frequency of the VCSEL and therefore ensures the laser to work in the most stable region and gives the broadest tuning range. Since the sweeps are double sided, with a 280 kHz driving frequency the effective A-scan rate of the system is 560 kHz, which is faster by a factor of 5 compared to the state of the art commercial swept source lasers. Furthermore, by sacrificing some of the tuning range and stability it is possible to run the laser off resonance and achieve even faster imaging speeds.

The data acquisition card used in both of the OCM systems is a 500 MHz card from AlazarTech (Pointe-Claire, QC). It has two input channels, which can be operated simultaneously by reducing the effective sampling rate of each channel to half (500 KS/s). It has a 12 bit depth for both of the channels, and can digitize from ±40 mV upto ±4V. It supports external clocking, which is critical to implement optical clocking, and allows a clock frequency upto 500 MHz. It requires a clock input of at least 200 mV for external clocking. It also has a trigger input which allows the synchronization of the laser sweeps with the acquisition of the A-lines.

Both of the 1060 nm and 1310 nm systems also employ an analog I/O card (NI PCI-6751, National Instruments, Austin, TX) for driving the scanning mirrors, as well as for synchronization purposes explained in Section 4.4. This card supports 4 analog outputs at 16 bit depth and also has an input channel allowing for external clocking.

The 1310 nm OCM system is used both with internally clocked mode, which required the MZI fringes for calibration, and with optically clocked mode. For optical clocking a small portion of the VCSEL output is constantly fed to the MZI arm depicted in Fig. 2. Then the analog MZI signal which had a nearly gaussian envelope is converted to an optical clock signal with equal amplitude using a Thorlabs prototype pulse shaper and sent to the external clock input of the DAQ. Optical clocking ensures the fringes to be sampled equal in wavenumber and does not necessitate an additional calibration signal. Details on this process are explained in Section 4.6. Note that, the frequency generated by the path length difference in the MZI arm sets the maximum imaging depth of the system. As a 500 MHz DAQ (ATS9350, AlazarTech, Pointe-Claire, QC) is employed in the system, the clock frequency is set to about 400 MHz in order to avoid overclocking of the card as well as the match the bandwidth of the dual balanced optical detector. However, as the fringe frequency is not linear, 400 MHz is actually the maximum frequency of the fringe whereas the average frequency of it is about half of that value. Therefore, with optical clocking one effectively uses about half of the imaging range can be achieved using fixed internal clocking. However, this is not a limiting factor for OCM applications as an imaging range of a few mm achievable with optical clocking is usually

sufficient. Moreover, for most of the acquisition cards it is possible to use higher clocking frequencies and overclock them.

4.4. System Synchronization

In a swept source OCT system, there are several components that need to be synchronized in order to perform a smooth acquisition. Here, an outline will be given that describes how the synchronization is achieved for the 1310 nm VCSEL OCM system. For the 1060 nm system, synchronization was already established with the turnkey operated prototype VCSEL source and the imaging engine.

To give a general overview, the electronics part of the system can be divided into several modules. One component is the light source which generates laser sweeps at a frequency set by the waveform that drives the MEMS cavity. The second component is the data acquisition card (DAQ) that performs the acquisition of the fringe samples at its internal or external clock frequency. One task for the synchronization would be to acquire a certain number of samples for each sweep of the laser, ensuring that the acquisition of each fringe starts from the same wavelength. A third component of the system is the I/0 (NI) card, which produces the waveforms to drive the scanning mirrors, as well to synchronize acquisition of each B-scan to the beginning of the fast galvo trajectory.

Figure 3 depicts the general synchronization scheme. The light source outputs a square signal (laser trigger) at its sweep frequency, which is about 280 kHz for the 1310 nm VCSEL laser when operated at resonance. This signal can be taken from the synchronization output of the waveform generator that drives the laser. Then, this laser trigger is sent to a pulse generator (TGP110, TTi), that adjust the delay of the incoming square wave in order to match the start of the sweep to the start of the A-scan, which is done by observing and centering the mirror fringes in the preview mode. For each B-scan, the NI card outputs a square wave consistent with the length of the B-scan duration, as well as a slowly rising ramp and sawtooth signals for the slow and fast scanning mirrors, respectively. This square wave is then combined with the laser trigger signal using a logical AND gate, which is then sent to the trigger input of the data acquisition card. The purpose of this step is to synchronize the start of the B-scans with the acquisition, as the card will start the acquisition of the particular B-scan after it receives the first trigger signal overlapping with the B-scan duration signal. For each rising edge of the trigger signal, the DAQ will acquire a predetermined number of points producing the fringe for that particular sweep. Moreover, the laser trigger signal is also sent to the clock input of the NI card, in order to clock the card with the exact frequency that the laser is sweeping. This step will add an extra degree of synchronization accuracy.

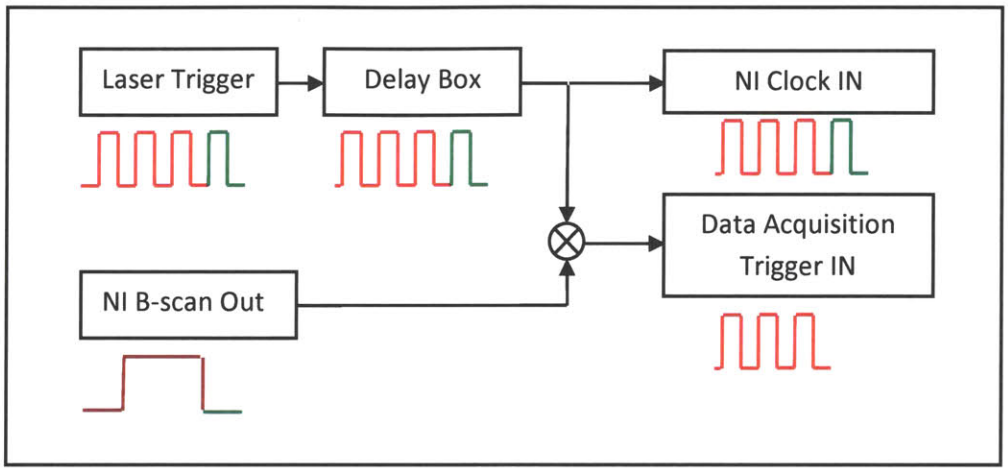

Figure 3: Schematic Representation of the System Synchronization. The high frequency square wave signal corresponds to the sweep trigger, whereas the low frequency signal corresponds to the B-scan duration signal. Acquisition will be performed for the duration of the B-scan, corresponding to the overlap between the laser trigger signal and the B-scan duration signal, shown by the red color.

The procedure described in this section ensures a synchronized acquisition. However, there are still some mechanical delays between the signal that is sent to the scanning mirrors and the actual starting time of the movement of the mirrors. This causes a few pixels of artifacts in the beginning of each B-scan, until the scanning mirrors actually start to follow the input waveform, which can be readily removed in the post processing by cropping the related portion of the image.

4.5. Signal Processing Scheme for Generating OCT and OCM Images

The processing scheme for generating cross sectional OCM images follows standard techniques described in the literature in great extend and will not be explained in detail here, however, a brief summary will be presented [2]. A general flow chart for the processing of the spectrums is given in Fig. 4.

If the spectrum is acquired without optical clocking, then the wavenumber calibration step described in Section 4.6. will be performed. Next, the background spectrum is subtracted from the acquired spectrum which is calculated by averaging the spectrums acquired when the beam is scanned off the sample. This step will remove fixed pattern noise common for the sample and reference arms. The average background can be further smoothed using a median filter and divide the background subtracted spectrums. This step will remove any residual DC

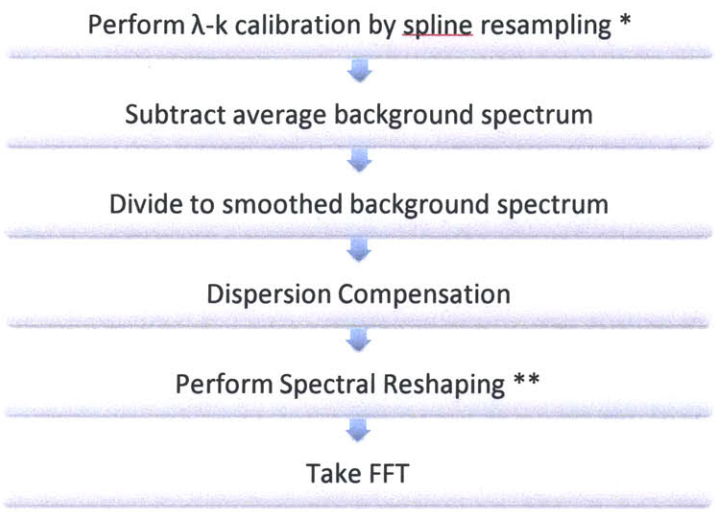

Figure 4: Processing Flow Chart to Generate OCT Images. The step denoted with * is performed only for the spectrums acquired without optical clocking.

artifacts on the spectrum caused by the imbalances of the detection. Next, the spectrums will be multiplied with a phase term to correct for dispersion. The calculation of this phase term for the dispersion is explained in detail in Section 4.6. Finally, spectrums are reshaped using a gaussian or other smoothing window, in order to reduce side lobes. Note that this step will reduce the axial resolution with a severity depending on the type and size of the selected window as can be seen in Section 4.9. Hence, it can be skipped if highest axial resolution is desired on the images. The final step consists of taking the Fourier transform of the reshaped spectrums, generating the cross sectional OCM image. Note that, depending on the sample rate and the sweep rate of the light source, the number of pixels on the acquired fringe can be small. For instance, for the optically clocked system working at 280 kHz sweep rate, there are about 357 samples on each fringe. Due to small amount of pixels in the acquired spectrums, it will be useful to zero pad the spectrums and take the FFT afterwards in order to increase the pixel density. As an example, for a total imaging range of 1.5 mm; taking a 2048 points FFT will give a pixel density of 1.5/1024 = 1.5 um/pixel on the resulting images, which is enough to have sufficiently sampled images (note that in order to be critically sampled the sampling density should be at least twice the axial resolution of the system). Table 2 summarizes the acquisition parameters for the 1060 nm and 1310 nm systems. Due to the high sampling rate of the internally clocked 1310 nm system and due to the lower sweep rate of the 1060 nm system, the number of samples in the sweeps are relatively high, relaxing the need for upsampling of the fringes.

System	Operating Mode	Sweep Frequency	Clock Frequency	Number of Samples per Sweep (single sided)
1060 nm	Optical Clock	50 kHz	~340 MHz	3400
1310 nm	Internal Clock	280 kHz	500 MHz	890
1310 nm	Optical Clock	280 kHz	~200 MHz	357

Table 2: Acquisition parameters for the 1060 nm and 1310 nm VCSEL OCM systems.

After cross sectional OCM images are generated, one can select a depth of interest and construct the *en face* OCM image from this depth. Moreover, several depths can be averaged to reduce the speckle of the images, at the expense of losing axial resolution, or projection views can be generated by finding the average, maximum intensity, minimum intensity etc. images along the entire depth. Moreover, color maps on the OCM images can be adjusted to provide a desired appearance as will be discussed in section 4.8.

4.6. Considerations for Acquisition and Calibration of the Spectrum

A major feature of most SD-OCT and SS-OCT systems is that the wavelength characteristics of the acquired spectrums are typically a function of wavelength (λ). For instance, due to the diffraction laws of light, the diffractive or reflective grating used in the spectrometer of the SD-OCT system disperses light to the detector such that pixels are equispaced in wavelength (linear in λ). Similarly, the cavity of an SS-OCM system is swept such that each consecutive sample that the detector acquires is a function of wavelength depending on the waveform that actuates the laser cavity. As it is also the case with the VCSEL sources used in this study, usually a sinusoidal waveform is employed for this purpose due to the resonant characteristics of the cavity, although there are studies that used more tailored waveforms to linearize the sweeps [3].

On the other hand, the depth information is coded into the spectrums with a linear dependence on wavenumber (linear in k). Hence, one has two ensure that the pixels of the spectrum are linearly spaced in wavenumber prior to performing the Fourier transform operation. In this project we have pursued two methods of accomplishing the task of sampling the spectrum linear in wavenumber. The first method is based on using an external Mach Zehnder interferometer (MZI) signal to acquire a fringe that has a single frequency component. This fringe is then used to calibrate subsequent spectrums that are acquired. As the second method, we will demonstrate that an optical clock derived from the MZI signal can be used instead of the internal clock of the data acquisition card, which subsequently will allow the acquisition of spectrums that are intrinsically linear in phase (wavenumber). These two methods will be compared to each other and it will be seen that optical clocking is a superior

technique for the OCM application, allowing the acquisition of spectrums in a more stable fashion.

i. Calibration Using Mach-Zehnder Traces

This method consists of acquisition of fringes using an MZI, which is guaranteed to have a single frequency component. From this MZI signal, one can extract the phase of the fringe and resample it such that the resulting resampled fringe will have linear phase. In the following more insight into this algorithm will be casted.

Since the MZI has only a single frequency component, analytical representation of the detector output is a pure phase term. Hence, for the angle of it one expects to see a well behaved monotonically and linear decreasing term as: $\measuredangle Ie^{-jk\Delta z} = -jk\Delta z$, where $Ie^{-jk\Delta z}$ is the analytical representation of the detected MZI signal, I is the envelope of the light source and Δz is the length mismatch of the MZI arms. Clearly, this behavior is valid only when the detector output is discretizated linear in wavenumber (*k*), which, as mentioned earlier, is usually not the case. As an example, Fig. 5 (A) depicts the plot of the angle of the analytic representation of an acquired MZI signal where a curvature on the phase can be observed due to nonlinear sampling of the fringe signal. Similarly the frequency chirp can be appreciated in Fig. 5 (B) due to the nonlinear behavior of the sweep. Hence the task is to resample the acquired spectrums such that the resulting analytical representation of the signal would have linear phase. In order to accomplish this, a linear fit to the original phase can be made (as shown in Fig. 5(A) and the spectrum can be resampled based on this fit. The resulting resampled spectrum will have a linear phase and uniform frequency that can be observed in Fig. 5 (A) and Fig. 5 (C), respectively.

Consequently, the method of calibration of the nonlinearly acquired spectrums using an MZI interferometer can be summarized as follows:

1. Acquire MZI signal by adjusting the path difference between two arms to an appropriate delay.
2. Calculate the analytic representation of the MZI spectrum.
3. Find the angle of the analytical representation and fit a linear curve onto it. This fit can be constructed by connecting the angle of the first and last samples with a straight line.
4. Calculate the coefficients for a cubic spline interpolator for resampling such that the analytic representation of the resampled spectrums will have linear phase (cubic spline interpolation is a good balance for the trade-off between computational speed and accuracy).
5. Use the coefficients calculated in the previous step to calibrate the subsequent spectrums acquired during the imaging session

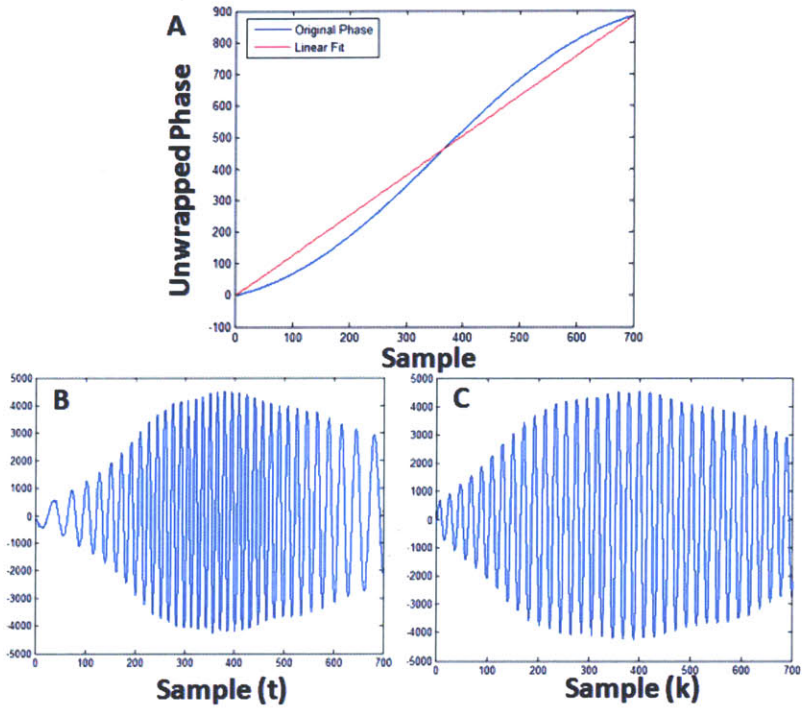

Figure 5: Phase of the analytic representation of the acquired MZI signal and linear fit (A), as well as original (B) and resampled spectrums (C). Fringes are obtained with the 1310 nm VCSEL system.

It is worth mentioning some practical considerations for the steps outlined above. First of all, the appropriate delay for the mismatch between the MZI arms should optimally be around half of the imaging range. If it is too close, then there won't be many cycles in the fringe such that an accurate determination of the phase can be made. If it is too deep, then one will start to observe nonlinearities due to the limited bandwidth of the detector.

A good way to test the fidelity of the calibration procedure is to compare the point spread function (PSF) of the resampled spectrum to the PSF obtained from the envelope of the spectrum. The envelope of the spectrum can be obtained by multiplying the spectrum with the inverse of the phase of its analytic representation. This will produce a zero phase signal (envelope), unrelated to the sampling issues and dispersion mismatches. This envelope would be the best possible PSF achievable with the system in terms of axial resolution. The task is to obtain the same PSF after wavenumber calibration. For the spectrum which is used for calibration it is expected that the PSF of the resampled spectrum and the envelope are exactly same, as it is ensured that the phase of this spectrum would be linear during the calibration process. This is indeed observed in Fig. 6 (A). Moreover, Fig. 6 (B) shows that the envelopes

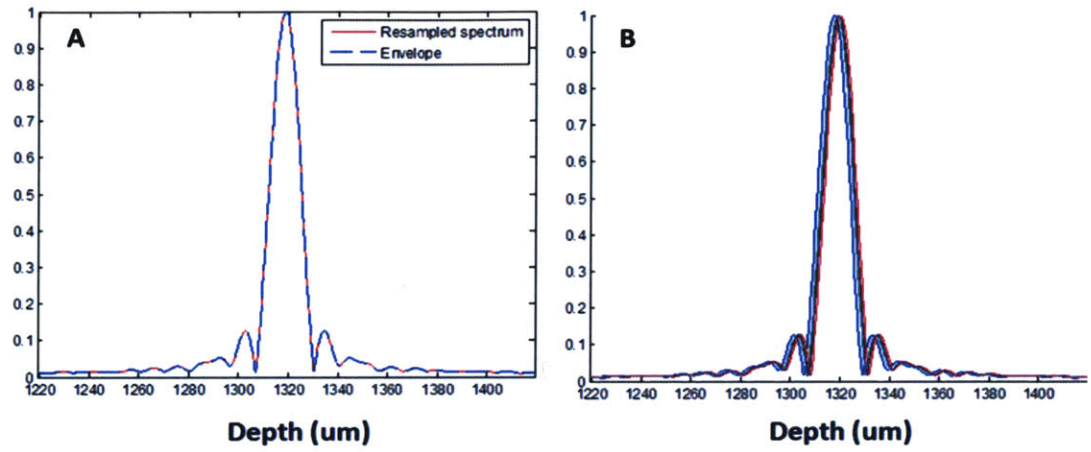

Figure 6: The PSF of envelope and the resampled spectrum for the MZI signal used for calibration (A). PSFs obtained from the envelopes of different A-scans from the same location (B). The resolution for this PSFs are about 13.2 um in air, where the 1310 nm VCSEL laser was tuned to about 100 nm bandwidth.

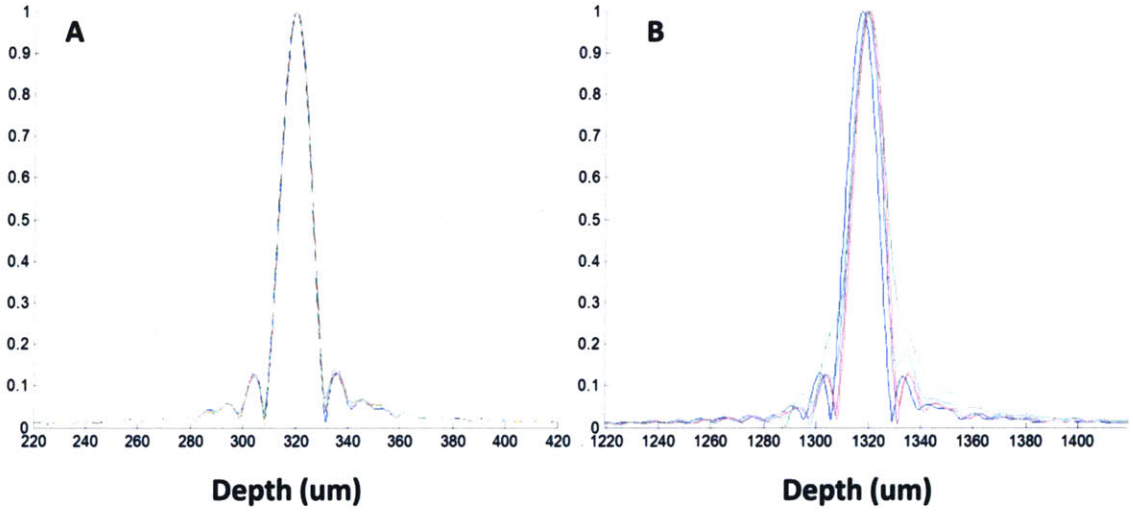

Figure 7: PSFs obtained from resampled MZI signals from two different depths (~300 um in (A) and ~1.3mm in (B)). Spectrums are obtained with the 1310 nm VCSEL system.

from different A-scans at the same depth are more or less the same, although, a few um horizontal shift is evident. Moreover, Fig. 7 depicts the PSFs acquired by moving the MZI to two different depths, where one of the spectrums at the same depth as the spectrum whose PSF is given in Fig. 7 (B) is used as the calibration. From Fig. 7 (A) it is evident that the PSFs do not vary a lot at the shallow depth ranges. However, a considerable variation of the PSFs can be observed in Fig. 7 (B), which is around the middle of the depth range of the imaging system.

This variation is linked to the fluctuation on the sweep characteristics of the light source, in which each sweep starts from a slightly different position.

A second point to consider is that, for the actual imaging arm (sample + reference arms), it is very important that the total fiber and electrical cable lengths are matched to those in the MZI arm. For the case where there are mismatches, one will see a broadened PSF, especially when the path length difference of the MZI is different from the depth where the calibration signal is acquired. Specific examples for this case will be given in the discussion for optical clocking. One factor that complicates this issue is that a mismatch in the dispersion of the sample and reference arms deteriorates the PSFs in a way similar to a mismatch in the cable lengths of the imaging and MZI arms, and it is hard to decouple these two phenomena. Hence a recommended procedure for matching the cable lengths of MZI and imaging arms can be given as following:

1. Construct a sample and reference arm that does not have any elements in its path, and measure the total fiber length in each arm to make sure that they are matched. This will ensure that the dispersion in the sample and reference arms is matched.
2. Vary the optical and electrical cable lengths until the resampled PSFs are matched to the PSFs obtained from the envelope at different depths. This way it is ensured that the cabling lengths are matched between the imaging and MZI arms.
3. Switch to actual sample arm by inserting back the optics.
4. Match the dispersion of the system by putting glass to the reference arm until the dispersion is matched between two arms. Again, the matching of the dispersion can be determined by comparing the PSF of the resampled spectrum to the PSF of the envelope. This way it is ensured that the dispersion of the system is compensated as well.

When performing the steps outlined above, it is important that the fringe signal is acquired close to the middle of the imaging range, since mismatches in the dispersion and cable lengths make less effect for shallow depths as shown in Fig. 7 (A).

ii. Uniform Wavenumber Sampling with Optical Clocking

Although the wavenumber calibration using MZI traces works to some extent, it has several disadvantages as shown in the previous section, mainly due to the variations in the sweeping behavior of the light source. Note that, if the VCSEL source was run off-resonance in order to increase its sweep rate, then it is expected for these variations to become even worse. One possible method to overcome this issue is to simultaneously acquire MZI signals during imaging, such that one has a corresponding MZI calibration trace for each A-line. However, this adds

remarkable computational complexity to processing as one needs to calculate the resampling coefficients for each individual A-line.

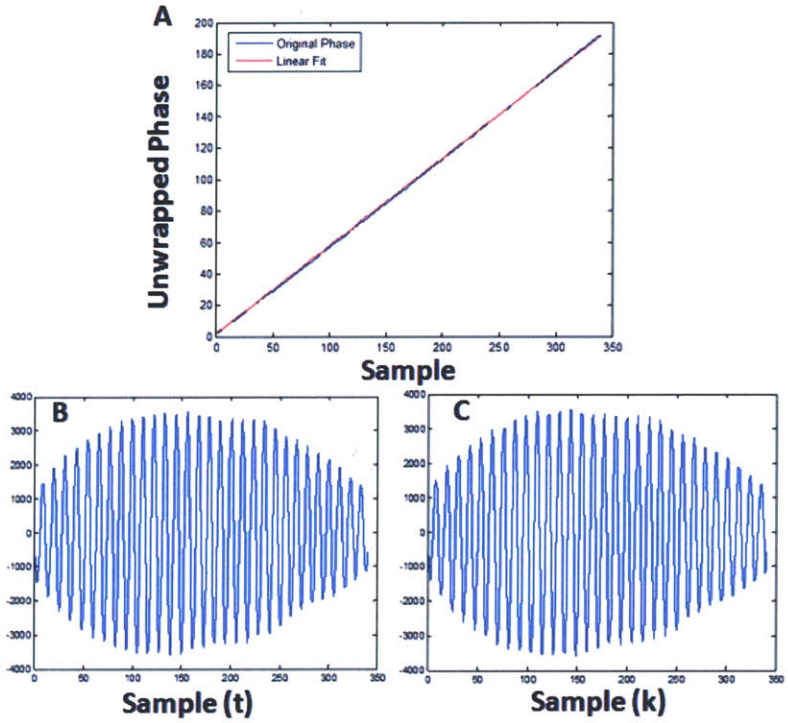

Figure 8: Phase of the analytic representation of the fringe, acquired with optical clocking, and linear fit (A), as well as original (B) and resampled spectrums (C). Fringes are obtained with the 1310 nm VCSEL system.

An alternative method is to sample the spectrums linear in wavenumber to begin with. This can be achieved by clocking the data acquisition card such that it acquires one sample at each zero crossing of the MZI signal. Since the MZI signal is already a function of k , picking a sample at each zero crossing will guarantee a sampling linear in k. This method is commonly called as optical clocking, and has been to proven to increase the computational speed by a factor of 2 to 10, as it circumvents the need for wavenumber calibration and oversampling of the spectrum [4].

As shown in Fig. 8 (A), the phase of the spectrum acquired using a mirror as the sample with the optically clocked system shows a linear behavior, as well as no frequency chirp is observed if Fig. 8 (B). For comparison purposes with Fig. 5, a linear fit is made to this spectrum and spectral resampling is performed as previously described. As shown in Fig. 8 (B) and (C), original and resampled spectrums are almost identical, proving that optical clocking indeed ensures linear sampling of the spectrums.

For this project, optical clocking has been tested for the VCSEL source using a 500 MHz Alazar data acquisition card (AlazarTech, Pointe-Claire, QC), and is confirmed to work more reliably compared to the previous method of using single MZI trace for the calibration. To maximize the portion of the MZI fringe used for clocking, a clocking circuit is used that converts the sinusoidal MZI trace to a uniform amplitude square clock signal.

Figure 9 (A) shows an example of PSF found by taking directly the FFT of the acquired spectrum compared to the PSF obtained from the envelope. A good agreement can be observed between the two PSFs in terms of the FWHM and level of the side lobes. Notice that, by adjusting the dispersion numerically, this PSF can be matched exactly to the PSF of the envelope. Figure 9 (B) and (C) shows PSFs of the envelope and original spectrum, respectively, for different A-scans. Comparing these plots to Fig. 7, one can appreciate the stability of the spectrums with optical clocking due to the insensitivity of this technique to the drifts and variations in the sweeps characteristics of the light source.

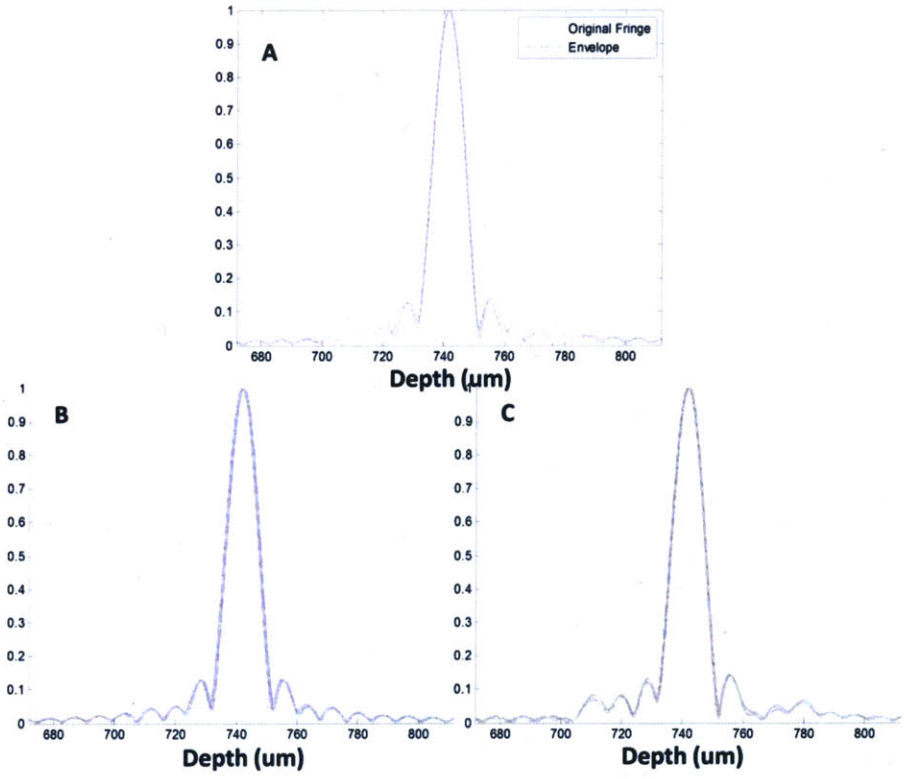

Figure 9: PSFs obtained from the envelope and the raw spectrums acquired by the optically clocked 1310 nm system proving the robustness of the acquisition scheme to the variations of the sweep behavior of the light source. PSFs obtained from envelopes (B) and raw spectrums (C) of different A-scans from the same location. (A) shows an overlap between these two PSFs. System tuned close to its full 120 nm tuning range. Resolution measured as 11.6 um in air.

As it is case for the calibration with MZI traces, for optical clocking it is also important to match the cable lengths of the imaging arm and the MZI arm. To decouple cabling length from dispersion, a similar procedure outlined in the previous section can be used. Again, it should be kept in mind that the PSFs will be relatively insensitive to the variations of the cable lengths for shallow depths. An example for this can be seen in Fig. 10, where the arm lengths are mismatched by about 2 meters. For Fig. 10 (A), although some asymmetry in the PSF can be observed, the resolution is still about the same as what was observed in Fig. 9. However, for the PSF in Fig. 10 (B), which is taken from a longer delay, the broadening of the PSF is clearly evident. Hence, it is important to perform dispersion compensation and cable length matching for a long delay between the sample and reference arms, typically around the middle of the imaging range.

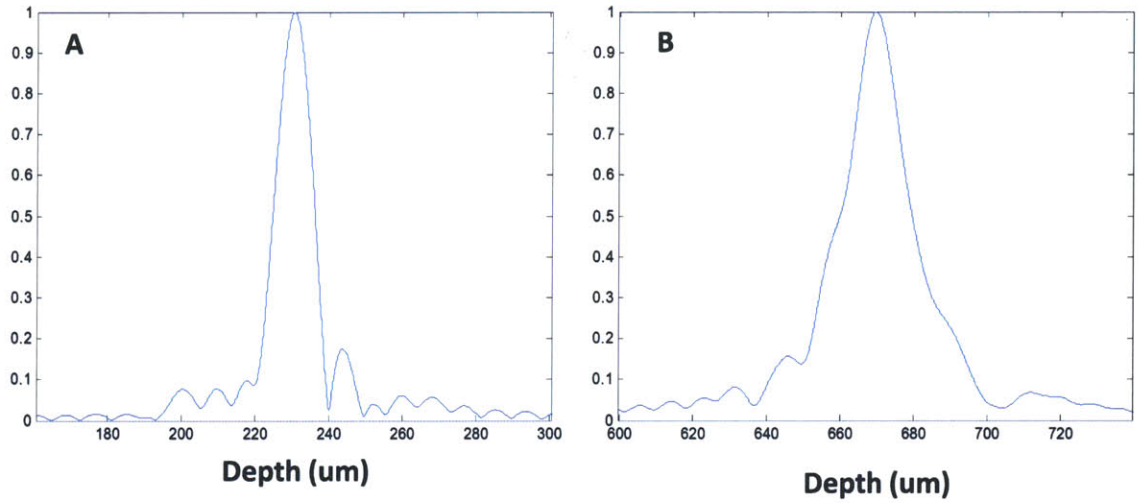

Figure 10: Effect of cable length mismatch on the PSFs from two different depths. Fringes are obtained with the 1310 nm VCSEL system.

As a final point, if the cable lengths and dispersion of the system is perfectly matched, then one expects to observe uniform resolution throughout the imaging range. However, usually it is not possible to perform this degree of optimization due to the coupled nature of the dispersion and cable lengths. However, it is still possible to compensate residual phase variations numerically. For this, one can find the nonlinearity of the phase for a mirror interference signal, and then use this phase to compensate for the phase nonlinearity of other spectrums. Table 3 shows the axial resolutions of the optically clocked system for different reference delays. In the first column a total of 1.6 um variation can be observed for the imaging range when no numerical compensation is performed. For the second column, on the other hand, the phase from the fringe at 350 um is used and the total variation is reduced to 1.2 um. Notice that, the resolution progressively gets worse when the delay is further from the point of calibration. For the last column of Table 3, the phase of the mirror near to the middle of the

imaging range is used and one observes a variation less than 0.8 um for the imaging range. Hence, a good choice for the mirror signal for its phase to be used for the calibration would be to choose around the middle of the imaging range or around a depth where the sample is expected to occupy.

	Axial Resolution in Air (um)		
Depth (um)	No dispersion compensation	Using phase from 350 um	Using phase from 630 um
210	13.27	11.48	12.35
350	12.44	11.40	11.93
490	11.75	11.66	11.66
630	11.75	11.76	11.66
770	11.66	12.44	11.66
910	11.75	12.99	11.93
1050	11.61	12.71	11.61

Table 3: Axial resolutions (in air) for the optically clocked 1310 nm system at 120 nm tuning range from different depths.

4.7. Generation of Large Field Images via Mosaic Imaging

Undoubtedly a major constraint of a high magnification imaging system is the limited field of view (FOV). A method to overcome this limitation which is used in many clinical settings, such as pathology, is to initially survey the specimen with a low magnification objective, then zoom into region of interests by switching the objective with a higher power one using a turret. However, there are cases when one wants to obtain high resolution images from the entire surface of the specimen. As an example, for digitization of histology slides, one needs image the slides in its entirety with high resolution. Another example would be that if one wants one to one correspondence of the OCM images with the histology, then he will also be required to image the whole specimen with a high power objective. Furthermore, in a clinical scenario where the sample needs to be imaged in real time due to the integrity of the specimen, but it will be interpreted at a later session, then it will be necessary to obtain images of the whole specimen with a high resolution objective.

A method to overcome the field of view limitation of the OCM imaging system is to acquire a number of small field images from different regions of the sample, and then combine these images to generate a large field stitched image. Fortunately, this is a well known and well studied research problem especially in the image processing community, and there are many methods and algorithms that are developed in order construct seamless composite images by combining individual frames [4]. Among many software that are developed to accomplish this task, it is found that Image Composite Editor (ICE), which is a closed source but freeware program from Microsoft, provides a reliable and robust environment for generating large field

stitched images. After the stitching is completed, images can be converted to a deep zoom format which produces a hierarchical format with different magnification levels. This format can be opened using the HD View program from Microsoft which seamlessly allows user to pan around the images and to zoom to regions of interests producing the native high resolution view. Furthermore, the HD View program is integrated with the browsers allowing the user to send the internet links of the stitched dataset or the specific views to satellite places, eliminating the need for physically transporting large amount of data.

Figure 11 shows a demonstration of combining four small field images to generate a large field mosaic image. The field of view for each image is about 500 um, and images are acquired with a 50% percent overlap. Hence, the composite image has a total of 750 um by 750 um field. Using an automated stage is it possible to acquire larger total fields, whose examples will be presented later in the thesis. For generating the mosaic images, ICE performs a two step process consisting of (1) alignment of frames within each other based on image features, and (2) composition of the large field mosaic image by using several image blending algorithms such as graph-cut optimization and gradient domain image-fusion algorithm, which accounts for possible intensity and rotational variations between the overlapping fields [5, 6]. Note that the images in Fig. 11 are acquired with a 50% overlap in order to ensure a seamless stitching by providing more corresponding features between frames, however, if the contrast is high enough then it is possible to have smaller overlap between the fields, which will decrease the time required for the acquisition of the total field.

One major disadvantage of the acquisition of individual small field images is the long time required for the total acquisition process. Here the limitation comes from the mechanical movement of the translation stages, which has to perform a discrete movement after acquisition of each individual frame. Especially if multiple depths are to be acquired by translating the focus, then the total acquisition time can easily span 20-30 minutes, which is impractical for a clinical setting. An alternative for acquiring individual square fields is to obtain long strip images by disabling one of the scanning mirrors and continuously translating the stage in the slow direction while acquiring the image [7]. Since the stage will only step after the acquisition of one strip is finished, the imaging speed will be roughly limited by the scan rate of the imaging system or the maximum frequency of the fast scanning mirror. In this setting, the fast scanning mirror can be replaced by a resonant scanner to further improve the imaging speed.

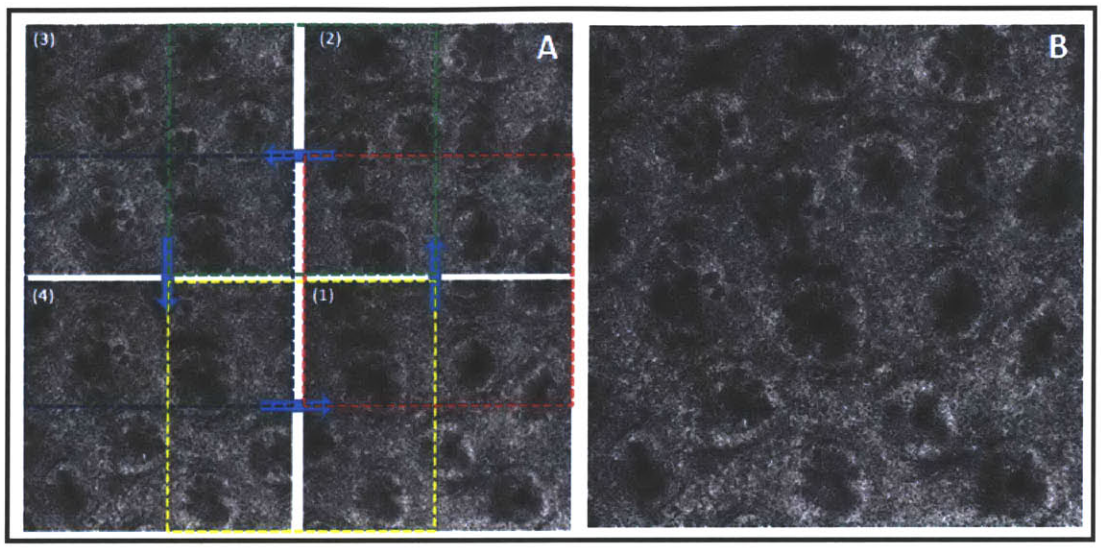

Figure 11: Demonstration of large field of view generation by acquiring overlapping small field images. Smaller field images are shown in (A). Arrows point to the direction of the stage motion and dashed boxes show the overlapping regions. Resulting mosaic image is shown in (B).

In addition to improving the imaging speed, strip imaging also has the advantage of reducing the artifacts due to scan field and illumination non-uniformities, as the image of the single scanning mirror can be placed directly to the back focal plane of the objective, which will produce a flat scan field. One disadvantage, however, is that even for a very precise translation stage, the motion parameters such as acceleration or the value of constant velocity is not precisely same for a series of movements. Hence, due to these variations in the motion of the stage it will be challenging to acquire the image of the same strip twice if one wants to acquire and average several strip images. If averaging is not necessary, however, then strip imaging is a good alternative to imaging smaller square fields. Initial tests demonstrated at least an order of magnitude increase in the acquisition speed compared to the latter technique.

4.8. Image Processing and Display

i. Field Curvature Correction

In order to provide the compactness necessary for the OCM system to be put into a pathology laboratory or an endoscopy suite, a non-telecentric sample arm design is employed as described in Section 4.1. However, this comes at a cost of curvatures in the scan field, as the back focal plane of the objective can not be imaged simultaneously to both of the scanning mirrors. Figure 12 depicts an example of this phenomenon, where a mirror is used as the sample. Figure 12 (A) and (B) are the cross sectional images generated by scanning the fast (X) and slow (Y) scanning mirrors, respectively. From these two figures it can be seen that the

curvature is concave in one case, and convex in the other case, which shows that the back focal plane of the objective is imaged in between the two scanning mirrors. Figure 12 (C) shows the *en face* projection image generated from the mirror. It can be seen that the brightness of the mirror reflection is highest at the center of the field, which extinguishes when approaching to the edges of the scan field.

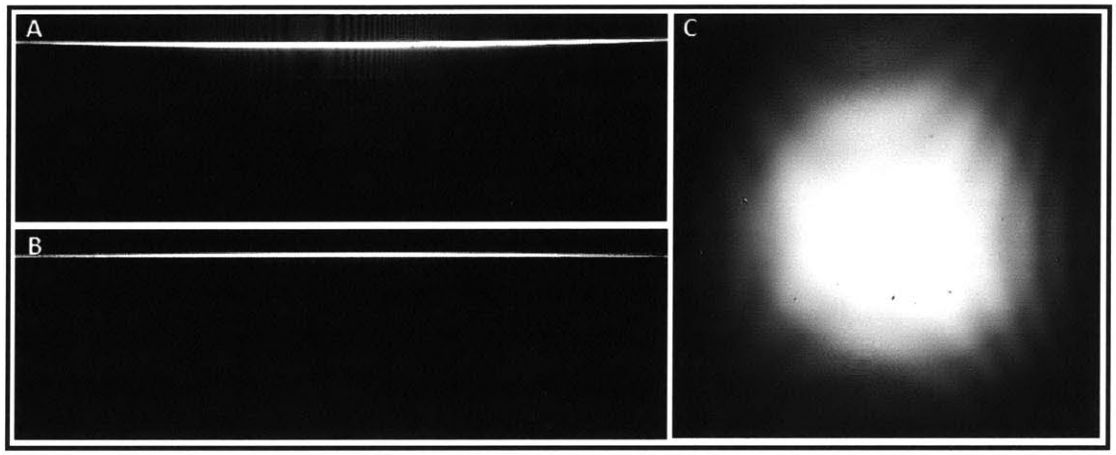

Figure 12: Scan field curvature due to non-telecentric scan of the beam. Images are obtained by the 1060 nm OCM system using the 40X objective. (A) and (B) show cross sectional images from two orthogonal directions whereas (C) shows the corresponding *en face* projection.

Note that, the field curvature depicted in Fig. 12 is particularly deleterious for a TD-OCM system, as the fixed reference arm delay determines the depth of the image that will be acquired. Moreover, if a high NA objective needs to be employed in the system in order to generate simultaneous two-photon or second harmonic generation images, then the confocal range will also be limited. Therefore, the curvature has to be less than the confocal range and the confocal and coherence gates matched to each other, in order for the TD-OCM image to be generated. Hence, one has to limit the field of view to the extend that the curvature in the scan field is sufficiently small. In a study by Tang et al., featuring multimodal time TD-OCM and MPM, the FOV was limited to as low as 20 um x 20 um due to this constraint [8].

However, due to major advantage of Fourier domain imaging methods which provide depth resolved images, one can still recover images from the whole FOV even when the scan field is curved. For this purpose, one can use either a mirror reflection similar to the one depicted in Fig. 12, or if the sample is imaged using a cover slip then it would be better use the reflection from the second surface of the cover slip which is in contact with the tissue. Then, this image can be used as a reference field for the calibration of the field curvature, which can be accomplished by circularly shifting individual A-lines according to the distance between the location of the calibration field for that particular A-line and the location of the calibration at the center of the image. Hence the procedure for the correction of the scan field curvature

would be to segment the mirror or the cover slip reflection for each frame, then apply a smoothing filter or a polynomial fit to construct the three dimensional surface profile. Finally, this profile is used to circularly shift each individual A-line in the image.

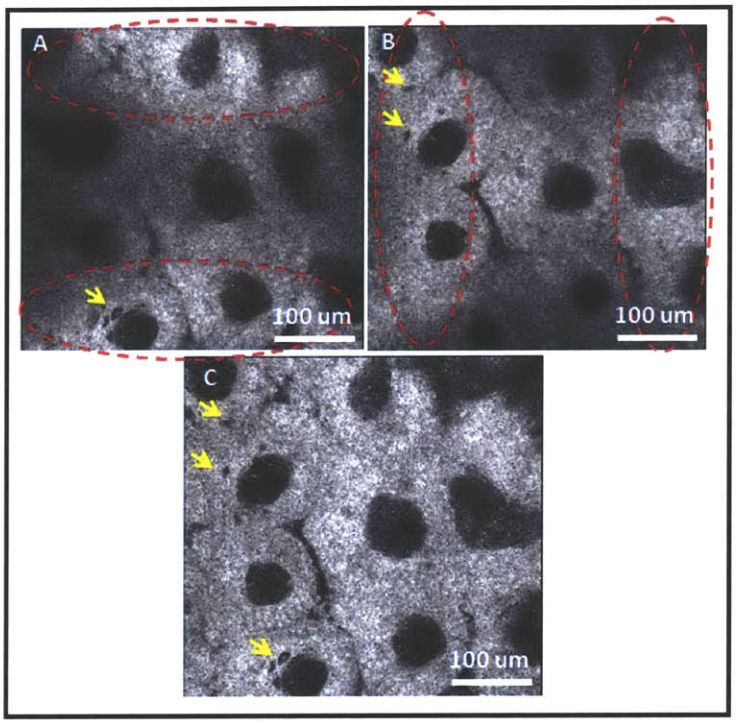

Figure 13: Correction of scan field curvature demonstrated by *ex vivo* human colon images obtained by the 1060 nm OCM system using the 40X objective. (A) and (B) are from two different depths from the same dataset, where (C) is the calibrated image. Dashed lines indicate the regions that are in focus for that particular depth. Arrows point to goblet cells.

Figure 13 demonstrates an example for the impact of the scan field curvature on the images generated from *ex vivo* human colon sample using the 40X Olympus objective. Note that, in Fig. 13 (A) and (B), which are selected from two different depths of the same dataset (~40 um apart), different portions of the image are in focus. This can be clearly seen by the visualization of goblet cells at the regions where the sample in focus. By following the procedure outlined in the previous paragraph, the image shown in Fig. 13 (C) is generated which shows uniform resolution throughout the field of view. Notice that the goblet cells are now visible in both of the regions highlighted in Fig. 13 (A) and (B).

Note that circular shifting of A-lines can be thought as multiplying the A-lines with a linear phase. Hence, in order to gain computational speed, one can also compensate the dispersion in this step by integrating the dispersion to the phase that will shift the A-line. This technique of compensating scan field curvatures while simultaneously compensating for the dispersion has been demonstrated in several studies [9, 10]. Another point to mention is that, this method

assumes that the focus will maintain the same curvature when the beam is propagating inside the sample. However, due to aberrations caused by the scattering inside the sample, the shape of the curvature might also change when the focus is deep inside the sample. If a high NA objective is used for imaging, then one can find the actual focal curvature inside the sample as the cross sectional image will be in the form of a bright stripe corresponding to the focal plane [11, 12]. In this case a sharpness or maximum intensity metric can be used to segment the actual focal curvature of the beam inside the sample, and use this as the calibration field. However, the field curvature can be observed even for the lower power objectives, such as the 10X and 20X objective where the focal plane can not be estimated precisely from the cross sectional images. In that case it will be more appropriate to estimate the scan field curvature from the mirror or cover slip reflection.

ii. Imaging with Low Power Objective and Surface Flattening

Usually a microscope cover slip (with a thickness around 0.16 - 0.2 mm) is used for microscopy imaging systems in order to ensure a flat imaging surface, as depth variations can be detrimental if the depth of focus of the objective is very short. For imaging systems such as multiphoton imaging, confocal imaging and TD-OCT, this is especially important as imaging is limited to the very superficial layers or, for the case of TD-OCT, the reference arm length must be matched to the confocal range.

When a low power objective with a long depth of focus is used for imaging, such as the 10X Zeiss objective employed in this study, on other hand, the use of cover slip can cause some undesired artifacts, as the reflection from the surfaces of the cover slips can overwhelm the signal originating from the sample by increasing the noise floor of the fringes. An example for this phenomenon is given in Fig. 14. Figure 14 (A) demonstrates a cross sectional image of an *ex vivo* human colon sample taken with a 10X objective using a cover slip. The focus is set about 60 um below the second surface of the cover slip and the depth of focus is calculated to be about 50 um for this configuration. There is a bright reflection from the second surface of the cover slip which also produces the horizontal bright lines seen in the image. A zoomed view around this region is shown if Fig. 14 (B), where these horizontal artifact lines can be observed upto 100 - 150 um below the second reflecting surface of the cover slip. Figure 14 (C) shows the *en face* reconstruction below ~40 um of the second surface of the cover slip, where the brightness caused by the reflection from the cover slip overwhelms the actual image. Figure 14 (D), on the other hand, is taken about ~60 um below the second surface and the crypt structure of the colon can still be discerned. Hence, it can be inferred that when imaging is performed with a low NA objective, cover slip causes imaging artifacts due to high reflections from its surfaces, upto an imaging depth which is related to the depth of focus of the imaging configuration.

On the other hand, the relatively high depth of focus of the low power objective makes it less critical for the imaging to be performed on a flat field; hence the use of a cover slip might not be necessary for this case. However, if the sample is tilted too much or has some topographical properties, such as protrusions or dips, then one can see structural variations along the *en face* imaging plane. This is demonstrated in Fig. 15, taken from a fixed *ex vivo* human colon sample using the 10X objective, without the usage of cover slip. Especially in Fig. 15 (B), one can appreciate the degree of tilt that is present in the image. The *en face* reconstruction in Fig. 15 (C) clearly shows the variations on the structural features along the image. The beginning portion of the image shows superficial layers whereas towards the end, the imaging plane gets deeper and one can see the crypt architecture.

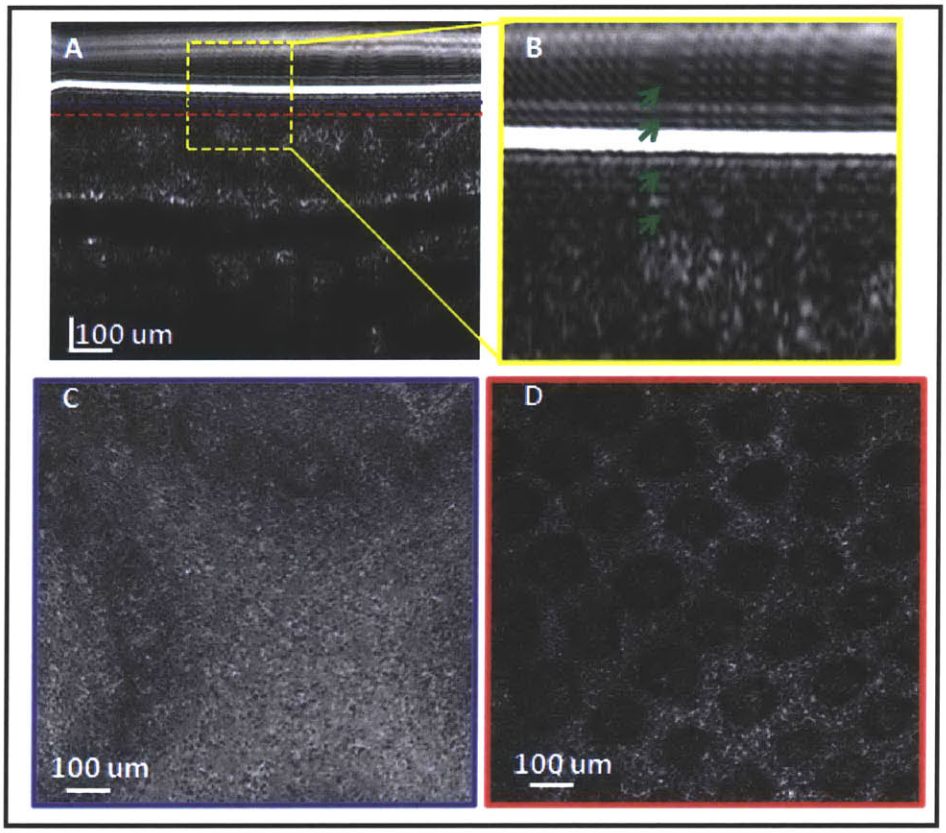

Figure 14: Cross sectional (A,B) and *en face* images (C,D) of an *ex vivo* colon sample taken with a 10X objective using a cover slip. (C) is from ~40 um below the second surface of the cover slip, whereas (D) is from ~60 um below that surface. Green arrows in (B) point to some of the horizontal artifacts caused by the reflection from the second surface of the cover slip. Images are taken using the 1310 nm OCM system.

A straightforward method to compensate for the topographical variations seen in Fig. 15 is to detect the surface of the specimens from cross sectional images, then shift the images of the individual A-lines according to its distance from a pre-determined center, which will ensure

a flat surface. A similar procedure outlined in the previous endoscopic OCT studies is followed to accomplish this task [13]. This algorithm operates on each cross sectional image to segment its surface. Briefly, a gaussian and median filter is applied to the frames in order to reduce the speckle noise. Then, the frames are thresholded in order to remove the noise especially above the surface portion of the image. Note that a relatively high threshold can be chosen here as the reflection from the surface is expected to be quite high. Afterwards, a Canny filter is applied that detect the edges in the image. Surface then can be detected by finding the first non zero elements in each A-line. The final step is to apply another median filter to the array of edge locations for that individual frame, in order to remove outliers in the detected edge and ensure a smooth surface profile. Once the surfaces are detected on each cross sectional frame, one can circularly shift the A-lines according to the distance between the location of the detected surface of that A-line and a pre-determined center depth, similar to the correction of the scan field curvature described in the previous section. Using this method a flat surface will be ensured at that pre-determined center.

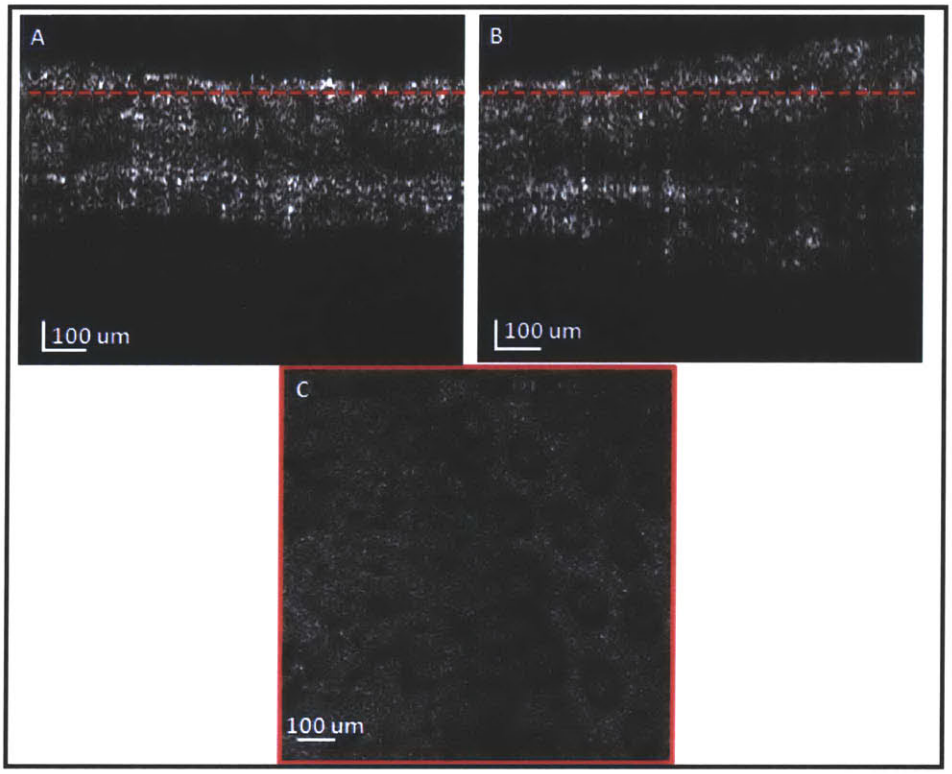

Figure 15: Imaging without using the cover slip using the low power (10X Zeiss) objective. Cross sectional images from XZ (A) and YZ (B) directions and *en face* reconstruction (C) along the depth shown by the dashed line. Images are taken using the 1310 nm OCM system.

Figure 16 shows the cross sectional and *en face* images after the surface flattening algorithm is performed. Comparing Fig. 16 (B) to Fig. 15 (B) one can appreciate the success of the flattening in the cross sectional image. Moreover, as can be seen from the *en face*

reconstruction depicted in Fig. 16 (C) and Fig. 16 (D), which are selected from two different depths, uniform structural information is present throughout the image, as opposed to Fig. 15 (C), where the two features seen in these images are mixed along the imaging plane. Notice that although surface can be flattened in post processing, the degree of tilt still should be small enough such that the features of interest remain inside the focal range for the cross sectional images. Hence the utility of this approach will be limited for low power objectives with a large depth of field, or for the samples that have limited tilt or topographical variations.

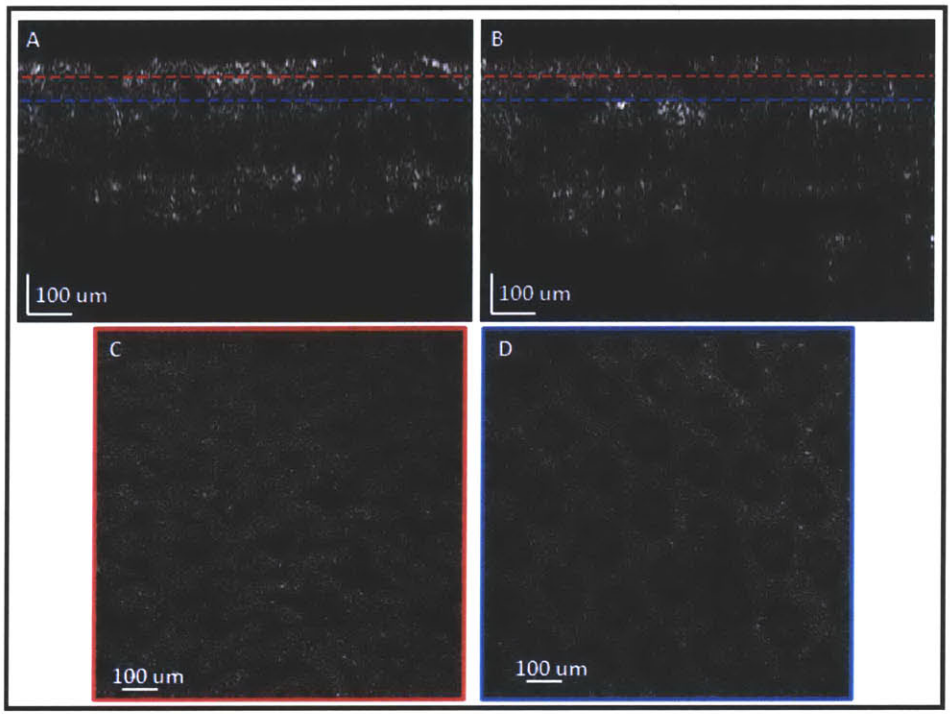

Figure 16: Cross sectional (A,B) and *en face* (C,D) images after surface is flattened. Dashed lines in the cross sectional images indicate the location selected for the *en face* plane. Images are taken using the 1310 nm OCM system.

iii. Color Maps for *en face* Display

The final step in the SS-OCM processing is to select several depths of interest from the volumetric dataset, and then to construct and display the *en face* images corresponding to the selected depths. Traditionally OCT images are displayed in a logarithmic scale, where the logarithm of the intensity images are taken and scaled to a bit depth of 16 bits after applying a threshold to crop the noise level and high intensity reflections. Taking the logarithm essentially compresses the dynamic range of the intensity image, which is necessary for cross sectional OCT images as there is a large variation of the signal intensity across different depths of the image. However, for *en face* images that corresponds to a specific depth, the signal variation is not as high as it is in the cross sectional images. Therefore, logarithmic compression might be

an overshoot for displaying OCM images. The uncompressed images, on the other hand, might still have too much intensity variation across the image where high intensity areas might appear as saturated and obstruct the delineation of fine structures. Consequently, a square root compression is considered as a good trade off for the display of OCM images, which balances the intensity saturation and the visualization of fine details in the images [14].

Another consideration for the visualization of the OCM images is the selection of a suitable color map. OCT and OCM imaging has single contrast generating channel (intensity image), which suits the usage of a single color display such as grayscale. Direct conversion of the images to grayscale dictates that the areas with high intensity appear as white, whereas the areas with low intensity appear with the tones of gray and black. This convention is commonly used in displaying confocal images, which has a similar contrast mechanism as OCM. However, in some of the OCM studies a negative color scale is chosen instead, in which the regions with high intensity appear with dark colors [15-17]. This display has the property that the areas with low signal are white, which gives a closer appearance to standard histology, hemalum and eosin (H&E) images, and therefore, might facilitate for a pathologist to interpret the images.

Another choice for display is the use of pseudocolor maps. Especially in the field of ultrasonography the use of false colors as opposed to grayscale display has been shown to increase the sensitivity and specifity of the radiological readings [18, 19]. Therefore, some of the commercial OCT imaging devices uses similar pseudocolor display conventions. Pseudocolor maps can be chosen either single color, or alternatively a range of colors can be used to divide the color scale. Recently, several confocal imaging studies have employed this approach to convert grayscale images into RGB colors which mimics H&E color scale [20, 21]. Note that in the H&E stain used in conventional histology, hemalum colors the nucleus of the cell in varying shades of blue depending on the concentration and composition the of nuclear material inside the cell. The second component eosin, on the other hand, colors cytoplasmic structures in various shades of red, pink and orange. These cytoplasmic structures include cytoplasm of individual the cells as well as the surrounding connective tissues and other extracellular substances. Consequently in these confocal imaging studies, an external contrast agent, acridine orange, has been used which bonds to the nuclear content inside the cells, generating fluorescence signal originating from the nuclei of the cells [20, 21]. Reflectance confocal or fluorescence images arising from fluorescein, on the other hand, highlight extracellular space and show nuclei as dark spots. These two different contrast channels then converted into a color scale such that the image showing acridine contrast appears in the shades of blue and the standard confocal image appears in the shades of pink and red.

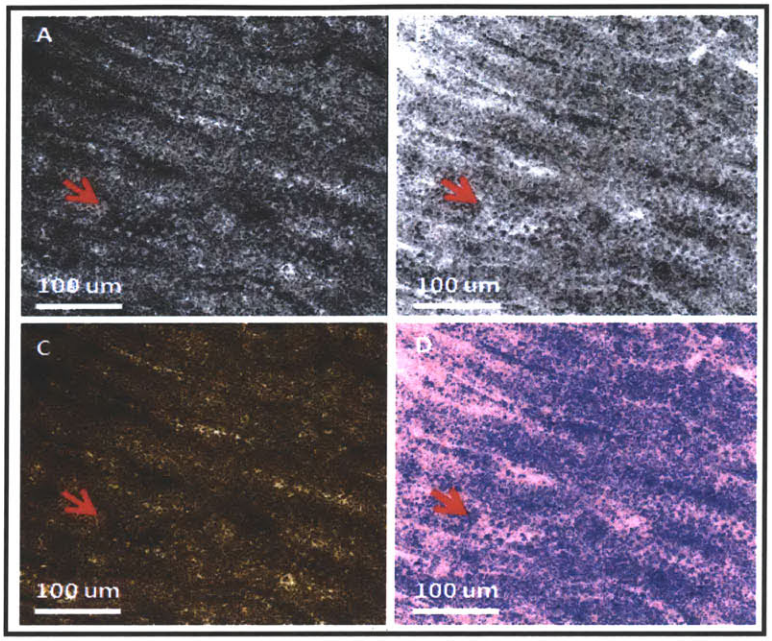

Figure 17: Illustration of regular grayscale color map (A), inverse color scale (B), false color sepia color map (C), and false color H&E mimicking color map (D) on the images of *ex vivo* fresh rabbit kidney specimen. Arrows point to areas showing cellular structures. Imaging is performed with the 1060 nm OCM system using the 40X Olympus objective.

Figure 17 illustrates some of the color scale concepts discussed in this section. *Ex vivo* images taken from renal medulla of a rabbit has been chosen which have well defined cellular features as pointed by the arrows in the images. When comparing Fig. 17 (A) and (B), it can be observed that the cellular features can be selected more easily from the inverse color scale image, whereas the overall shape of the collecting tubules are more easily discerned in the regular grayscale color map. Fig. 17 (C) displays a sepia color map which is typically used in ultrasound images. Finally Fig. 17 (D) displays a false color H&E color map. Note that, as opposed to the confocal imaging studies discussed previously, OCT does not have a dual channel contrast mechanism separating nuclei from extracellular substances. However, it has been suggested that the back scattering from nuclei of the cells dominates the back scattered signal [22]. Therefore, as done in Fig. 17 (D), by assigning the values of high intensity to the tones of blue and the values of lower intensity to the tones of red and pink, it might be also possible to enhance the nuclear contrast in the OCM images.

To summarize, in this section it has been seen that there are many possible choices of color scales that can be used to display *en face* OCM images. For majority of the images included in this thesis standard grayscale color map has been applied without loss of generality. However, the choice of color scale for a clinical scenario will be application dependent. For certain OCT applications, such as endoscopic or cardiovascular imaging the choice of sepia color map can be justified as the competitive imaging modality, ultrasound, has been used for a

longer time, and the radiologists or endoscopists might have more intuition in reading images with this color map. For OCM applications, on the other hand, grayscale color map might be a suitable choice especially for the applications that are in competition with confocal imaging. The false H&E color scale can also be appealing to pathologist as it resembles to histology more closely. However, it should be noted that not all applications will have clear nuclear structures as the images as shown in Fig. 17. For lower GI or breast images that will be shown later in Section 5.1., nuclear details are not as easily discernible. Therefore, the utility of this color map for those applications is not clear. As done by the ultrasound imaging studies, the ultimate test for choosing the optimum color map would be to perform blinded readings for images with different color maps and selecting the color map that has the highest diagnostic accuracy [19].

4.9. System Characterization

This section will summarize several parameters that have been measured to assess the performance of the OCM setup, for both the 1060 nm and the 1310 nm VCSEL OCM systems.

The 1060 nm VCSEL system operated at a 100 kHz A-scan rate and give an output light centered around 1060 nm with 80 nm tuning range. The output power of the light source is ~15 mW, whereas the collimated power in the sample arm is around 8.6 mW. The power onto sample is around 3.1 mW with the 40X Olympus objective, causing a total throughput of 36% for the sample arm. Note that, as previously mentioned, the low efficiency of the objectives around IR wavelengths is the main cause for the low throughput of the system. As for the 1310 nm VCSEL system, the operating frequency is set to 280 kHz, which causes an effective A-scan rate of 560 kHz. The output light is centered around 1310 nm, with a full tuning range of 120 nm. The output power of the laser is around 30 mW, and the collimated power on the sample arm is around 14.7 mW. The power onto sample is around 5 mW with the 40X Olympus objective, causing a throughput of 35%. The throughput with the Zeiss objectives is about 45%.

The axial resolution for the 1060 nm system is measured to be around 12.9 um when the full tuning range was used. However, for this configuration the system is not working stable probably because the lower ends of the sweep range is causing triggering issues. Hence the tuning range is decreased in the software and an axial resolution of 13.6 um is used for the imaging. For the optically clocked 1310 nm VCSEL system the axial resolution is measured as 11.4 um, when the full tuning range was used. Figure 18 (A) shows the PSFs of the original spectrum. Note that in order to numerically compensate the dispersion, spectrum is multiplied by the inverse of its phase, as described in Section 4.6. Note that due to the sharp edges of the VCSEL spectrum, the sidelobes of the PSFs are relatively high. In order to reduce the sidelobes, a smoothing window can be applied to the spectrums. Figure 18 shows the PSFs resulting from three different choices of windows. Note that the improvement in the side lobes comes with a

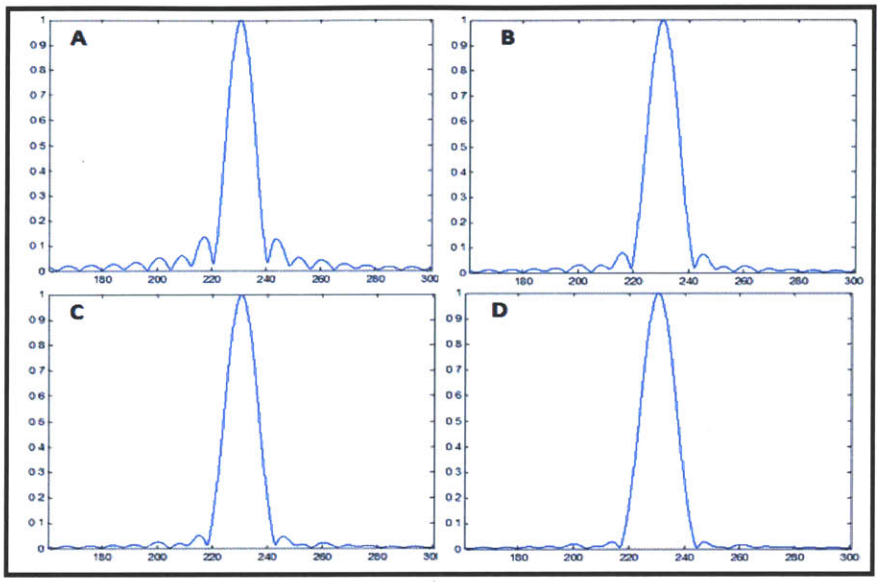

Figure 18: Axial PSFs of 1310 nm VCSEL OCM system. Original PSF (A), and PSFs from the spectrums that are reshaped using a Kaiser window (B), broad Gaussian window (C) and narrow Gaussian window (D). Axial resolutions are measured as 11.4 um, 12.5 um, 13.1 um and 14 um for (A-D), respectively. Resolution values are in air.

penalty on the axial resolution. For the majority of the images shown in this thesis either no window is applied to the spectrums or a broad Gaussian window is applied which caused < 1 um of loss in the axial resolution. Note that the axial resolution values reported here are measured in air, hence they need to be divided to a factor of 1.39 – 1.44 in order to convert them to the resolution values in the tissue. When this conversion is performed, the axial resolution of the optically clocked 1310 nm system is calculated as 8.14 um.

Figure 19 shows PSFs obtained by translating the reference arm to various depths throughout the imaging range. The intensity signal is plotted on a logarithmic scale where it is linearized by the highest intensity among the PSFs. A uniform intensity can be observed throughout the imaging range of the system proving the long coherence length of the VCSEL source. Note that, especially for spectral OCT systems a 6 dB drop is usually observed at half of the imaging range which degrades the image quality at deeper regions of the sample. As a side note, since the MZI signal employed for optical clocking had a maximum of 400 MHz signal component, which falls well within the bandwidth of the balanced detector as well as the DAQ, no additional roll-off is observed due to the nonlinearity of these detection devices at higher frequencies. Hence, if an MZI signal with higher frequency were used to clock the DAQ, then a residual roll-off is expected to occur especially at higher imaging depths.

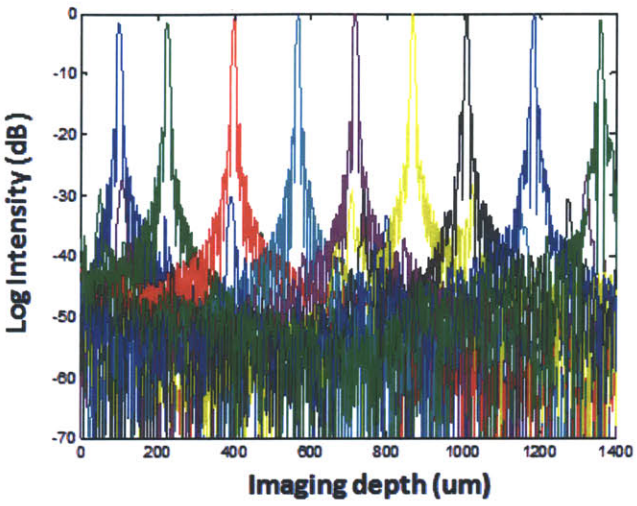

Figure 19: PSFs from different depths of the optically clocked 1310 nm system showing virtually no roll-off for the entire depth range.

The transverse resolution of the system can be characterized by imaging an USAF resolution chart. Figure 20 displays an image taken by the 40X objective. Note that the smallest element in the chart is resolved which indicates a transverse resolution better than 2.2 um. In order to measure the exact transverse resolution a knife edge test can be performed [23]. For this test, the intensity drop from an edge in the resolution chart is plotted and the width from 90% of the maximum value to 10% of the maximum value is calculated. Then this edge width is multiplied with 0.78 to calculate the $1/e^2$ transverse resolution. Using this test the transverse resolution is measured as 0.86 um for the 40X Olympus objective. Transverse resolution is also measured with the 10X Zeiss objective where the smallest resolvable lines in the resolution chart predicted a resolution of 3.11 um. Note that these values are consistent with the theoretical values calculated in Section 4.1.

Finally, the sensitivity of the 1310 nm system is measured as 102 dB. For the measurement of the sensitivity an ND filter of 3.3 OD is inserted to the sample arm to attenuate the reflection from a mirror placed to the focus of the objective. The reference arm power is adjusted to an optimum value until the best sensitivity is achieved. The reference arm signal is also recorded by blocking the sample arm. The processing consisted of removing the reference arm signal from the interference fringe followed by the Fourier transform operation. The value of the resulting peak intensity is divided by the standard deviation of the noise level, then the logarithm of this ratio is taken and multiplied with 20, which gave a value of 36 dB. Due to the double pass of the light on the sample arm, the OD value of 3.3 of the ND filter corresponds to an attenuation of 66 dB. Consequently a sensitivity of 102 dB is measured.

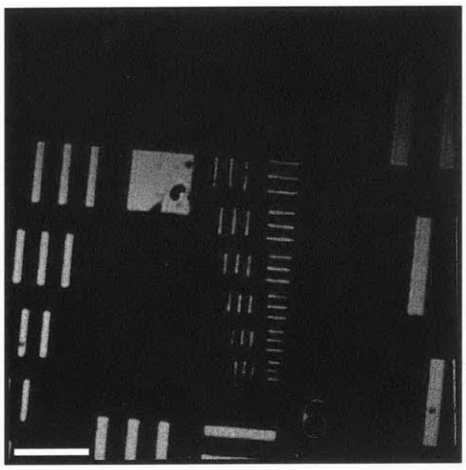

Figure 20: Image from USAF resolution chart taken by the 40X objective where the smallest element in the resolution chart is clearly delineated.

References

[1] A. E. Siegman, *Lasers*. Mill Valley, CA.: University Science Books, 1986.

[2] W. Drexler and J. G. Fujimoto, *Optical coherence tomography : technology and applications*. Berlin ; New York: Springer, 2008.

[3] B. R. Biedermann, W. Wieser, C. M. Eigenwillig, G. Palte, D. C. Adler, V. J. Srinivasan, J. G. Fujimoto, and R. Huber, "Real time en face Fourier-domain optical coherence tomography with direct hardware frequency demodulation," *Opt Lett,* vol. 33, pp. 2556-8, Nov 1 2008.

[4] R. Szeliski, "Image alignment and stitching: a tutorial," *Found. Trends. Comput. Graph. Vis.,* vol. 2, pp. 1-104, 2006.

[5] A. Agarwala, M. Dontcheva, M. Agrawala, S. Drucker, A. Colburn, B. Curless, D. Salesin, and M. Cohen, "Interactive digital photomontage," *Acm Transactions on Graphics,* vol. 23, pp. 294-302, Aug 2004.

[6] S. Winder, G. Hua, and M. Brown, "Picking the best DAISY," *Cvpr: 2009 Ieee Conference on Computer Vision and Pattern Recognition, Vols 1-4,* pp. 178-185, 2009.

[7] S. Abeytunge, Y. Li, B. Larson, R. Toledo-Crow, and M. Rajadhyaksha, "Rapid confocal imaging of large areas of excised tissue with strip mosaicing," *Journal of Biomedical Optics,* vol. 16, p. 050504, May 2011.

[8] S. Tang, T. B. Krasieva, Z. Chen, and B. J. Tromberg, "Combined multiphoton microscopy and optical coherence tomography using a 12-fs broadband source," *Journal of Biomedical Optics,* vol. 11, p. 020502, Mar-Apr 2006.

[9] B. W. Graf, S. G. Adie, and S. A. Boppart, "Correction of coherence gate curvature in high numerical aperture optical coherence imaging," *Opt Lett,* vol. 35, pp. 3120-2, Sep 15 2010.

[10] B. W. Graf and S. A. Boppart, "Multimodal In Vivo Skin Imaging with Integrated Optical Coherence and Multiphoton Microscopy," *Ieee Journal of Selected Topics in Quantum Electronics,* vol. 18, pp. 1280-1286, Jul-Aug 2012.

[11] A. D. Aguirre, J. Sawinski, S. W. Huang, C. Zhou, W. Denk, and J. G. Fujimoto, "High speed optical coherence microscopy with autofocus adjustment and a miniaturized endoscopic imaging probe," *Optics Express,* vol. 18, pp. 4222-39, Mar 1 2010.

[12] V. J. Srinivasan, H. Radhakrishnan, J. Y. Jiang, S. Barry, and A. E. Cable, "Optical coherence microscopy for deep tissue imaging of the cerebral cortex with intrinsic contrast," *Optics Express,* vol. 20, pp. 2220-39, Jan 30 2012.

[13] D. C. Adler, C. Zhou, T. H. Tsai, J. Schmitt, Q. Huang, H. Mashimo, and J. G. Fujimoto, "Three-dimensional endomicroscopy of the human colon using optical coherence tomography," *Optics Express,* vol. 17, pp. 784-796, Jan 19 2009.

[14] A. D. Aguirre, "Advances in Optical Coherence Tomography and Microscopy for endoscopic applications and functional neuroimaging," Ph D, Harvard-MIT Division of Health Sciences and Technology, 2008.

[15] A. D. Aguirre, Y. Chen, B. Bryan, H. Mashimo, Q. Huang, J. L. Connolly, and J. G. Fujimoto, "Cellular resolution ex vivo imaging of gastrointestinal tissues with optical coherence microscopy," *Journal of Biomedical Optics,* vol. 15, p. 016025, Jan-Feb 2010.

[16] C. Zhou, D. W. Cohen, Y. Wang, H.-C. Lee, A. E. Mondelblatt, T.-H. Tsai, A. D. Aguirre, J. G. Fujimoto, and J. L. Connolly, "Integrated Optical Coherence Tomography and Microscopy for Ex Vivo Multiscale Evaluation of Human Breast Tissues," *Cancer Research,* vol. 70, pp. 10071-10079, Dec 15 2010.

[17] H. C. Lee, C. Zhou, D. W. Cohen, A. E. Mondelblatt, Y. Wang, A. D. Aguirre, D. Shen, Y. Sheikine, J. G. Fujimoto, and J. L. Connolly, "Integrated optical coherence tomography and optical

coherence microscopy imaging of ex vivo human renal tissues," *J Urol,* vol. 187, pp. 691-9, Feb 2012.

[18] S. M. Pizer and J. B. Zimmerman, "Color Display in Ultrasonography," *Ultrasound in Medicine and Biology,* vol. 9, pp. 331-345, 1983.

[19] K. W. Beach, J. F. Primozich, and D. E. Strandness, "Pseudocolor B-Mode Arterial Images to Quantify Echogenicity of Atherosclerotic Plaque," *Ultrasound in Medicine and Biology,* vol. 20, pp. 731-742, 1994.

[20] D. S. Gareau, "Feasibility of digitally stained multimodal confocal mosaics to simulate histopathology," *Journal of Biomedical Optics,* vol. 14, p. 034050, May-Jun 2009.

[21] J. Bini, J. Spain, K. Nehal, V. Hazelwood, C. DiMarzio, and M. Rajadhyaksha, "Confocal mosaicing microscopy of human skin ex vivo: spectral analysis for digital staining to simulate histology-like appearance," *Journal of Biomedical Optics,* vol. 16, p. 076008, Jul 2011.

[22] L. T. Perelman, V. Backman, M. Wallace, G. Zonios, R. Manoharan, A. Nusrat, S. Shields, M. Seiler, C. Lima, T. Hamano, I. Itzkan, J. Van Dam, J. M. Crawford, and M. S. Feld, "Observation of periodic fine structure in reflectance from biological tissue: A new technique for measuring nuclear size distribution," *Physical Review Letters,* vol. 80, pp. 627-630, Jan 19 1998.

[23] M. Rajadhyaksha, R. R. Anderson, and R. H. Webb, "Video-rate confocal scanning laser microscope for imaging human tissues in vivo," *Appl Opt,* vol. 38, pp. 2105-15, Apr 1 1999.

5. Imaging Results

In this chapter, some example images obtained with the 1060 nm and 1310 nm VCSEL OCM systems will be presented. Unless noted otherwise, majority of the images are displayed after a square root compression and with the positive grayscale color map. In order to obtain corresponding images without performing histological processing, some of the specimens are imaged with a multiphoton microscopy (MPM) imaging system possessed by our group. Immediately after the OCM imaging session is conducted, specimen is stained with acridine orange which, as previously mentioned, stains the nuclei of the cells. When it is excited with a high power laser around 740 nm, it emits a two photon signal around 530 nm. Furthermore, with the same excitation, second harmonic signal centered at 370 nm is also emitted from collagen structures that are typically residing in the extracellular spaces of the cells. As a consequence, the resulting image displays two color channels corresponding to two photon fluorescence from the nuclei and second harmonic generation from the collagen in the stroma, similar to the counterstaining role of hemalum and eosin in the standard histological processing as discussed in Section 4.8 [1].

5.1. Imaging Results with the 1060 nm System

Initial imaging studies have been conducted with the 1060 nm VCSEL OCM system. According to the imaging protocol, fresh specimens are imaged within a few hours after excision. Prior to imaging of the specimens, they are dipped into a 6% acetic acid solution for ~1 minute followed by a ~30 second wash with water, in order to increase the nuclear contrast by the mechanism which condenses nuclear material in the cell and increases the scattering from the nuclei [2]. Imaging is performed in the modified cassette used in standard histology, as previously described. The 40X Olympus water immersion objective is employed whose properties are given in Section 4.1.

Figure 1 show *ex vivo* OCM images from freshly excised rabbit kidney samples together with the corresponding MPM images. In Fig. 1 (A) and (B) a glomerulus and surrounding convoluted tubules can be observed, which are characteristic features of renal cortex. Figure 1 (D) and (E) are also from renal cortex and delineate the contour of the convoluted tubules more clearly. Figure 1 (C) and (F), on the other hand, show the collecting tubules from renal medulla where cellular features in the epithelial lining of tubules can be clearly discerned. Figure 1 (G) and (T) show the corresponding MPM images from renal cortex and medulla, respectively. These images are acquired by setting the focal plane ~ 50 um deep from the surface of the specimen.

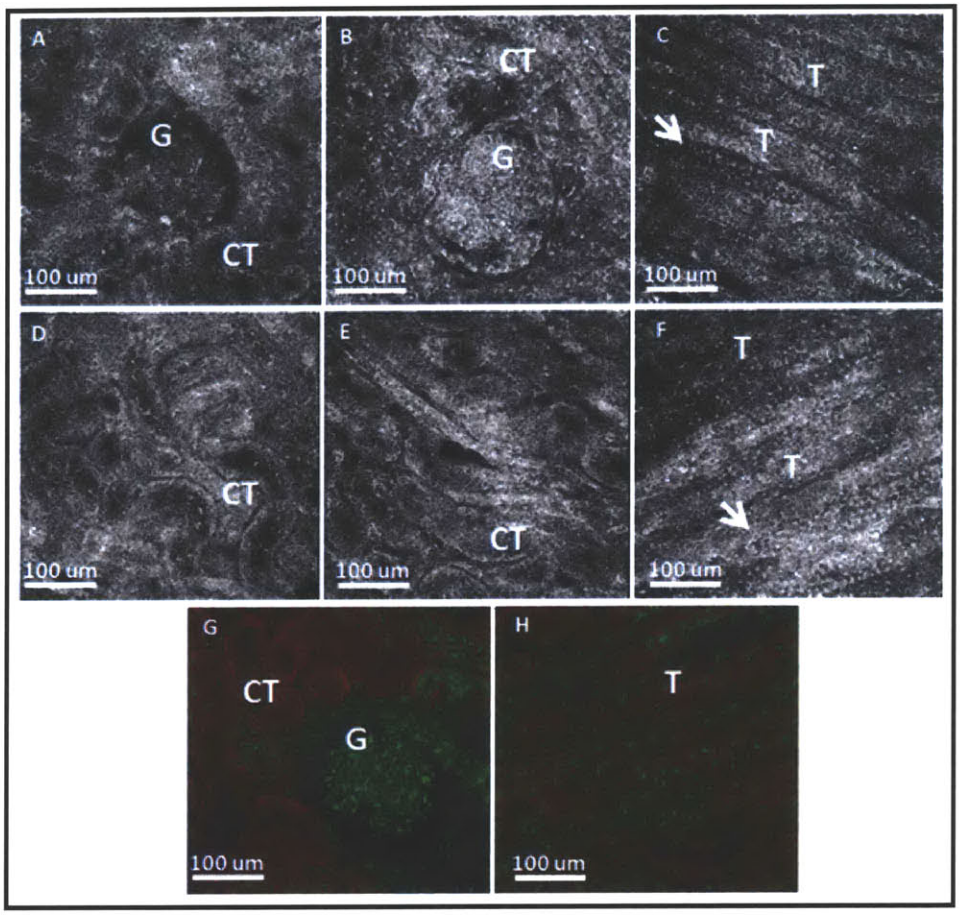

Figure 1: OCM and corresponding MPM images from *ex vivo* fresh rabbit kidney obtained using the 40X Olympus objective. Specimens are treated with 6% acetic acid. (A, B, D, E, G) are from renal cortex, whereas (C, F, H) are from renal medulla. Arrows point to cellular features apparent in the epithelial lining of the tubules. CT: Convoluted tubules, G: Glomerulus, T: Collecting tubules.

Figure 2 shows *ex vivo* OCM images from freshly excised rabbit colon sample together with the corresponding MPM image. In this figure, contour of the colonic architecture can be identified with occasional crypts. Note that the sizes of the crypts are relatively smaller and they are not very densely packed compared to the crypts usually observed in human colon. Furthermore, goblet cells can not be visualized neither in the OCM nor in the MPM images.

Figure 3 shows *ex vivo* OCM images from freshly excised normal human colon specimen together with a representative histology. Figure 3 (A-C) have been obtained from the same imaging location, by translating the focus ~20 um between each acquisition. The depth dependent features of the crypt architecture can be appreciated in these images. A close correspondence can be observed between OCM images and the histology image shown in Fig. 3 (F). Note that OCM images clearly delineate the mucin secreting goblet cells residing on the outer linings of the crypts.

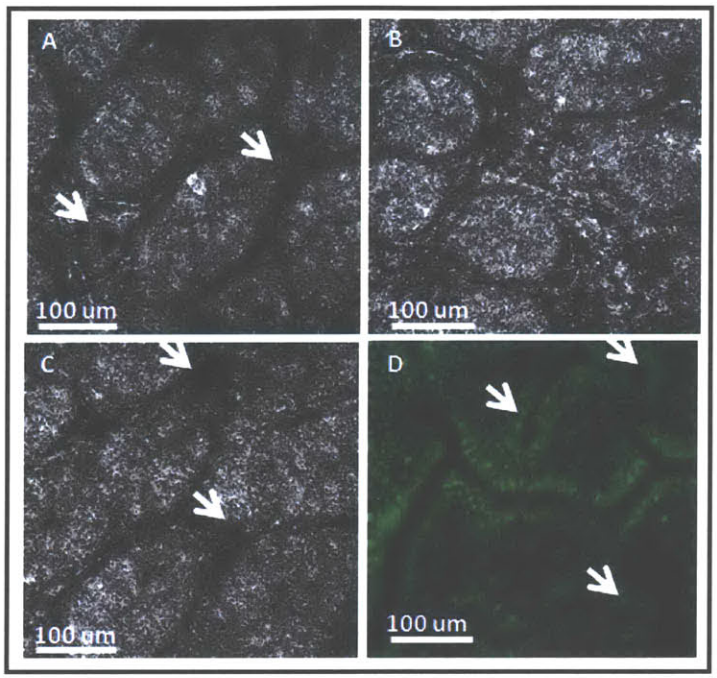

Figure 2: OCM and corresponding MPM images from *ex vivo* fresh rabbit colon obtained using the 40X Olympus objective. Specimens are treated with 6% acetic acid. Arrows point to crypts.

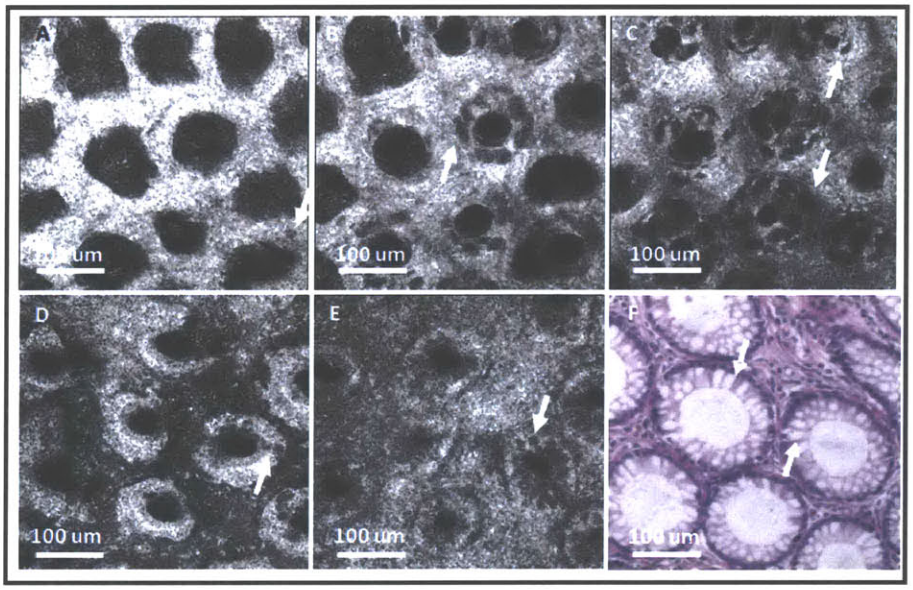

Figure 3: OCM and representative histology from *ex vivo* fresh human colon obtained using the 40X Olympus objective. Specimens are treated with 6% acetic acid. (A-C) have been obtained from the same imaging location, by translating the focus ~20 um between each acquisition. (D) and (E) are from different imaging locations on the same specimen. Arrows point to goblet cells.

Figure 4 shows a mosaic image from freshly excised normal human colon sample obtained by constructing the mosaic image from 16 overlapping frames, using the methods described in Section 4.7. The total field is increased to about 1 mm x 1 mm in this representative mosaic image. From the link provided in the caption the deep zoom formatted image can be accessed, which allows the user to pan around the image and to zoom to regions of interests, similar to the Google earth view. As a side note, it is worth noting that from this large FOV mosaic image, a Type – I pit pattern, which is the characteristic appearance of normal colonic mucosa as discussed in Section 2.2. can be clearly observed. Therefore, generating large FOV images has the advantage of identifying the crypt architecture of the colon which will facilitate the assessment of the neoplastic state of the tissue, while regions of interests can still be investigated with high resolution.

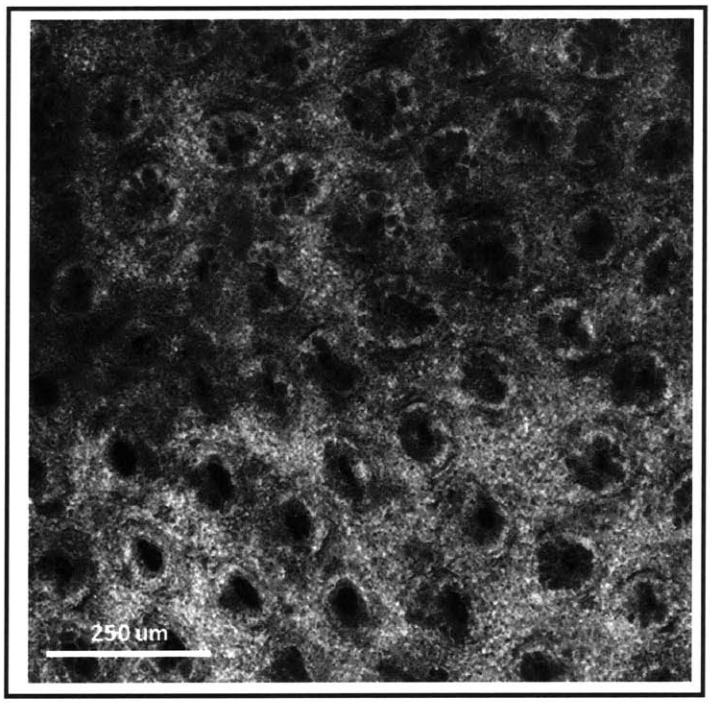

Figure 4: Large FOV mosaic image from *ex vivo* fresh human colon obtained by stitching 16 frames. The deep zoom file can be accessed from the following link which allows pan and zoom the image: http://bit.ly/SPvqVM

Figure 5 shows an example of a large field OCM image from an *ex vivo* invasive breast cancer sample, together with a multiphoton image of the same region and representative histology. The OCM image shown in this figure is generated by combining 96 frames with a field of 420 um x 420 um each to obtain a 1.8 mm by 2.6 mm total field. Sepia color map is chosen for displaying the OCM image. Adipose tissue and invasive lesions are distinguishable in the OCM image as hollow circular structures and homogenous high scattering tissues, respectively. Residual stroma, identified as parallel stripes in the OCM image is also present and

encapsulates the tumor tissue. Note that, this sample is from a highly invasive breast cancer, where the delineation of individual nuclei is challenging even in the MPM images. Therefore, the contrast in the OCM image is relatively low. For a less invasive or normal breast lesion, it should be possible to identify ducts, lobules and surrounding stroma, which are characteristic features of the breast tissue.

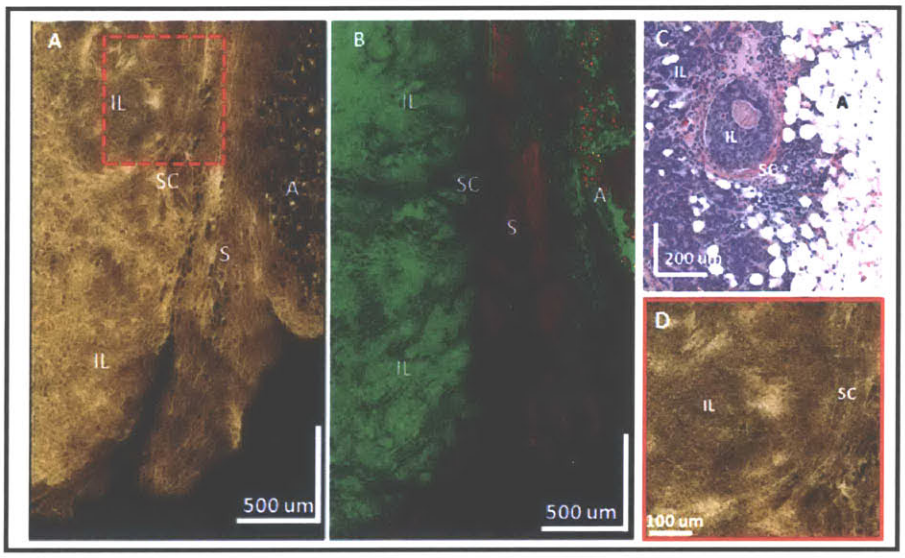

Figure 5: OCM and multiphoton image of an *ex vivo* fresh breast cancer sample and representative histology. OCM image is obtained using the 40 X Olympus objective. Specimens are treated with 6% acetic acid for the OCM image and acridine orange for the MPM image. OCM image is constructed by merging 96 frames. (D) shows a zoomed view for the region shown with dashed lines in (A). IL: Invasive Lesion; SC: Stromal Capsule; S: Residual Stroma; A: Adipose. The deep zoom file can be accessed from the following link which allows pan and zoom the image: http://bit.ly/UzbiVz

5.2. Imaging Results with the 1310 nm System

Preliminary images have already been obtained with the 1310 nm VCSEL OCM setup, although the system is still under development. Similar to the 1060 nm OCM system, imaging is performed in the modified cassette. The 40X Olympus water immersion objective and 20X Zeiss objective are employed for the imaging, whose properties are given in Section 4.1.

Figure 6 depicts examples of OCM images of *ex vivo* fixed human colon samples obtained with the 1310 nm system. Note that this is the same specimen whose images are depicted in Fig. 3 and Fig. 4, and the image quality looks comparable to those images, despite imaging is done on fixed specimens. Figure 6 (C) is taken using the 20X Zeiss objective, and shows reasonable image quality and minimal loss in resolution compared to the images taken with the 40X objective. Note that for the 20X image the scan angle of the scanning mirrors are

adjusted to a smaller value in order to acquire similar FOV as the 40X objective for comparison purposes, whereas the total FOV with the 20X objective is about 1.25 mm x 1.25 mm as discussed in Section 4.1.

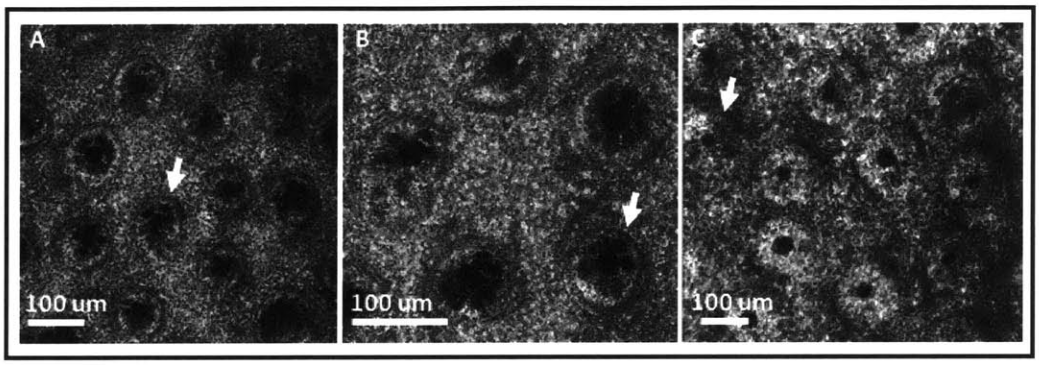

Figure 6: OCM image obtained from *ex vivo* fixed human colon sample using the 1310 nm system. (A,B) are obtained with the 40X objective whereas (C) is obtained with the 20X objective.

Note that, as discussed previously, the use of lower NA objective with a longer confocal range enables to exploit the full power of the Fourier domain OCM imaging which enables the acquisition of multiple imaging depths simultaneously. As a demonstration, Fig. 7 shows OCM images from an *ex vivo* fixed human colon sample. These images are selected from the same volumetric dataset, at a depth location 50 um apart from each other. Depth dependent features of the crypt architecture can be clearly observed in the images. As a side point, note that the crypt structure seen in Fig. 7 (B) is remarkably different compared to the crypt structure seen in Fig. 6. This might be due to the different compression that the modified histology cassette applies to the tissue or the differences in the tilt of the crypts for the two different samples. Nevertheless, these images show the high impact on the differences in the sample preparation on the resulting OCM images. Therefore, in order to be able to obtain consistent images, it is important to use the same protocol (applying same pressures etc.) for imaging different specimens of the same tissue.

Note that for the OCM images shown in this section, the specimens were fixed for a few months when they are imaged, which might cause a loss in the contrast due to degradation and changes in the optical properties of the tissue. Although the colon is preserved relatively well during fixation, the loss in the contrast for other tissues such as kidney and breast are very drastic and it is not possible to obtain good quality OCM images from fixed specimens of those samples. Recruitment of fresh samples of human colon, kidney, breast and thyroid to be imaged with the 1310 nm system is currently ongoing.

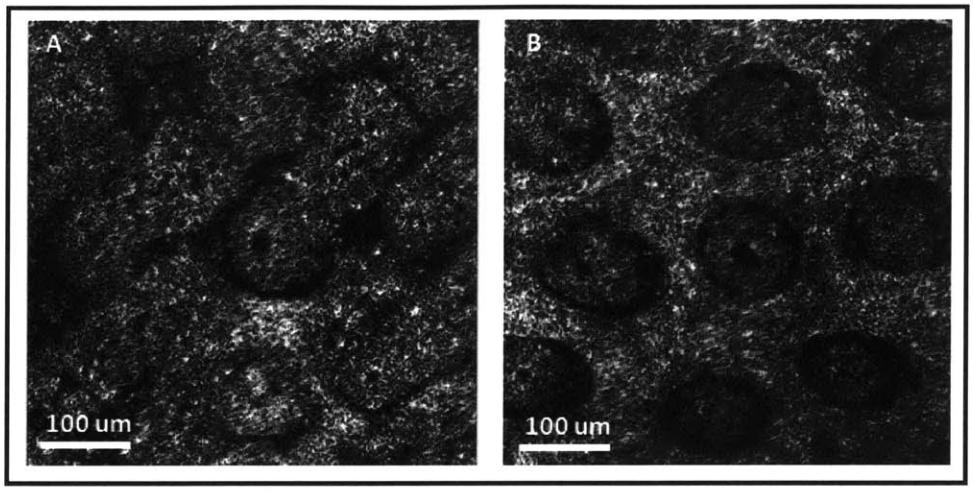

Figure 7: OCM image obtained from *ex vivo* fixed human colon sample with the 20X objective. Images are selected from the same volumetric dataset, 50 um apart from each other in depth.

References

[1] Y. K. Tao, O. O. Ahsen, P. Fendel, A. E. Cable, D. Shen, J. L. Connolly, and J. G. Fujimoto, "Breast Pathology Assessment Using Two-Photon Microscopy," *SPIE Photonics West* 2012.

[2] R. A. Drezek, T. Collier, C. K. Brookner, A. Malpica, R. Lotan, R. R. Richards-Kortum, and M. Follen, "Laser scanning confocal microscopy of cervical tissue before and after application of acetic acid," *American Journal of Obstetrics and Gynecology,* vol. 182, pp. 1135-1139, May 2000.

6. Summary and Future Work

In summary, in this study a swept source OCM system has been demonstrated which employs a novel VCSEL light source. The A-scan rate of the OCM system can easily reach > 1 MHz when the system is run off-resonance and it is shown that optical clocking circumvents the deleterious effects related to the sweep variations of the VCSEL that run in this mode. The axial resolution of the system with the 1310 nm light source is measured as 8.1 um in tissue, which is still lower than time domain and spectral OCM systems. However, next generation VCSELs are expected to have ~160 nm tuning range which will improve the axial resolution to < 6 um. When the broad tuning range VCSEL becomes available it will replace the laser currently employed in the OCM setup.

Recruitment of fresh samples to be imaged with the 1310 nm VCSEL system will continue in the future. For this purpose a variety of pathologies have been identified which will show the fidelity of the imaging system. These pathologies include colon (normal, tubular adenoma, adenocarcinoma), breast (normal, ductal carcinoma in situ (DCIS), invasive ductal carcinoma (IDC)), kidney (normal and cancer) and thyroid (normal and cancer). Furthermore, modifications to the imaging setup will continue to be implemented to make it more compact and robust, so that it can be transported to the pathology laboratory or to the endoscopy suite. Once the system is placed to the clinic it will be possible to conduct large scale studies for selected applications that will show the sensitivity and specifity of OCM imaging in making real time diagnosis. Towards this end, an alternative, inverted microscopy design can be implemented where the specimen is placed directly on a cover slip and illuminated from the bottom. This will make the imaging process easier, as well as it will reduce artifacts due to the pressure applied to the tissues when they are pressed against the cover slip in the modified cassette. An inverted microscope design, however, will require the use of air immersion objectives, which might cause issues with increased noise floor due to the reflections from the cover slip surfaces as seen in Section 4.8. Anti reflection coatings for the cover slips can be employed to overcome these issues.

Another aspect of real time imaging with a Fourier domain OCM system is the demanding processing speeds, as one needs to process the full volumetric dataset in order to obtain *en face* images. The current acquisition software used in our group is able to process the datasets with relatively fast speed using parallel processing architectures and is constantly being improved. However, if processing speeds are proven to be a limiting factor, then alternative processing strategies, such as direct computation, Goertzel algorithm or zoom FFT algorithms can be employed that will produce *en face* images from selected depths with an increased speed compared to taking the full FFT of the fringes.

With the novel OCM scanning probes it is possible to translate this imaging modality to an *in vivo* setting, where the OCM probe can be inserted through the working channel of the endoscope and obtain images similar to CLE. Especially for some of the clinical challenges in the management of lower GI diseases discussed in Chapter 2, OCM has distinct advantages over CLE which can make this technology a strong alternative to the latter imaging modality. In this respect, the benchtop OCM system developed in the course of this thesis plays a major role in determining the quality of the images that can be expected with the endoscopic OCM probe.